IDENTIFICATION OF THE INTERDEPENDANCE OF AGING AND INTERNAL PRESSURE EVOLUTION OF COMMERCIAL LI-ION CELLS

by

ANTHONY MATASSO

Presented to the Faculty of the Graduate School of

The University of Texas at Arlington in Partial Fulfillment

of the Requirements

for the Degree of

DOCTOR OF PHILOSOPHY

THE UNIVERSITY OF TEXAS AT ARLINGTON

December 2014

Acknowledgements

I would first like to thank God, through whom all things are possible. Next, I would like to thank my wife Amy, my sons Josh and Andy, and my parents for their patience and unwavering support through my professional and academic career. I also want to thank my advisor, Dr. David Wetz, for his guidance, assistance, and expertise through this arduous process. Additionally, I would like to thank my committee for their support: Dr. William Dillon, Dr. Rasool Kenarangui, Dr. Wei-Jen Lee, and Dr. Fuqiang Liu. I would also like to acknowledge David Boston, Cynthia Griffith, Jimmy Hanhart, Dong Liu, Derek Wong, and all of my fellow students in the lab for their assistance. Finally, I would like to thank Dr. Ray Johnson and Lockheed Martin for the extraordinary opportunity they have provided me.

November 10, 2014

Abstract

IDENTIFICATION OF THE INTERDEPENDANCE OF AGING
AND INTERNAL PRESSURE EVOLUTION OF
COMMERCIAL LI-ION CELLS

Anthony Matasso, PhD

The University of Texas at Arlington, 2014

Supervising Professor: David A. Wetz

The demand for high power and energy coupled with long cycle life, low cost, and increased safety have become the driving factors in the development of lithium-ion batteries. This demand continues to expand with the sustained capability expansion of high power military applications, electric vehicles, grid-tie energy storage, and other renewable energy applications. Unlike the short innovation cycles that technologies like portable electronics experience, these applications are focused on an affordable long term product lifecycle that is safe. In order to achieve these long term goals, a better understanding of the chief degradation mechanisms as well as a more sophisticated approach for battery life prediction is needed.

This research examined the use of internal pressure evolution of commercial lithium-ion cells as a metric for predicting aging or damage. A novel test chamber was designed and manufactured that enabled commercial cells to be punctured in an inert environment and tested inside of the chamber during full

lifecycle, and damage event testing. Three studies were undertaken to examine the internal pressure behavior of li-ion cells: the single cycle internal pressure evolution of a $LiFePO_4/C_6$ cell over high-rate lifecycle testing, over-discharge characterization of various li-ion chemistries, and a more extensive study aimed at correlating the internal pressure rise and capacity degradation of $LiCoO_2/C_6$ cells cycled at elevated rates. These studies examined the pressure evolution behavior of the cells and compared this behavior with degradation analysis including electrochemical impedance spectroscopy, capacity fade, DC equivalent series resistance, differential capacity, gas chromatography-mass spectroscopy, and scanning electron microscope imaging.

Through the measurement and understanding of the bulk internal pressure behavior, these studies confirmed the ability to detect degradation events like over-discharge, the ability to measure the apparent bulk volume change of the electrodes and correlate this change to the capacity fade of the cell, and the ability to directly correlate the pressure rise with the capacity fade of various cells cycled at high-rate charge and discharge. The addition of internal pressure as an in-situ measurement may be used as a substitute or to supplement other more conventional diagnostic tools. Additionally, this method may be of particular use for systems that are cycled at high rate, high temperatures, or both.

Table of Contents

List of Illustrations

List of Tables

Chapter 1

Introduction

The demand for high power and energy coupled with long cycle life, low cost, and increased safety have become the driving factors in the development of lithium-ion batteries (LIBs). This demand continues to expand with the sustained capability expansion of high power military applications, electric vehicles, grid-tie energy storage, and other renewable energy applications. Unlike the short innovation cycles that technologies like portable electronics experience, these applications are focused on an affordable long term product lifecycle that is safe. In order to achieve these long term goals, a better understanding of the chief degradation mechanisms as well as a more sophisticated approach for battery life prediction is needed. The complicated nature of LIB aging poses a challenge to this goal as the power and capacity fade are products of various processes and internal interactions. There has been extensive research aimed at better understanding the stability of various electrode materials, electrolytes, and cell components, however power and capacity fade continue to be a nontrivial impediment to many of these applications. The cause of power and capacity fade of LIBs can generally be grouped into three categories: structural degradation (e.g., volume change, phase transition, and binder decomposition), chemical changes to the electrodes (e.g., chemical decomposition, dissolution reaction), and surface layer formation at the electrode-electrolyte interface. Additionally, current collector corrosion and metallic lithium plating contribute to power and capacity fade. All of these degradation mechanisms will vary depending on the materials chosen, however the general mechanisms remain valid for most systems [1].

The research presented here was comprised of two main objectives. The first was to measure the internal pressure evolution of commercial lithium-ion cells under various cycling conditions and determine the correlation of the bulk pressure evolution to the capacity fade or damage. The second objective was to examine the primary degradation mechanisms present in the cell and determine the relationship to both pressure evolution and capacity fade. Previous research suggests that loss of active lithium at the anode, and impedance rise at both the cathode and anode are the major process related to capacity fade [2]. At high rate charge and discharge cycling, it has been shown that the anode dominates the impedance rise as a result of an accelerated and excessive SEI layer growth on the electrode surface [1]–[4]. This passivation layer is a result of the reduction of electrolyte at the anode surface which produces various hydrocarbon gases [5]. An examination of the internal pressure evolution can reveal the generation of gases inside the cell as a result of this passivation layer formation and other chemical changes occurring at the electrodes. While there are multiple factors that affect the production of gases, a correlation of the bulk internal gas production to capacity fade or damage for a given system would be a useful diagnostic tool aiding in the prediction of cell life or damage.

Chapter 2

Background

A battery is a device that utilizes an oxidation-reduction reaction to convert stored chemical energy into electrical energy. The first battery, known as the voltaic pile, was demonstrated in 1799 by Alessandro Volta. The pile was constructed by stacking dissimilar metals, silver and zinc, separated by cardboard soaked in salt water. This configuration resulted in a small electric current passing between the silver and zinc electrodes [6]. Over the past two centuries, the battery has made great strides in its construction, performance, and capability becoming an essential part of modern life. In recent history, lithium-metal primary batteries (disposable batteries) were identified as a promising energy storage technology and developed in the early 1970's with Sanyo commercializing the technology in 1975. The technology matured, but was plagued by safety concerns stemming from lithium dendrite growth which could lead to an internal short circuit of the battery. In the early 1990's Sony Corp commercialized the first practical lithium-ion secondary battery (rechargeable battery). Early batteries used a hard-carbon anode and LiCoO2 cathode materials coupled with a propylene carbonate-based electrolyte. This configuration allowed lithium to be reversibly deintercalated and intercalated into the carbon crystalline structure producing lithiated graphite. The use of a carbon anode retained a similar reduction potential to that of lithium while demonstrating outstanding cycling performance, all while eliminating the dendrite formation issue found with lithium anodes [7]. The result of this development has produced a technology that has a high energy density, high power density, high working voltage, low self-discharge rates, long cycle life, and no memory effects.

Lithium-Ion Batteries

Electrochemical Operation

A typical commercial lithium-ion battery is comprised of three main components, namely the positive electrode (cathode), the negative electrode (anode), and the electrolyte. These components are packaged using various methods and form factors to support commercial requirements. Figure 2-1 shows a lithium-ion battery packaged in a standard 26650 cylindrical construction. The anode and cathode are rolled up with a thin separator in between and are soaked with a non-aqueous electrolyte. The separator prevents physical contact and electronic flow between the cathode and anode while allowing free ionic transport through the electrolyte. This roll is placed inside of the stainless steel case, and the negative tab is welded to the case. The positive tab of the roll is welded to the positive terminal of the case, and the entire cell is sealed. As a safety precaution, a venting mechanism is incorporated into the case to allow the cell to vent in the case of an internal overpressure.

Secondary lithium-ion batteries are rechargeable such that the battery can be charged and discharged hundreds or thousands of times. The left part of Figure 2-2 illustrates the discharge process in which the lithium-ions leave the anode, transition through the electrolyte, and insert into the cathode. During this process, the electrons transition across the load and generate electrical power. The charge process, as seen on the right side of Figure 2-2, reverses this behavior and thus the lithium-ions move from the cathode to the anode.

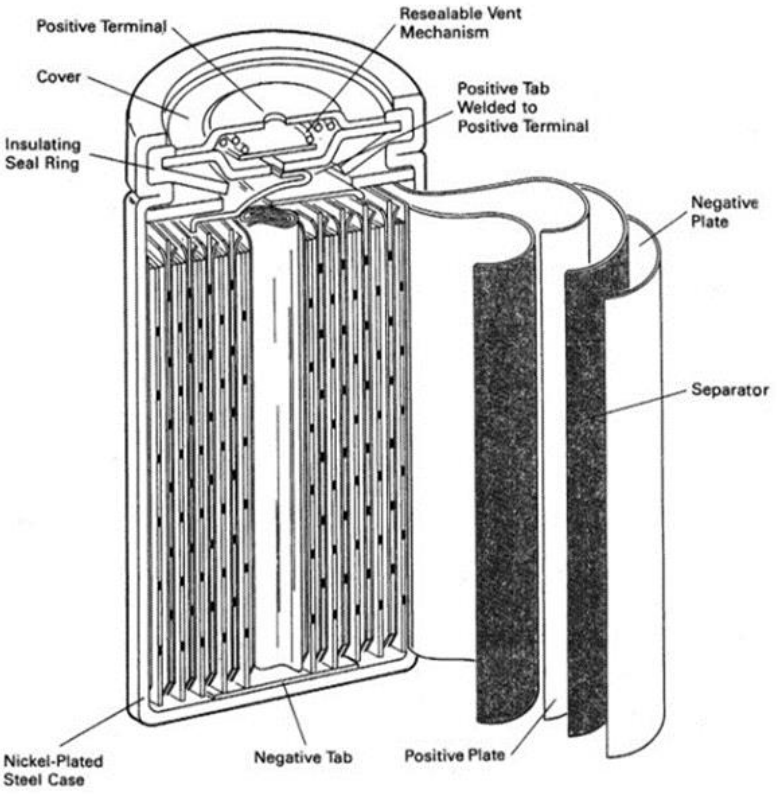

Figure 2-1 Commercially constructed 26650 format li-ion battery [8].

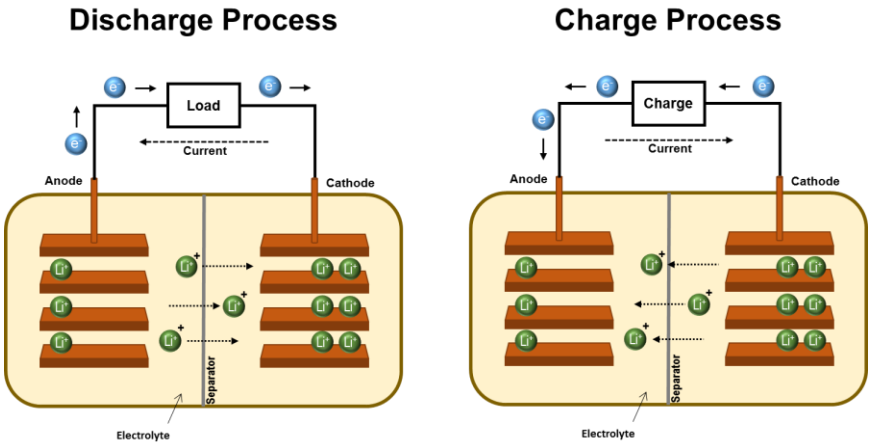

Figure 2-2 Charge and discharge process of a typical li-ion battery.

Using the Sony LiCoO2 battery as an example, the reversible electrochemical reaction at the cathode can be represented by Equation 2-1, and the analogous reaction at the anode is denoted in Equation 2-2.

$$LiCoO_2 \rightleftarrows Li_{1-x}CoO_2 + xLi^+ + xe^- \quad (2\text{-}1)$$

$$xLi^+ + xe^- + 6C \leftrightarrows Li_xC_6 \quad (2\text{-}2)$$

Anode Materials

The most commonly used anode materials are carbon based or more specifically graphite based electrodes. It is the primary material used for the anode in commercial secondary batteries due to its availability, cycling performance, and its safety compared to Lithium. Graphite is a hexagonal arrangement of six carbon atoms arranged in a stacked ABAB sequence as seen in Figure 2-3. The graphene planes are aligned along the c-axis and are held together by a weak Van der Walls force creating the layered structure. The carbon atoms are covalently bonded to three other atoms in the plate with an angle of 120°. The carbon atom has four valence electrons, three of which are used for the covalent bonding, one which is not covalently bonded allowing it to be easily displaced by an electric field. This fourth electron is responsible for the electrically conductive quality that graphite experiences [9].

The inter-layer distance is 0.34 nm creates an ideal location for lithium intercalation. This intercalation process changes the stacking sequence from ABAB to AAAA, and the lithium atoms locate between the C_6 sheets forming LiC_6 as seen in Figure 2-4. Each of the lithium atoms is centered between the two hexagonal

structures of each layer increasing the inter-layer distance to 0.37 nm [10]. This inter-layer expansion is associated with an estimated 12% volume expansion when the graphite is in the lithiated phase. This volume expansion and contraction pulverizes the graphite degrading the material with extended cycling which contributes to the irreversible capacity fade experienced in the system.

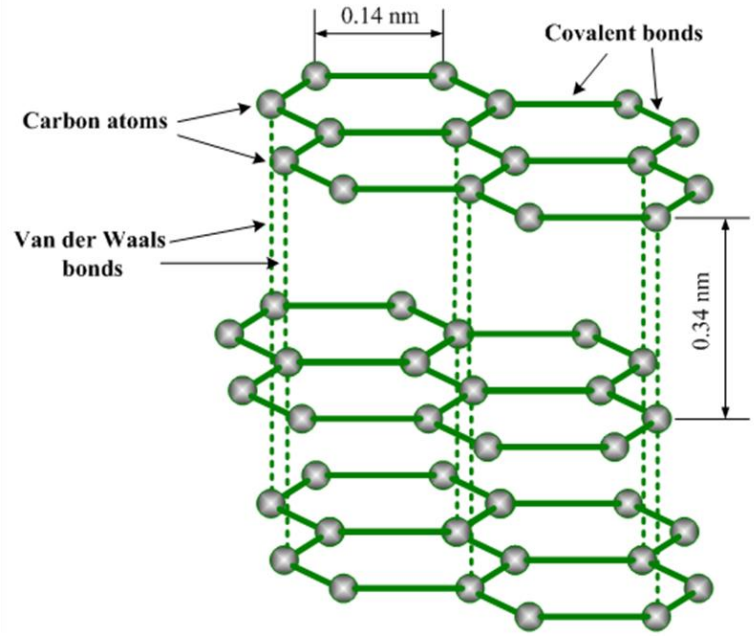

Figure 2-3 Crystal structure of hexagonal graphite with subsequent ABAB stacking [9].

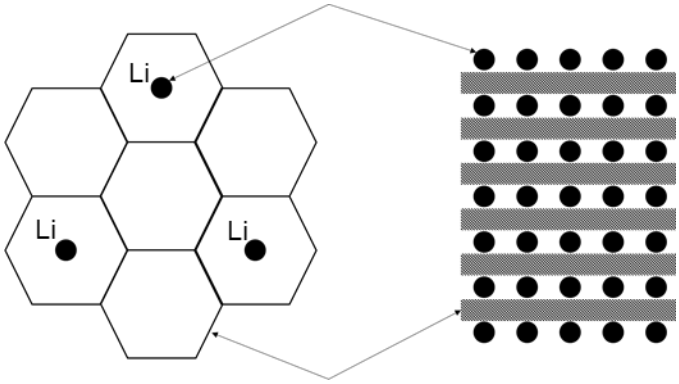

Figure 2-4 Arrangement of intercalated lithium and carbon atoms.

While graphite is the most commonly used anode material in commercial li-ion batteries, alternative materials are needed to expand capability. As the graphite anode is cycled, structural changes, loss of lithium, excess growth of the solid electrolyte interphase (SEI), and trapping of lithium-ions within sites in the carbon matrix/layers prevent the li-ions from going back to the parent cathode can contribute to the degradation in performance. As previously mentioned, mechanical strain on the graphite due to intercalation and de-intercalation of lithium ions can result in crack formations and contribute to capacity fade [1], [11]. However, the primary limitation is the theoretical specific capacity of 372 Ah/kg, and the theoretical volumetric capacity of 833 Ah/l. Table 2-1 includes a list of some of the first materials to be examined for use as electrodes. This table includes the theoretical capacities for the materials which indicate a remarkable increase over carbon. However, the high percent volume change exacerbates the mechanical strain issue seen in carbon and creates challenges for long term cycling.

Table 2-1 Capacities and volume changes of different elements [7].

Starting Material	C	Al	Si	Sn	Bi
Lithiated Phase	LiC_6	Li_9Al_4	$Li_{21}Si_5$	$Li_{17}Sn_4$	Li_3Bi
Theoretical Specific Capacity (Ah/kg)	372	2235	4010	959	385
Theoretical Volumetric Capacity (Ah/l)	833	6035	9340	7000	3773
Volume Change (%)	12	238	297	257	115

Cathode Materials

A number of different cathode materials have been explored for commercial use in LIBs. In ordered to be considered for production, the material must be low cost, have low toxicity, and be producible. In addition to these basic qualifications, the cathode must have the following specific characteristics [12]:

1. The cathode must intercalate or insert Li^+.
2. High Potential: Should show low electron energy and low site energy for Li^+.
3. Flat Potential: The electrical potential should have limited variation as a function of Li^+ content.
4. High Energy: High specific and gravimetric capacity.
5. High Power: The coupled diffusion of electrons and Li^+ must be fast.
6. High Cycle-ability: Li^+ intercalation/insertion must be highly reversible.
7. The cathode must be stable toward the electrolyte across the working potential.

Lithium cobalt oxide ($LiCoO_2$) is still one of the predominate materials in production, however a number of other materials have been explored and brought to market in an attempt to alleviate some of the performance and safety concerns of lithium cobalt oxide. $LiTiS_2$ [13], $LiCoO_2$ [14], $LiNi_{1-y}Co_yO_2$ [15], and $LiNi_yMn_zCo_{1-y-z}O_2$ [16] are layered structured cathode materials as seen in Figure 2-5a. These layered materials have an anion close packed lattice where the layers alternate between redox-active transition metals between which the lithium inserts itself [17]. Cubic or spinel structured materials such as $LiMn_2O_4$ are considered a special case and can be seen

in Figure 2-5b. The olivine-structured LiFePo4 can be seen in Figure 2-5c and represents a material that is gaining ground in performance and market share.

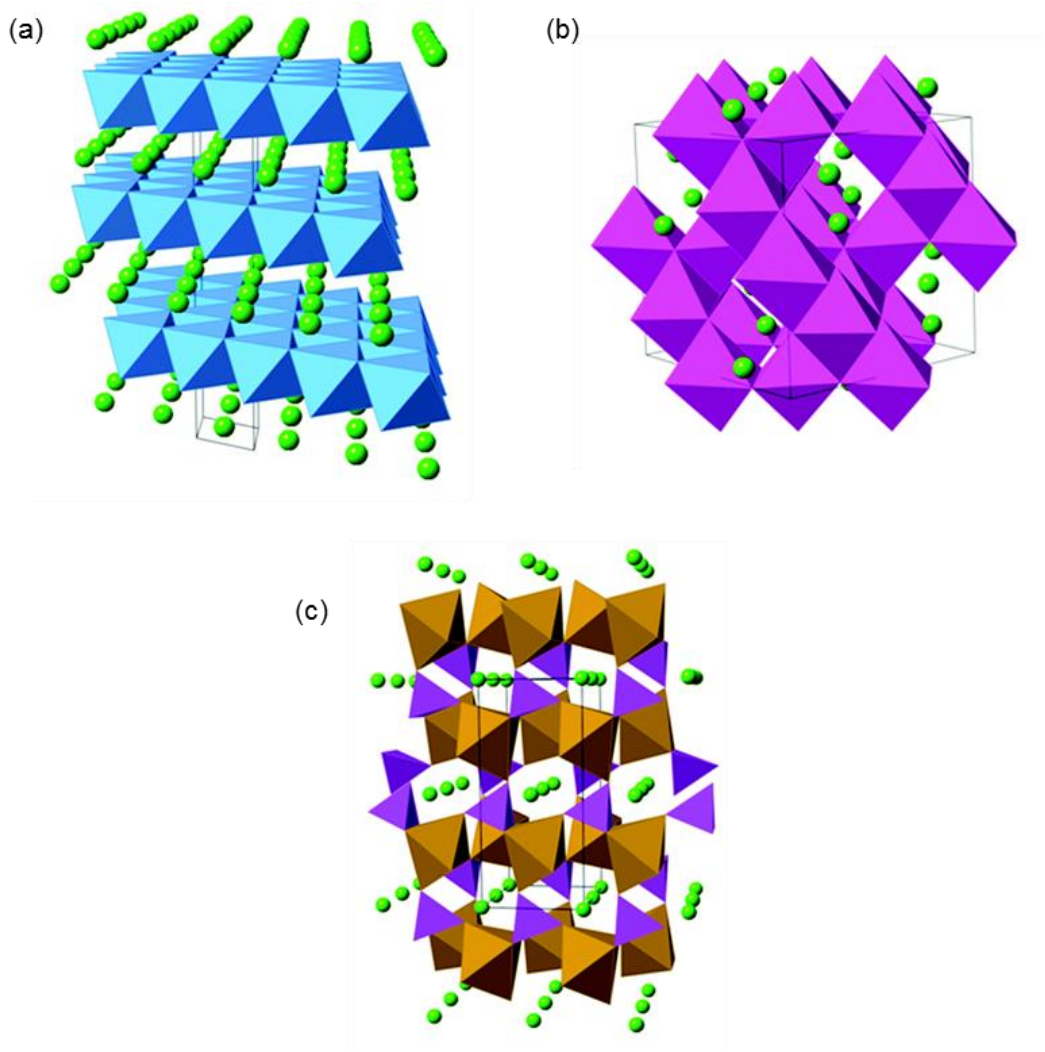

Figure 2-5 Representative crystal structures of cathode materials for lithium-ion batteries; (a) layered α-$LiCoO_2$, (b) cubic $LiMn_2O_4$ spinel, and (c) olivine-structured $LiFePo_4$ [17].

This material has a theoretical specific capacity of 169 Ah/kg and a specific energy of 590 Wh/kg and as much as 80% can be utilized in the relatively flat discharge voltage region of 3.4 V. With the introduction of carbon to the cathode

material, the cathode can reach up to 100% of its theoretical capacity at rates as high as 5C [18], [19]. With the exception of its lower operating voltage, this material performs well across all of the other desired specific characteristics of a cathode making it a material that is of particular interest in a multitude of applications.

Electrolytes

Electrolytes are key to electrochemical cells allowing an ionic path between the cathode and anode. The basic requirements of electrolytes are that they have high ionic conductivity, low melting and high boiling points, chemical and electrochemical stability, and safety. The specific requirements for lithium ion batteries are as follows [20]:

1. High ionic conductivity to minimize the cells resistance and resistive heating of the device.
2. High chemical stability to prevent decomposition of the electrolyte on the surface of reducing anode materials (metallic lithium or lithiated graphite), and highly oxidizing cathode materials.
3. Electrochemical stability to tolerate the high potential difference between the cathode and anode.
4. Low melting point to provide sufficient conductivity at sub-ambient temperatures.
5. High boiling point to provide safety and prevent explosions resulting from high pressure build-up in the cell.
6. Commercialization ease with low cost, low toxicity, and producibility.

In lithium ion batteries, the electrolyte solution must consist of a linear combination of alkyl carbonates including ethylene carbonate, dimethyl, diethyl, and ethyl-methyl carbonates (EC, DMC, DEC, and EMC) as well as electrolyte salts such as $LiPF_6$ or $LiClO_4$. The physical properties of the solvents can be seen in Table 2-2. While EC is challenging to use in wide temperature applications due to its high melting point, it has been found to be a critical components with an ability to form a passivation layer, known as the SEI on the negative electrode which protects it from further reduction of the electrolyte [21]. The proper combination of electrolyte components can be dependent of the cathode and anode material as well as the environment and cycling conditions of the cell. Each manufacture will tailor the electrolyte to provide the best performance for the application.

Table 2-2 Physical properties of selected solvents at 25 °C [20].

Solvent	Acronym	Melting Point (°C)	Boiling Point (°C)	Dielectric Permittivity	Density (g/cm3)
Ethylene Carbonate	EC	36.5	238	90.36	4.87
Propylene Carbonate	PC	-54.53	242	64.95	4.98
Dimethyl Carbonate	DMC	3	90	3.12	-
Diethyl Carbonate	DEC	-43.0	126.8	2.802	0.9693
Ethyl-methyl Carbonate	EMC	-14.5	107	-	1.01

Aging Mechanisms

Cathode Material Degradation

The nature of the LIB creates a complex and intertwined aging process that poses a challenge to properly understanding the process. It is generally understood that calendar or cycling aging can lead to or can be caused by the following [1]:

1. Changes of the electrode/at the electrolyte interface and in the electrolyte.
2. Changes of the active material.
3. Changes of the composite electrode (current collector, active materials, conductive additives, binder, porosity, etc.).

Cathode materials can have a significant effect on the performance and aging of lithium ion cells in both calendar and cycling conditions. Figure 2-6 illustrates a basic overview of the dominant aging features including changes occurring with the inactive components (binder, current collector, etc.), as wells as the lithium metal oxide. These effects are heavily dependent on the design and production of the cathode material and are truly intertwined making it difficult to examine each independent of the other. Generally, these mechanisms can be grouped into three categories [1]:

1. Structural changes during cycling.
2. Chemical Decomposition/dissolution reaction
3. Surface film modification

These degradation categories are heavily dependent on state of charge, cycling conditions, and temperature of the cell. Additionally, the intercalation/deintercalation process induces a mechanical strain on the oxide particles as the volume of the

material changes. This strain can cause the micro-cracking, loss of contact, and continued surface layer formation.

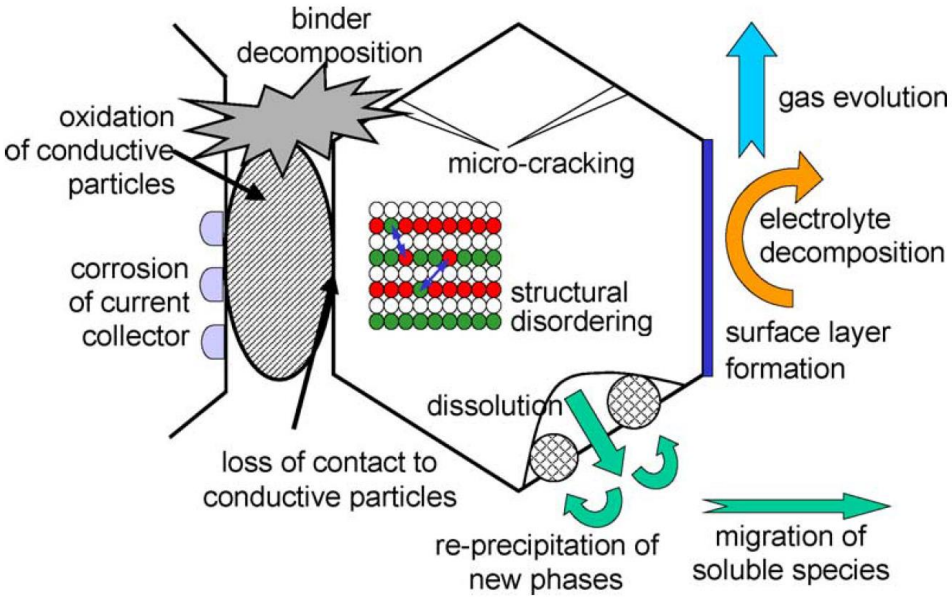

Figure 2-6 Overview on basic aging mechanisms of cathode materials [1].

The flow diagram shown in Figure 2-7 gives an overview of the current understanding of aging mechanisms with regard to lithium ion cathode materials [11]. Again, a separation of the inactive components and the lithium metal oxide demonstrates the two primary degradation paths. However, all of these mechanisms result in an impedance increase, capacity fading, or gas evolution.

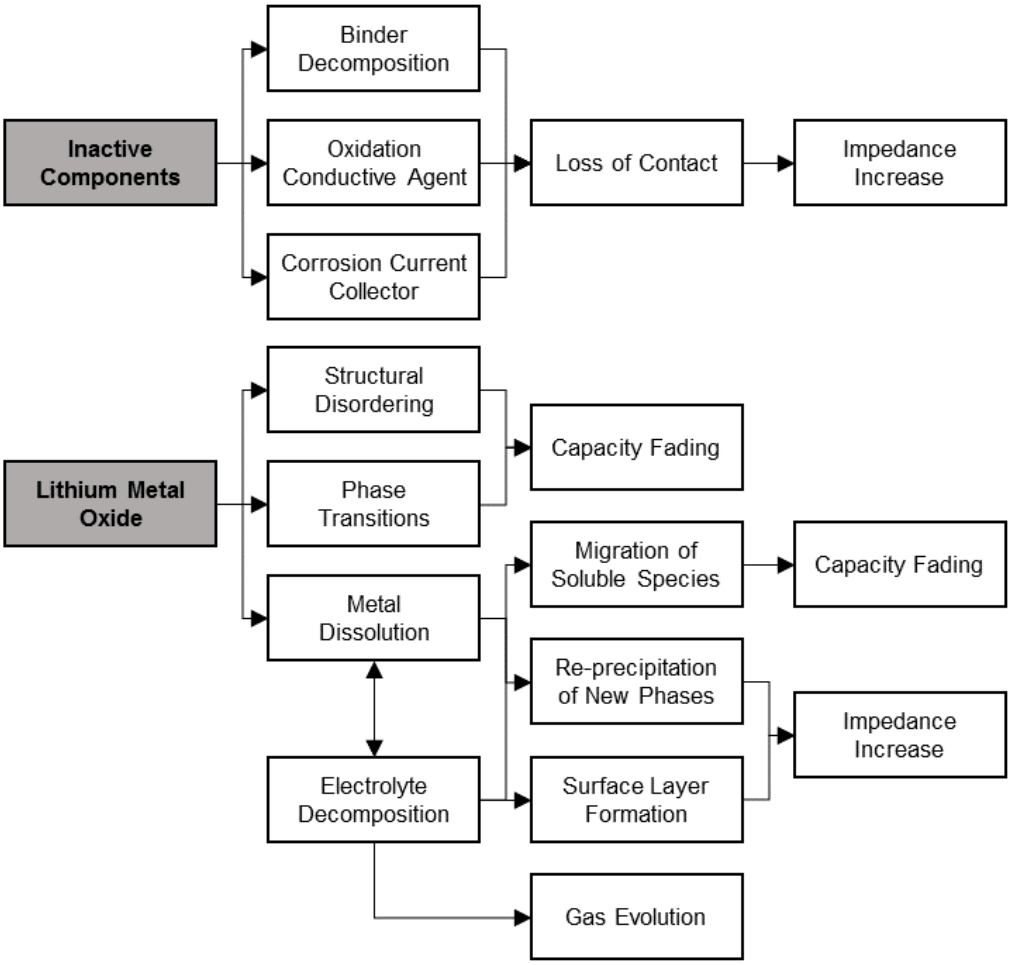

Figure 2-7 Cause and effect of aging mechanisms of cathode materials [11].

Anode Material Degradation

While there has been much research focused on LIB aging, the majority has focused on the changes that occur at the electrode/electrolyte interface because it is considered to be the primary source for aging at the anode [22]. Figure 2-8 illustrates the primary interactions that take place at the interface including graphite exfoliation and cracking, electrolyte decomposition and SEI formation, SEI conversion, SEI

dissolution, and lithium plating and corrosion. It is well understood that the anode operates at voltages outside of the electrochemical stability of the electrolyte resulting in an irreversible reductive decomposition of the electrolyte at the interface. This reaction results in a buildup of decomposed electrolyte on the surface of the anode that is known as the SEI layer. This buildup typically takes place when the cell is first cycled and prevents continued reduction of the electrolyte. While the SEI allows the intercalation/deintercalation of lithium ions to and from the anode, it slows the transport increasing the cells total resistance.

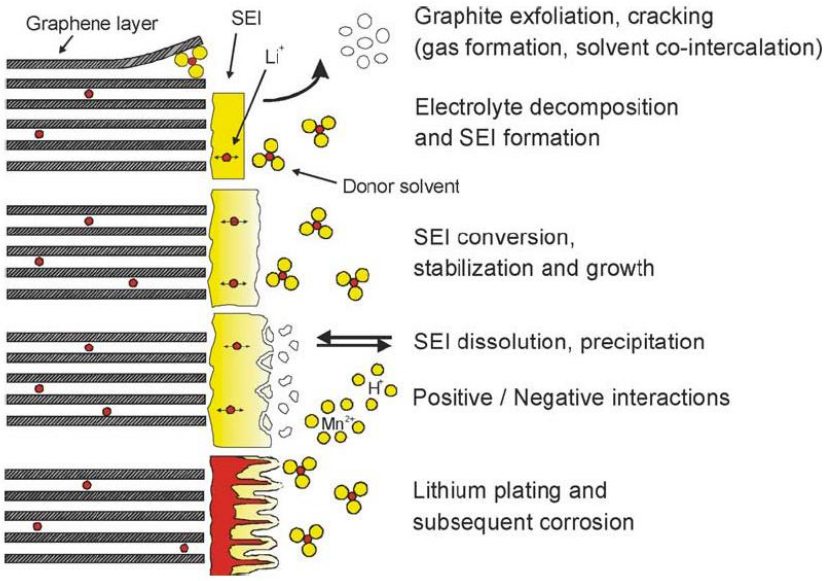

Figure 2-8 Changes at the anode/electrolyte interface [1].

Examples of the complex and intertwined aging mechanisms are shown in Table 2-3. This table is an examination of the principal aging causes and effects of the lithium-ion carbon based anode. While the primary causes of aging at the anode occurs at the electrode-electrolyte interface, Table 2-3 demonstrates several of the contributing factors that can complicate the proper discernment of capacity and power fade with regard to a specific cause.

Table 2-3 Lithium-Ion anode aging and effects [1].

Cause	Effect	Leads to	Enhanced by
Electrolyte decomposition	Loss of lithium, Impedance rise	Capacity fade, Power fade	High temp High SOC
Solvent co-intercalation, gas evolution, cracking formation in particles	Loss of active material (graphite exfoliation), Li loss	Capacity fade	Overcharge
Decrease of accessible surface area due to continuous SEI growth	Impedance rise	Power fade	High Temp High SOC
Changes in porosity due to volume changes, SEI formation and growth	Impedance rise, Over-potentials	Power fade	High cycle rate High SOC
Contact loss of active material particles due to volume changes during cycling	Loss of active material	Capacity fade	High cycle rate High DOD
Decomposition of binder	Loss of lithium, Loss of mechanical stability	Capacity fade	High SOC High temp
Current collector corrosion	Over-potentials, Impedance rise, Inhomogeneous distribution of current and potential	Power fade, Enhances other aging mechanisms	Over-discharge Low SOC
Metallic lithium plating and subsequent electrolyte decomposition by metallic Li	Loss of lithium (Loss of electrolyte)	Capacity fade (power fade)	Low temp High cycle rate Poor cell balance Geometric misfits

The table also lists the features that enhance these degradation factors including high cycling rates. Cycling these cells at elevated cycle rates heightens the impedance rise of the cell through electrode volume changes which leads to changes in the material porosity. The impedance rise can also derive from an accelerated

formation and growth of the SEI layer which slows the intercalation of Li^+. High cycling rates will also increase the capacity of the cell through the loss of active material or the loss of lithium. The electrode volume change during cycling leads to material cracking which can separate the active material particles causing contact loss. Metallic lithium plating at the electrode surface causes a loss in capacity due to the reduction of useable Li^+. This process also leads to an accelerated rate of electrolyte decomposition.

Aging Effects

As previously mentioned, there are a number of different causes for aging within a lithium ion cell, and all result in a capacity fade, power fade, and/or gas production. With that said, the slow electrochemical process that forms the SEI at the anode is believed to have the largest impact and leads to impedance rise at the anode. This SEI formation and growth process is tightly coupled with the complex chemical reactions within the electrolyte and results in gas production within the battery [23]. Results from a study utilizing differential electrochemical mass spectrometry and subtractively normalized interfacial Fourier transform infrared spectroscopy demonstrated that the gas generation at the anode is the dominate source of generation within an LIB [24]. Studies also demonstrated that the gas generation continued within the battery even after the initial SEI formation had occurred and that the gas generation is increased by high temperatures and cell potential [25], [26]. While the gas generation itself can result in performance degradation due to the reduction of interfacial area between the active material and the electrolyte [26], its production is also a result or indicator of many other performance degradation processes. In addition

to the gas generation within the cell, mechanical deterioration can occur from volume changes that result in crack formations and contact loss of active material. Winter performed dilatometric investigations confirming this volume change during the intercalation/ deintercalation process [27].

Previously Documented Results

The study of evolved gases in the li-ion system has been studied in connection with various aspects of cell operation. The primary areas of investigation have focused on the evolution of gases during the initial development of the SEI layer [28], and the evolution of gases during extreme conditions such as over-discharge [29]–[31], over-charge [32]–[34], and thermal runaway [35]–[38]. Few studies examine the generation of gas during life cycle testing, and fewer still study this in commercially available cells. The following studies conducted by Kumai and Kong examine gas production of cells cycled at low rate as well as slight over and under potentials.

Gas Generation Mechanism Due to Electrolyte Decomposition

In 1999, Kumai et al. conducted a study examining the decomposition of electrolyte in commercial $Li_xC_6/Li_{1-x}CoO_2$ one ampere hour (Ah) cells. The cells were cycled at nominal voltage ranges at rates extending from C/5 to C/2 for 2000-3000 cycles until their capacity had faded by half. The volume and composition of the generated gasses was then measured and identified. In addition to the nominally cycled cells, a further set of cells were cycled at 5% overcharge, and 10% over-discharged for 880 cycles resulting in significantly more gas being generated. Figure 2-9 shows the amount of gas generated in the cells across the nominal, overcharged,

and over-discharged regions as well as the relationship between the volume of hydrocarbons to that of CO_2. The cells that were cycled at low rates produced small amounts of gas that were mainly hydrocarbons. Both the overcharged and over-discharged cells showed both hydrocarbon and CO_2 production with the over-discharged cells producing a higher amount of CO_2.

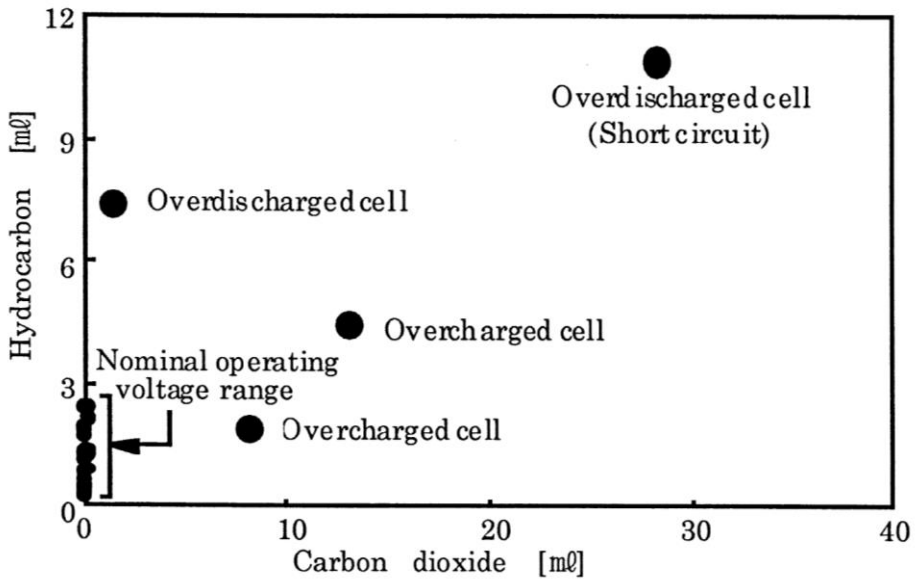

Figure 2-9 Relationship between the generated hydrocarbons and carbon dioxide [5].

The authors developed a process for the gas generation mechanism and it is demonstrated in Figure 2-10. This figure elucidates the large volume of gas generation during overcharge and over-discharge, the large compositional change to the electrolyte, and that different decomposition reactions occur in each of the three regions [5]. The nominal operating range produced compositional changes that were primarily due to the ester exchange. Both the over-charge and over-discharge conditions produced a considerable amount of gases due to electrolyte decomposition with each involving a different decomposition process.

The authors were the first to quantify the gas production inside the cells while being cycled and also established the gas generation mechanism in each region. Nominal cycling was primarily dependent on the slow decomposition of the electrolyte with the anode. Over-charge cycling included the decomposition of the electrolyte as well as the release of O_2 from the decomposition of the overcharged cathode material. The over-discharged cells were found to have copper plating on the cathode reducing the cathode charging and accelerating the electrolyte decomposition producing both hydrocarbons and CO_2.

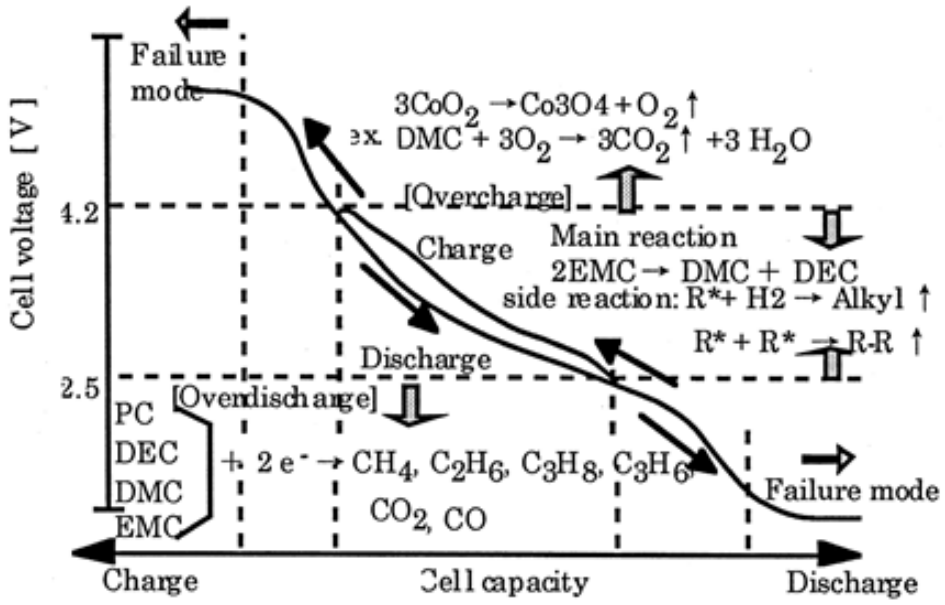

Figure 2-10 Gas generation model of Li-Ion cells during expanded voltage profiles [5].

Gas Evolution of Various Cathode Materials

A related study conducted by Kong et al. in 2005 examined the gas evolution behaviors of three different lithium-ion chemistries, $LiCoO_2$ (1.1 Ah), $LiMn_2O_4$ (0.7 Ah),

and $LiFePO_4$ (1.0 Ah) at nominal voltage ranges and overcharge conditions. Each of the cells were constructed in the laboratory utilizing commercially available materials. In this study the cells were cycled three times at a rate of C/5 and then floated at their max nominal or overcharged voltages. The gas was then extracted from the cells and evaluated for composition. Results found that under nominal conditions gas generation behavior was not dependent on the cathode material. However, in the overcharged condition the cathode material made a significant difference in the volume and type of gas produced due to the oxidation ability of each cathode material [39].

Figure 2-11 illustrates the gases produced under different charging voltages for the $LiCoO_2$/CMS battery. It can be seen that the same species of gases were produced with the 4.2 V, 4.5 V, and 5.0 V charging voltages, however the amount of gases produced increased with the elevated charging potential. This is of particular note for the production of CO_2 at higher potentials which corresponds to the work conducted by Kumai et al. This is a result of the increase in O_2 generated at higher potentials due to the decomposition of the $LiCoO_2$ cathode. The amount of gas and the type of gas species are significantly influenced by the oxidation ability of the cathode materials in over-charge conditions. The oxidation ability of the three cathode materials tested is LiCoO2 > LiMn2O4 > LiFePO4 which corresponds to the understood safety order. However, while $LiFePO_4$ may have a lower oxidation ability than $LiCoO_2$, it produced a considerable amount of C_2H_2which is combustible [39].

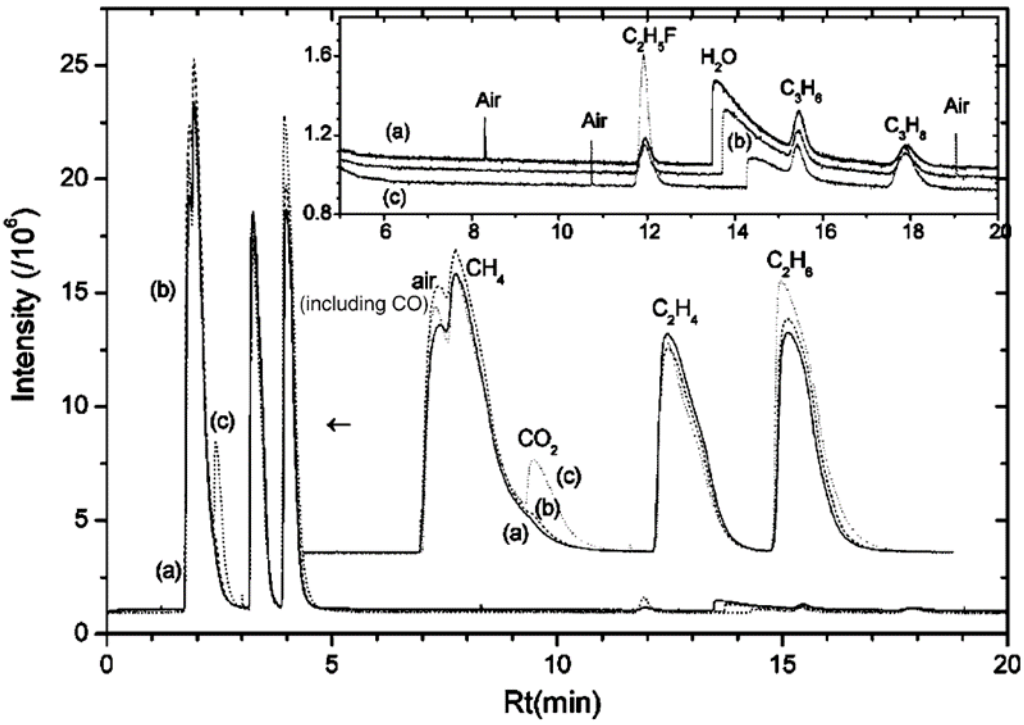

Figure 2-11 The gas-chromotography of the CMS/LiCoO2 battery under different charging voltages (a) 4.2 V (solid), (b) 4.5 V (dash), (c) 5.0 V (dot). Species marked in figure are determined by corresponding mass spectroscopy results [39].

Research Overview

It is clear that the aging of li-ion batteries is a complicated interrelated process of structural degradation, chemical changes to the electrodes, and surface layer formation at the electrode-electrolyte interface, and that these degradation mechanisms can be enhanced by temperature, SOC, DOD, over-charge, over-discharge, and cycling rate. This research examined the effects of over-discharge and high rate cycling on the aging of li-ion cells, and identified an alternative method of predicting aging. This method examined the in-situ pressure evolution of cells and

attempted to correlate the pressure evolution to aging or failure. Three studies were conducted to assess the internal pressure evolution:

1. Single cycle internal pressure evolution
2. Over-discharge behavior of various lithium-ion batteries
3. Correlation of internal pressure rise and capacity degradation

These studies examined the micro and macro pressure behavior inside the cell, and also identified the evolution of pressure during a damaging over-discharge event. Conventional non-destructive diagnostic tools such EIS, capacity, and DC ESR, along with destructive analysis like GC-MS, and SEM were utilized to examine the aging phenomenon and correlate the behavior to the pressure evolution within the cell.

Chapter 3

Experimental Setup

Test Hardware

Pressure Chamber

In order to conduct a study that would be capable of evaluating the evolution of gas produced by a lithium ion cell while being cycled, a test chamber would need to be assembled with the following qualities:

1. A sealed system that would not allow gas exchange to the external environment.
2. An inert system that would not react with the solvents contained in the electrolyte or with the gases produced.
3. A rigid system that would not significantly expand or contract due to pressure or temperature variations.
4. A system that would allow for the temperature measurements of the cell.
5. A system that would allow for high rate cycling of the cell without a significant increase or change in measured impedance.

With these requirements in mind, a commercially available split cell chamber produced by the MTI Corporation was initially selected for testing and can be seen in Figure 3-1. The primary chamber components consisted of stainless steel bottom and top endcaps and a Polytetrafluoroethylene (PTFE) body. The body was mated to the endcaps, sealed with a top and bottom o-ring, and held together with three vertical screws. This design allowed for a 26650 form factor battery to be sealed inside of the chamber while the end caps made contact with the positive and negative terminals of

the battery. Finally, a pressure transducer was mated to the chamber to allow for the internal pressure to be measured. The design of this system accomplished three of the five requirements, but failed to allow for the measurement of the cell temperature, and also properly contain the gases produced over long term cycling.

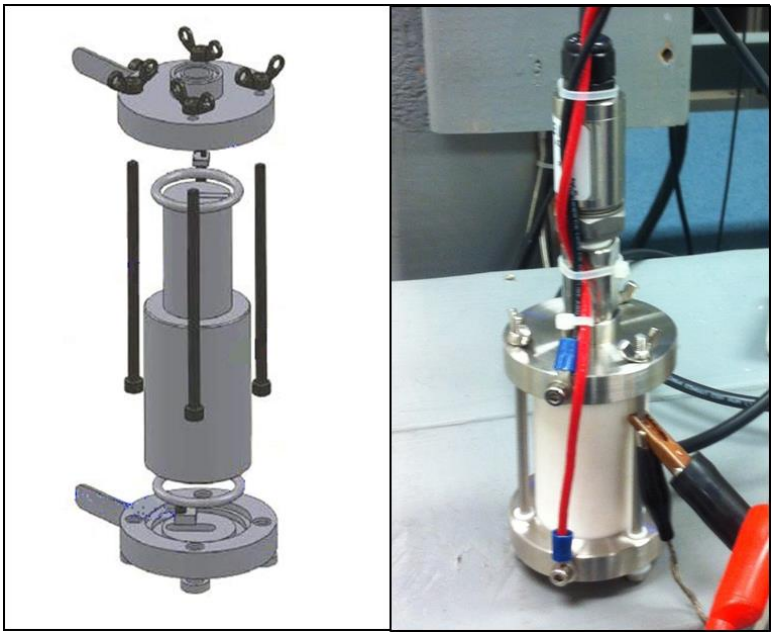

Figure 3-1 Modified commercial test chamber for evaluating gas evolution.

Due to the restrictions of the commercial chamber, a custom designed test chamber was manufactured to examine the pressure evolution of a single 26650 form factor LIB at elevated cycling rates over a complete life cycle. Figure 3-2 illustrates a computer-aided design (CAD) image of the custom battery test chamber as well as photographs of various features of the constructed test chamber. The chamber was constructed with corrosion resistant 316 stainless steel end caps, and mated with dual O-rings (Figure 3-2c) to the virgin PTFE cylinder for gas containment as well as electrical isolation from the positive and negative end caps connected to the battery. National Pipe Thread (NPT) taps were included in the end caps to allow for the

pressure transducer, multi-thermocouple feed through, battery puncture needle, and external valve to be connected to the chamber with minimal deadspace. The PTFE cylinder has vertical grooves cut on the inside radius (Figure 3-2d) in order to accept the stainless steel clad thermocouples and place them firmly along the external case of the battery. Finally, a needle was designed (Figure 3-2f) to screw into the top end cap and puncture the battery's pressure release cap while it is sealed inside of the test chamber in order to capture the initial release of gas.

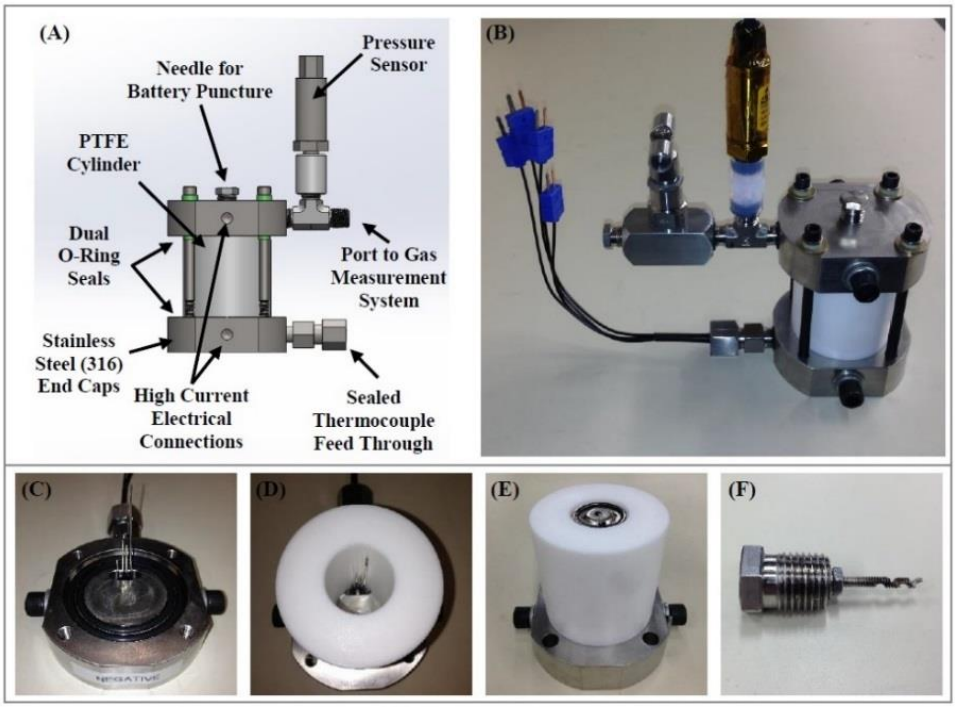

Figure 3-2 (A) CAD drawing of the custom battery test chamber, (B) photograph of assembled test chamber, (C) negative endcap with o-rings and thernocouples, (D) thermocouple grooves, (E) Battery inserted into chamber. And (F) puncture needle.

While the custom LIB test chamber was a significant improvement over the commercially available chamber, two issues remained. The first issue with the chamber was a small leak that became apparent after weeks of cycling. The second issue

concerned the amount of deadspace present in the chamber and its effect on the ability to detect small pressure changes. In order to remedy the first issue, the body was replaced with a fused quartz cylinder in order to make a better seal to the o-rings. A PTFE sleeve was placed inside of the quartz to allow for the thermocouple grooves. In order to decrease the deadspace, the puncture needle was removed and the pressure transducer was transferred to this center port. This change required that the cell be punctured in an inert glove box and then sealed inside the test chamber. Figure 3-3 demonstrates the modifications to the test chamber, and the final design.

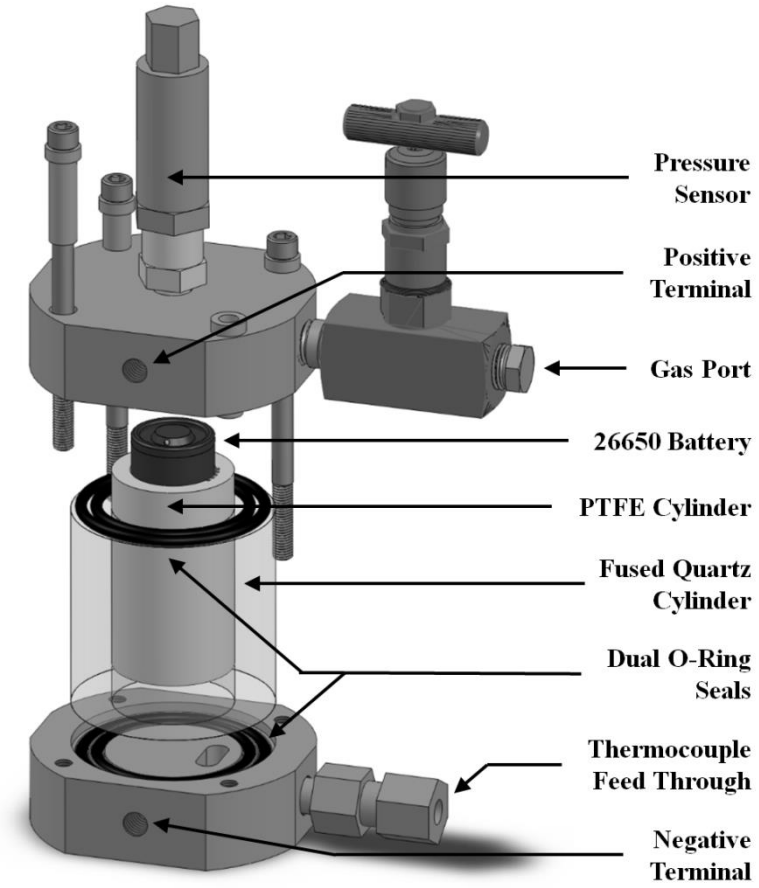

Figure 3-3 Modified custom battery test chamber designed to examine in situ pressure evolution of commercial LIBs.

Gas Extraction

In order to examine the gases produced at the conclusion of the cycling process, the chamber was reconfigured (Figure 3-4) to allow the gas to be sampled. The plug was removed from valve 1, and a tee with two additional valves was attached to valve 1. A threaded PTFE mininert valve was attached to valve 3 providing a septum to extract the gas via an airtight syringe. In order to extract a clean sample from the chamber, valves 1 and 3 were closed and a vacuum pump was connected to valve 2 to clear the tee. Valve 2 was then closed, and valve 1 opened to allow the chamber gas to enter the tee. Valve 3 could then be opened and the needle of a gas tight syringe could be inserted into the septum of the mininert valve allowing for a clean sample extraction. This modification was made at the conclusion of cycling and the process was used each time a sample was extracted for gas analysis.

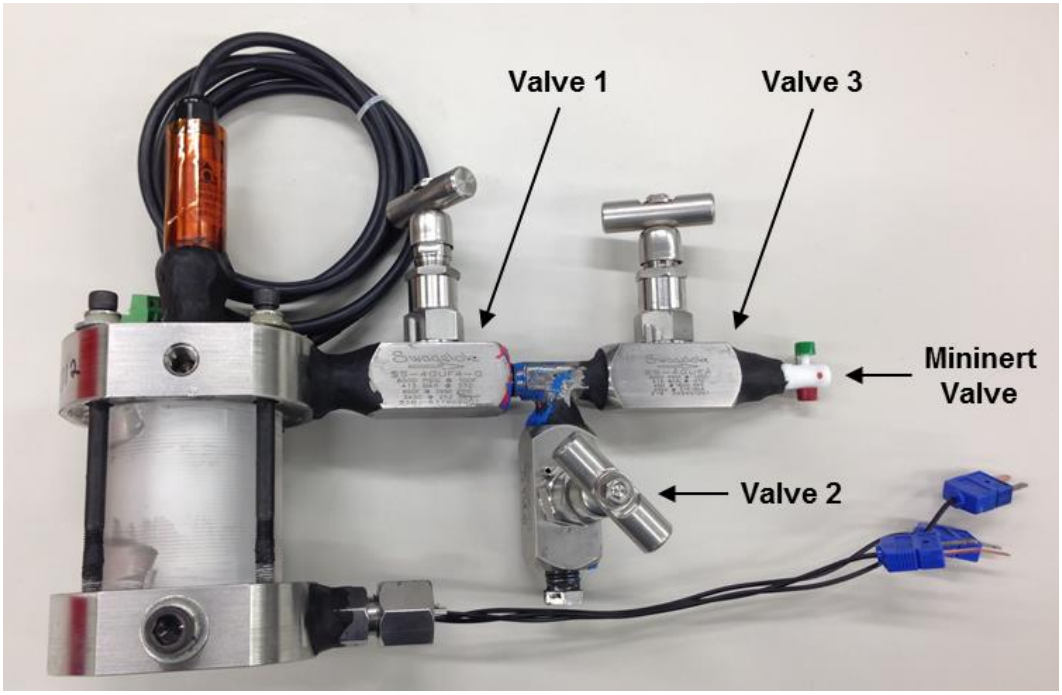

Figure 3-4 Gas extraction system configuration.

Experimental Control and Monitoring

Battery Cycler

When cycling the cells in a conventional manner, a commercially available Junsi iCharger 4010 Duo was used. The iCharger is a high power battery cycler capable of providing 40 A continuously in either charge or discharge modes. The cycler is programmable allowing for a constant current discharge and a constant current / constant voltage charge profile. The iCharger is equipped with a 4-wire configuration utilizing two wires to transfer current, and two wires for remote voltage sensing allowing for a small voltage drop and thus a higher accuracy voltage sense capability. The cycler contains protection for reverse polarity, voltage and current ranges, cell temperature, and cell capacity. Additionally, the cell voltage, current, temperature, and capacity is continuously recorded at a rate of 2 samples/second.

A Metrohm PGSTAT 302N potentiostat / galvanostat was used for tests requiring high accuracy or tests outside of the safety voltage range of the iCharger. The PGSTAT has a voltage range of +/- 10 V, and a current range of 10 nA to 2 A (20 A with a booster). It is also equipped with a 4-wire configuration utilizing two wires to transfer current, and two wires for remote voltage sensing allowing a voltage and current accuracy of +/- 0.2%. The hardware is connected to a computer via USB, and is controlled with the NOVA software package. The control software allows charge and discharge profiles to be programmed and also records the relevant voltage, current, capacity, and resistance data at extremely high rates.

Environmental Chamber

Two identical custom designed environmental test chambers were built to maintain a constant temperature environment for the cells under test. The chambers were constructed with 2 in thick foam insulation board with an internal chamber size of 2.3 cubic feet (Figure 3-5a). A 12 V, 90 W thermoelectric air-to-air heat exchanger with aluminum heat sinks and fans chamber (Figure 3-5b) were used to remove heat from the chamber. A TE Technology TC-48-20 PWM temperature controller (Figure 3-5c) was used to regulate the heat exchanger, employing a PID loop sensing the temperature near the internal heat sink with a thermistor. The system was capable of maintaining the chamber temperature at +/- 0.3 °C when measured at the thermistor after system stabilization.

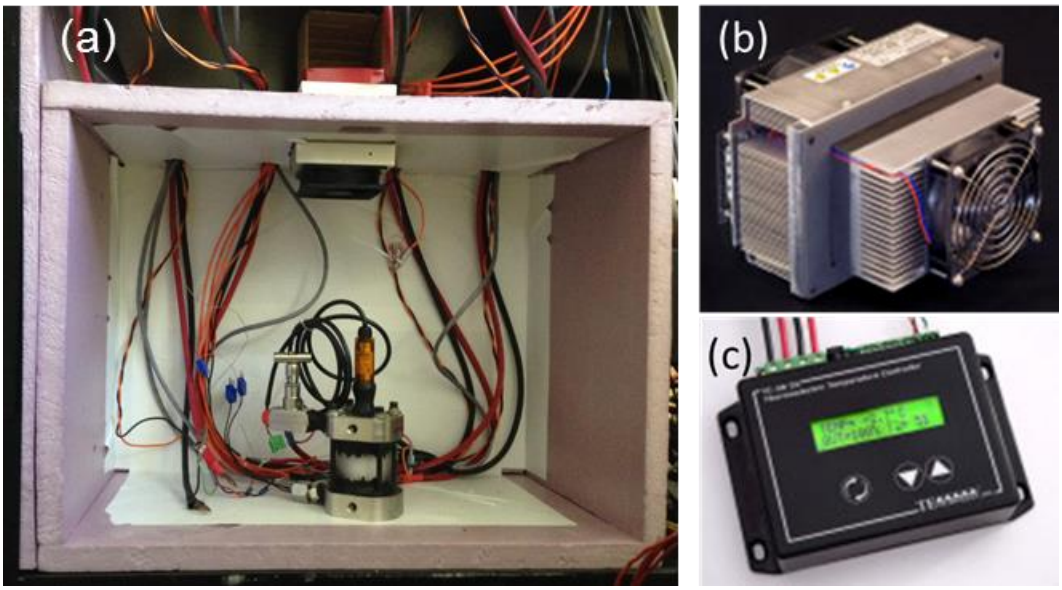

Figure 3-5 (A) Custom designed environmental test chamber, (B) thermoelectric air-to-air heat exchanger, and (C) TE Technology TC-48-20 PWM temperature controller.

Data Acquisition

A diagram of the test setup with requisite control and data acquisition is displayed in Figure 3-6. Differential inputs on a National Instruments NI-9205 analog voltage module were utilized to capture the cell voltage and the voltage outputs of both the current and pressure transducers. The ambient temperature in the environmental chamber as well as the temperature of the cell measured at the outer case near the top, middle, and bottom of the cell utilized 0.040 inch diameter, stainless steel clad T-type thermocouples. The temperature data from these thermocouples was collected with a NI-9213 thermocouple input module. Both the NI-9205 and NI-9213 data acquisition cards were loaded into a NI cDAQ-9184 4 slot chassis which streamed the collected data back to the data acquisition computer.

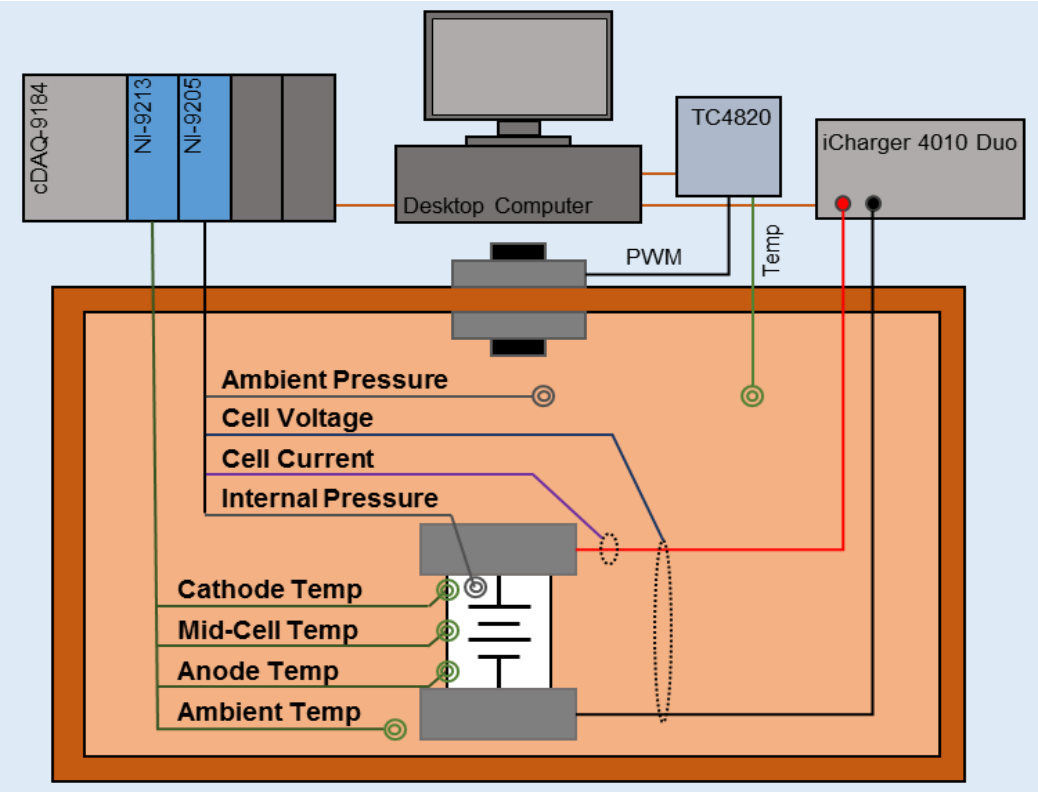

Figure 3-6 Data acquisition setup for cycle life testing of cells.

A Labview program was created on the computer to enable data monitoring during testing, and to serve as a data acquisition system. The telemetry for each cell was monitored and recorded to include terminal voltage, current flow, internal pressure, and temperature at the top, middle, and bottom of the case. Additionally, the environmental chamber temperature, and pressure were also captured. Each of these datasets were continuously recorded on the computer at a rate of 10 samples/sec in order to capture the necessary transient behavior of each variable in the system.

Chapter 4

Experimental Preparation and Procedure

Cell Transfer

The puncture of the cell and the subsequent transfer into the test chamber is an important step in the testing process. The electrochemical system is particularly susceptible to contaminates during manufacturing, and steps are taken to ensure not only the purity of the components being assembled, but also the environment in which it is assembled. Cells are typically assembled in a dry room or dry box where the moisture has been effectively removed in order to avoid contamination of the cell [40].

Similar to the manufacturing process, care must be taken during the puncture and transfer of the cell so as to avoid introducing new contaminates to the system. In order to accomplish this goal, all transfer procedures were conducted in a glove box filled with high purity argon (99.9%) where the oxygen and moisture levels were kept below 1 ppm (Figure 4-1). The system was equipped with a transfer chamber located on the right side of the glove box that enabled samples to be moved in and out. The system utilized a MTI PPM Grade Dual Column Inert Gas Purifier capable of reducing gaseous impurities (H_2O, O_2, CO, CO_2, and H_2) in the Argon to sub-ppm.

In order to prepare the battery and test chamber for transfer, all surfaces were cleaned to remove any external contaminates. All stainless steel components of the test chamber were disassembled and cleaned in a Branson 5510 precision ultrasonic cleaner with a MC-1 metal cleaner solution heated to 55 °C. The ultrasonic cleaner removes oils, and other contaminates from the steel surface. After the ultrasonic

cleaning, all parts were rinsed and manually cleaned with acetone. The test cells were also cleaned with acetone to remove any contaminates from the outside of the cell.

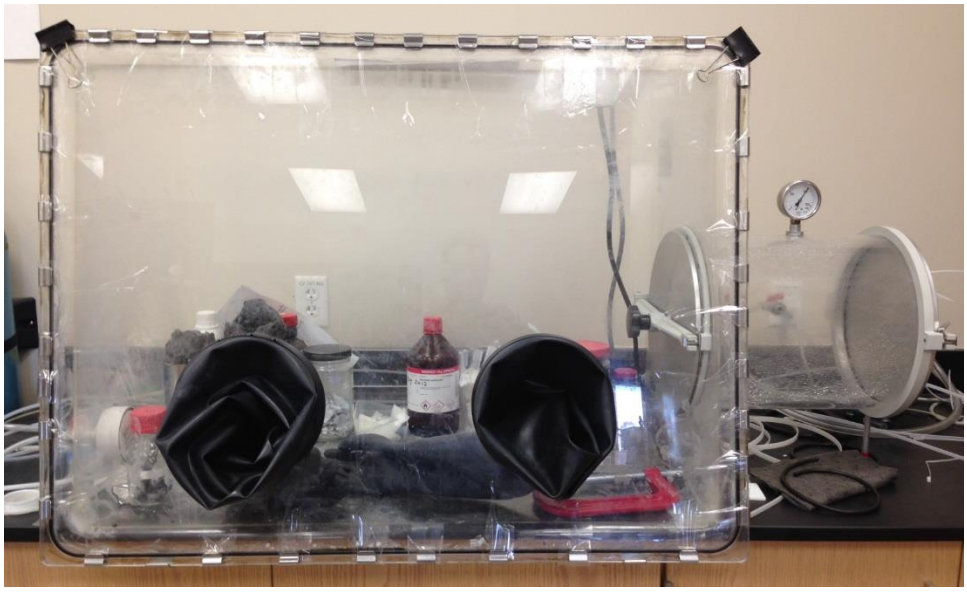

Figure 4-1 Sealed glove box filled with high purity argon.

Before transfer into the glove box, a 6 mm hole was drilled at the center of the positive terminal cap of the cell to allow for the pressure cap to be removed. After transfer into the inert environment of the glove box, the pressure release cap seen in Figure 4-2 was carefully cut away from the top assembly and removed through the 6 mm hole in the positive terminal. This procedure allowed for the free flow of gases from inside the cell to test chamber while still allowing for a solid electrical connection between the positive electrode and terminal.

The cell was then placed into the PTFE cylinder of the test chamber seen in Figure 3-3. Careful placement of the cell into the cylinder allowed for the three thermocouples to be located along the top, middle and bottom of the outer casing of the cell. The top assembly of the test chamber was then fitted with the upper o-rings and placed on the top of the quartz and PTFE cylinders. The four bolts were then fitted

into the system and methodically tightened to avoid an improper seating. Blue Locktite was used on the threads of the bolts to ensure that the assembly remained stationary. As a precaution, a self-setting rubber adhesive capable of bonding to steel, ceramics, and glass was used to line all interfaces of the test chamber.

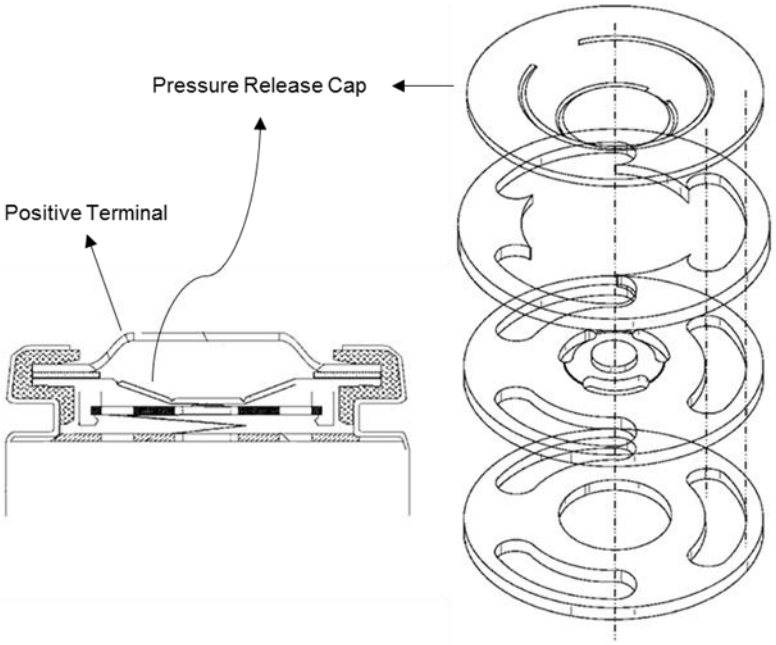

Figure 4-2 Top assembly of a 26650 form factor cell [41].

Baseline Procedure

Each study conducted as part of this research utilized a baseline procedure in order to establish the performance of the cell under test. While the baseline procedure varies depending on the study, each study periodically uses a procedure to examine the evolution of the cell performance based on the original baseline. This analysis enables an insight into the degradation mechanisms occurring during the study. The baseline procedures include measuring the cell's EIS, DC ESR, and 1C discharge capacity

Impedance Spectroscopy

Due to the complicated nature of LIB aging processes, EIS has emerged as the primary nondestructive test method for evaluating the effects of lithium-ion battery aging [42]–[45]. This method examines the impedance of the electrochemical system over a range of frequencies and determines the system response including capacitive and resistive characteristics. This data is typically viewed graphically in Bode or Nyquist plots (Figure 4-3b) where shifts in frequency response can be identified and correlated to aging mechanisms of specific components as the battery ages [46]. Figure 4-3a illustrates the kinetic steps involved including the electronic conduction from the current collector through the particles, and the subsequent ionic conduction through the electrolyte that is in the cavities between the particles. Charge transfer at the surface of the particles involves the resistance of the insulating layer as well as the activated electron transfer resistance on the electronic/ionic conduction boundary [47], [48]. Finally, the ions must diffuse into the bulk particles via solid-state diffusion. Figure 4-3b examines the resulting impedance of this process and matches the frequency range with the requisite process. In addition to the processes described other events such as the formation of new crystalline structures can become limiting kinetic steps below 1 mHz [48]. The ability to identify and measure changes in these processes allows EIS to aid in diagnosis of aging phenomena.

Because EIS can shed light on the internal changes within a cell, the method was used to baseline the performance of the cells throughout each study. In order to examine a commercial cell non-destructively, a two-electrode setup was utilized. The cell was charged to 100% SOC and allowed to relax in order for the electrochemical system to reach equilibrium. A Metrohm PGSTAT 302N potentiostat was used to apply

a fixed DC potential, and the Metrohm FRA32M frequency response analyzer was used to superimpose a sinusoidal potential perturbation on the DC potential applied to the cell. The current measured from the applied sinusoid was used to determine the impedance of the system at various frequencies. The frequency of the applied sinusoid is limited by the potentiostat, the test setup, and the electrochemical system. The test setup that was utilized in these studies collected data using a 10 mV amplitude potential with a frequency sweep over the range of 2 kHz to 15 mHz.

Figure 4-4 illustrates a typical evolution of EIS spectra for a $LiCoO_2$ cell as it is cycled. The EIS curve begins with a semicircular arc at the middle frequencies followed by a sloped diffusion tail at the lower frequencies. The Ohmic resistance (R_S), or the high frequency intercept with the real axis (Z'), is representative of the electrolyte resistance, electronic resistance of active particles, the contact resistance between the measurement instruments the test chamber and the battery [49]. The middle frequency arc is related to two processes occurring at the electrode-electrolyte interface, namely the SEI resistance (R_{SEI}) coupled with the SEI capacitance (C_{SEI}), and the charge-transfer resistance (R_{CT}) paralleled with the double-layer capacitance (C_{DL}). At the onset of cycling, the two processes are indistinguishable as there is a singular middle frequency arc. However, the single arc begins to transition into two separate arcs at cycle 75 and becomes more apparent at cycle 150. The semicircular arc is followed by a 45° slope behavior at low frequency that is indicative of the Warburg impedance corresponding to semi-infinite diffusion. While it is not possible to positively identify the contribution of each electrode to the overall EIS spectrum without a three electrode or split cell setup, the full cell EIS data coupled with the other analysis can provide insight.

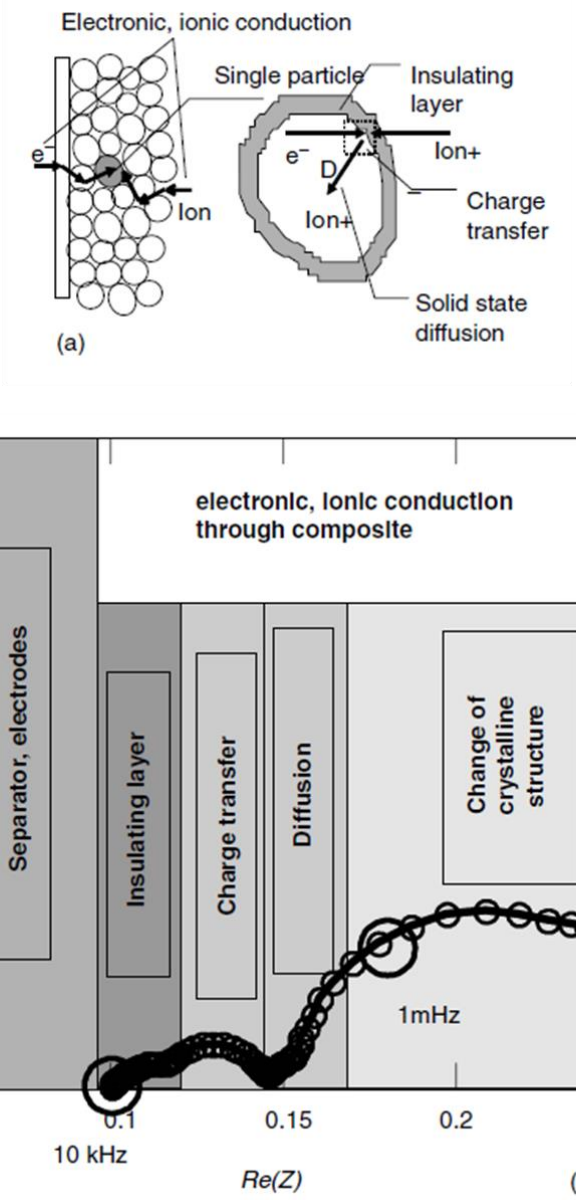

Figure 4-3 (a) Kinetic steps common in most batteries; (b) typical impedance spectra of intercalation material [47].

Key parameters from the EIS measurements can be extracted and used to model the response of the system using an equivalent circuit such as the one illustrated in Figure 4-5. Non-linear regression of the model is then used to analyze the

data and estimate the model parameters for each EIS spectra. This process allows each set of EIS data to be compared as the cell is cycled, and the estimated model parameters can be compared to identify any shift. This shift can be used to elucidate changes in impedance for the Ohmic resistance (R_S), the SEI resistance (R_{SEI}), the SEI capacitance (C_{SEI}), the charge-transfer resistance (R_{CT}), the double-layer capacitance (C_{DL}), and the Warburg impedance [49]–[51].

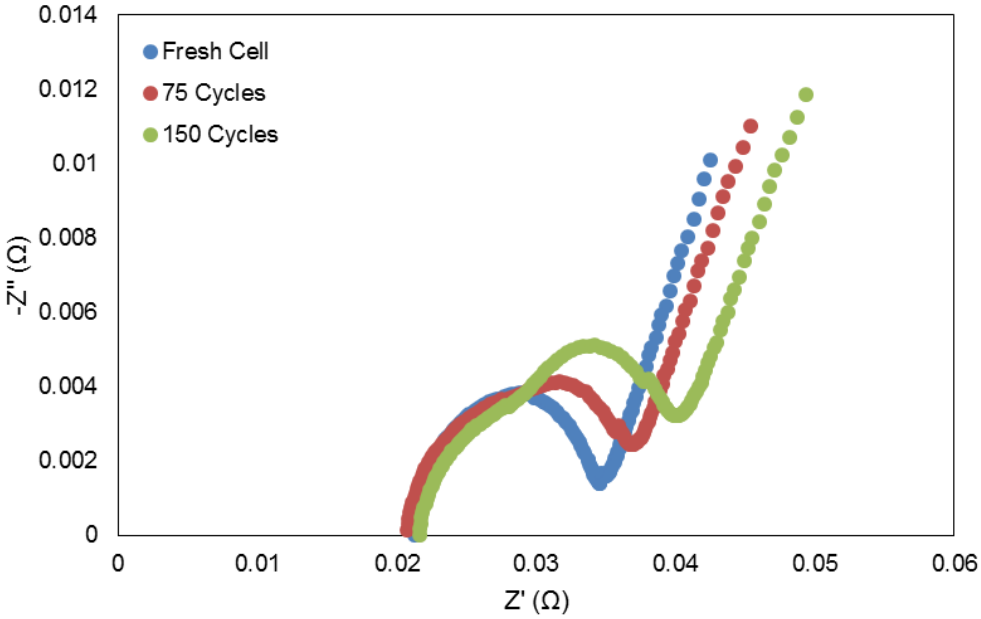

Figure 4-4 Typical EIS curve of a LiCoO2 cell at various cycling intervals.

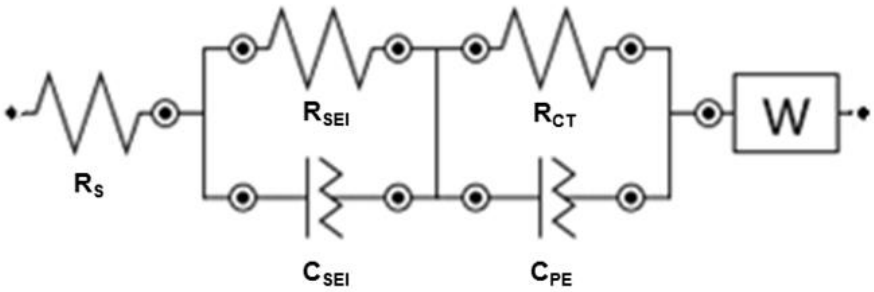

Figure 4-5 Modified Randles equivalent circuit.

While EIS measurements can assist in the identification of many of the mechanisms responsible for battery aging, properly deciphering the impedance data of a two electrode system can be unclear and challenging in its own right. As a result, EIS is typically coupled with other more conventional methods for evaluating battery aging including changes in internal resistance, capacity, potential, and cumulative charge/ discharge cycles [42]. Although the coupling of EIS with more traditional methods is the primary nondestructive method for examining the internal changes within a lithium-ion battery, no results obtained thus far using these methods is proven as the perfect solution and therefore complementary solutions are needed for determining and predicting the aging/failure mechanisms that result from high rate discharge.

DC Equivalent Series Resistance

The internal resistance of a cell is an important factor in understanding its ability to deliver high power or high rate over the life cycle of the cell. The heat evolution and energy efficiency of the cell under high current loads are also primarily determined by the cell ESR. The resistance of a cell is typically determined using Ohm's law by applying a current to the device and measuring the voltage. Impedance spectroscopy uses this method to determine the small signal resistance of the non-linear time invariant system while methods like the Advanced VDA are used to determine the large signal resistance of the cell [52].

While the Advanced VDA method is only one of a number of methods used to determine the ESR of a cell, it has been found to be quick and efficient while not transferring a significant amount of energy to or from the cell. The discharge ESR of the cell is measured by a 20C constant current discharge pulse with a duration of 100

ms. The discharge resistance is calculated by the resulting voltage drop after the load is applied. Due to the linearity of the pulse, the slope of the voltage can be extrapolated back to the beginning of the discharge pulse using a least square fit of the linear curve (Figure 4-6). Once the voltage drop is extrapolated, Equation 4-1 is then used to determine the discharge ESR [53][52].

$$ESR = |(V_{OC} - V_{LOAD})/I_{LOAD}| \quad (4\text{-}1)$$

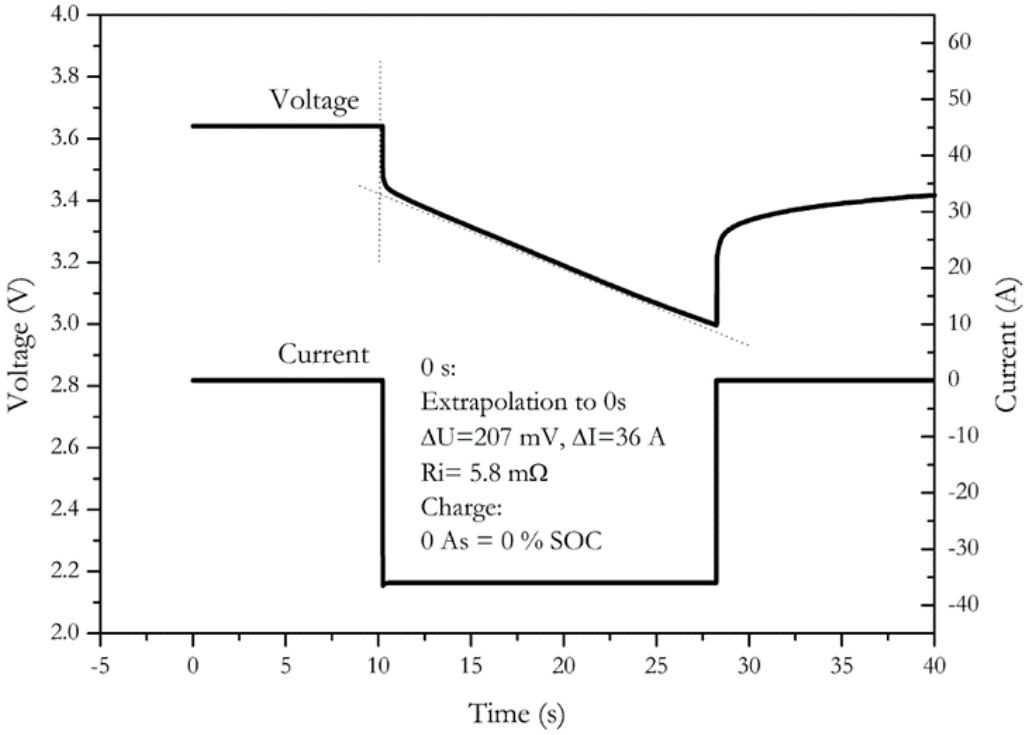

Figure 4-6 Reduction of feigned resistance introduced by discharge by extrapolation to the beginning of the discharge pulse [52].

Cell Capacity

A determination of the capacity of the cell under test is a particularly important analysis tool that is widely utilized in evaluating the aging of li-ion cells. If periodically applied, the test can evaluate the capacity of the cell and the resistance change of the cell as it ages. It can also be used for post-test analysis such as Differential Voltage Analysis and Incremental Capacity Analysis. While the cell capacity test can be conducted at various current rates, lower rates limit the resistive effects.

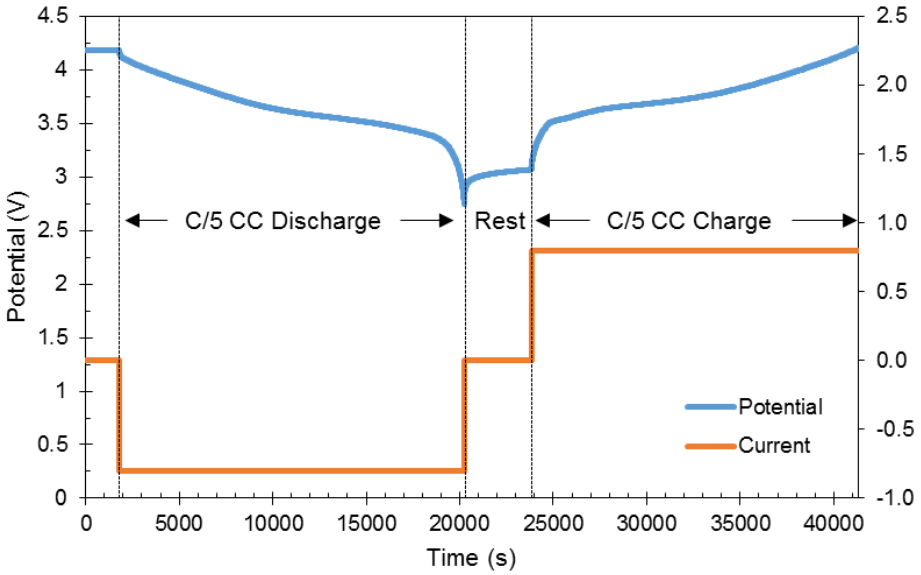

Figure 4-7 Representative C/5 cell capacity test of a $LiCoO_2$ cell.

For each capacity test, the cell was charged at C/5 Constant Current (CC) until the potential reached the max charge voltage and then the cell was charged at a Constant voltage (CV) until the current fell to C/40. The cell was allowed to rest for approximately one hour and then discharged at C/5 CC until the cell potential reached the minimum discharge voltage. The cell was then allowed to rest for another hour and then charged at C/5 CC to the max charge voltage followed by a CV charge to C/40.

Experimental Verification

In order to determine the effects of the experimental setup on the performance of the LIB, various tests were conducted to verify the impact of the setup as well as the puncture of the battery. These tests were aimed at evaluating and quantifying any changes in the battery's capacity, DC ESR, and EIS curve. These specific metrics were chosen due to their use as primary methods of monitoring and evaluating the aging of batteries over their lifecycle. Therefore, any alterations caused by the addition of the test chamber and the puncture of the battery needed to be quantified in order for them to be used for long term cycling and full lifecycle testing. A commercially available 2.6 Ah, $LiFePO_4$/Graphite, LFP-26650P LIB was utilized for these verification procedures.

Capacity Analysis

The initial testing focused on identifying any changes made to the usable capacity as a result of the transfer of the LIB into the test chamber. Discharge tests of the battery were conducted in order to measure this change. Figure 4-8 shows both a C/2 and 1C constant current discharge curves measured from the LIB both before and after the transfer and battery puncture. The plots of the battery potential vs. capacity demonstrate a minimal variation in the profiles measured for both the C/2 & 1C discharge respectively. The pre and post transfer capacity measurements made, show that the battery's capacity has changed less than 0.5% as a result of the transfer process. This small reduction in capacity is attributable to the fact that the discharge of the battery is limited by a minimum potential of 2.5 V. This threshold is affected by the additional conduction losses that the stainless steel end caps add to the system resulting in less capacity being extracted from the battery.

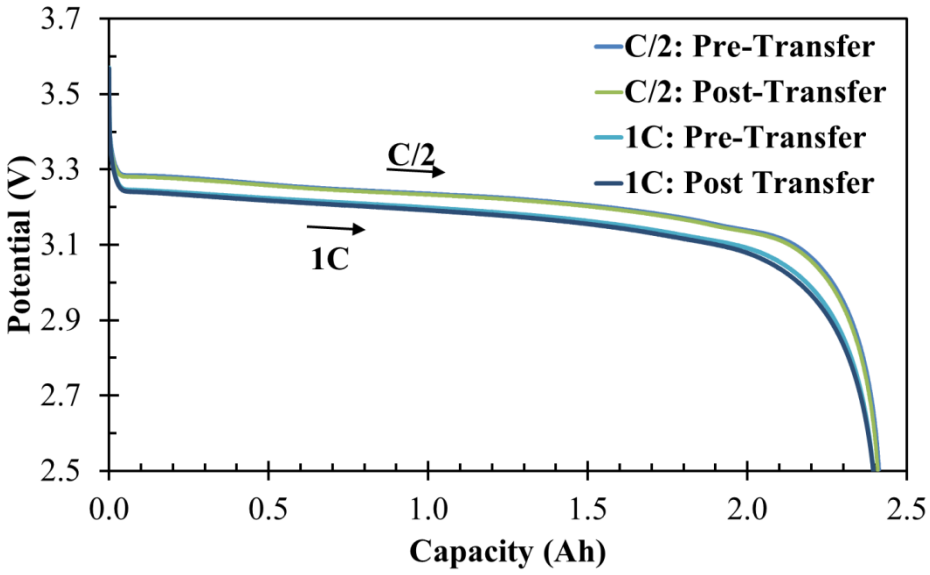

Figure 4-8 Evaluation discharge curves from 3.65 to 2.50 V at 1C and C/2 rates measured pre and post transfer at 298 K ambient.

DC ESR Analysis

The second test conducted focused on establishing the change in DC ESR that the stainless steel end caps add to the LIB. The advanced VDA method [52], uses a 100 ms discharge pulse to determine the DC ESR of the LIB by comparing the open circuit potential to the extrapolated load potential. This method was used to determine the resistance of the system before and after the transfer allowing for the additional resistance of the stainless steel conductors to be identified. Utilizing the advanced VDA method at 100% State of Charge (SOC) yields a pre-transfer DC ESR of 22.82 mΩ, and a post-transfer ESR of 24.26 mΩ resulting in a 1.44 mΩ test chamber DC ESR. This additional resistance is directly responsible for the additional potential drop and thus the slight reduction in capacity measured in the first verification tests shown in Figure 4-8.

EIS Analysis

EIS measurements were used as the final test aimed at assessing the effects of the test chamber on the LIB. A Metrohm PGSTAT 302N/FRA Potentiostat with a 20 A booster was used to apply a 10 mV amplitude potential with a frequency sweep from 5 kHz to 10 mHz. The same EIS measurements were made on the battery before and after the transfer, and are displayed in Figure 4-9. A distinct increase in the magnitude of the real resistance is identified in the comparison of the two data sets. Additionally, there is a slight phase shift at higher frequencies. Both of these results are expected due to the addition of the stainless steel end caps.

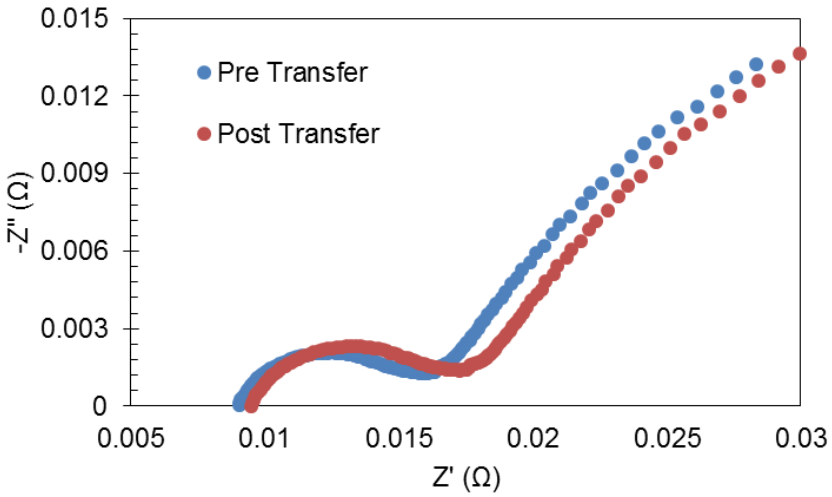

Figure 4-9 Nyquist plots of the LIB at 100% SOC, measured pre and post transfer.

The chamber verification tests were performed on a 2.6 Ah, $LiFePO_4$/Graphite, LFP-26650P cell. While minor variations were seen with each of the tests, they confirmed that the use of the test chamber would not adversely impact the overall performance of a cell place inside. They also established a baseline of the test setup for use in understanding the results of each study.

Chapter 5

Experimental Results

Single Cycle Internal Pressure Evolution

The intent of this study was to examined the micro behavior of the internal pressure evolution inside of a cell during a single 1C cycle and compare that behavior periodically throughout high-rate lifecycle testing. It is well understood that the volume of both the cathode and anode will change depending on the level of intercalated lithium, and the intent was to attempt to measure this change through chamber pressure and correlate the reduction in delta pressure change during the 1C baseline cycle throughout lifecycle testing. A high power 2.6 Ah $LiFePO_4$/Graphite cell was selected for this study and it was subjected to elevated charge and discharge cycling. The battery was charged at 3.5 C (9 A) CC to 3.65 V and then charged at CV until 0.1 A. The battery was allowed to rest for ten minutes and was then discharged at 11.5 C (30 A) CC until the potential reached 2.0 V. This was followed by another 10 minute rest, after which the cycle would begin again. All of the testing was conducted in a temperature controlled chamber and the ambient temperature was kept at 298 K. The battery was subjected to this cycling profile 10 to 13 times per day, and allowed to rest overnight in order for the system to reach electrochemical and thermal equilibrium. This cycling pattern was continued until the usable 1C discharge capacity was reduced to 80% of its original value.

Baseline performance tests were conducted post transfer (5 cycles), and at 100 cycle intervals throughout the lifecycle testing in order to measure the battery performance with respect to time. These baseline performance tests included DC ESR,

capacity, and EIS measurements. The constant current full discharge tests were conducted at 1 C to measure the amount of accessible capacity within the battery. The discharge tests were also used to evaluate the internal pressure change within the battery with respect to cycle number. EIS measurements were conducted at 100% SOC to assess the change in internal impedance as the battery was cycled.

Internal Pressure Analysis

When examining the change in internal pressure of the test chamber, the system can most easily be described by the ideal gas law. Because the experimental setup cannot specifically determine the in-situ change in the amount of gas (Δn) or the change in internal chamber volume (ΔV), the ideal gas law can be rewritten to describe the molar density or the ratio of the amount of gas produced inside the chamber to the change in internal chamber volume (Equation 5-1).

$$\rho = \Delta n/\Delta V_{chamber} = P_{chamber}/\left(R * T_{battery}\right) \quad (5\text{-}1)$$

This approach also enables a compensation for the variability of internal temperature and pressure and their subsequent effect on the system. Examining the system during a C/25 cycle of a fresh cell yields a reproducible change in the molar density that is reversible between the charge and discharge process. Figure 5-1 demonstrates this process plotting the battery potential versus the change in molar density during the C/25 CV cycle. This reversible process implies a change in the amount of gas in the chamber, a change in the internal chamber volume, or a combination of the two during a discharge, or vise-versa during a charge. The

reduction of electrolyte is considered to be the primary cause of gas generation within the battery. While there are multiple causes for electrolyte decomposition, it is a slow process and is principally driven by the development of the SEI layer at the electrode-electrolyte interface [1]. The rate and product of this side reaction will vary depending on the composition of the electrolyte, however this process is non-reversible [54].

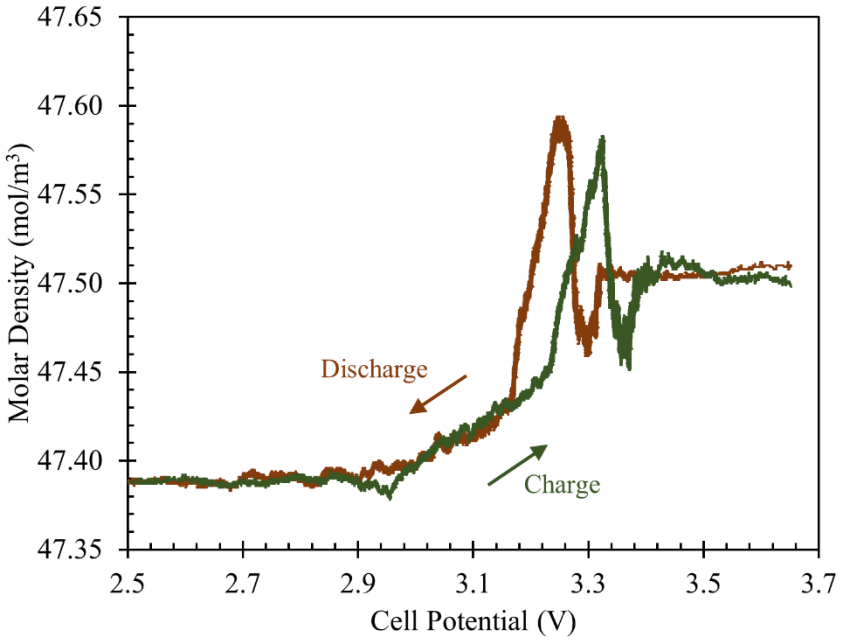

Figure 5-1 Recoverable molar density change during a single CV C/25 discharge and charge cycle from 3.65 V to 2.5 V.

If the change in the amount of gas inside the chamber is considered to be held constant, the pressure is then inversely proportional to the change in internal volume of the test chamber. The recoverable nature of this volume change during a complete charge/discharge cycle, appears to be linked to the lithium intercalation/de-intercalation process and thus to the battery electrode material. It is well known that both the positive $LiFePO_4$ cathode and negative hexagonal graphite anode experience volume expansion and contraction during this intercalation/de-intercalation process. Various

publications have experimentally and mathematically demonstrated that the $LiFePO_4$ cathode will experience a 4.2-6.8% volume change [55], [56], and the graphite anode a 7-14% volume change [57], [58]. In order to explore this idea, a fresh battery was disassembled and the volume of active material was estimated to be 10.02 mL for the cathode, and roughly 10.76 mL for the anode. When changes of both the cathode and anode are combined into a bulk measurement, it can be expected that the bulk electrode volume will be reduced by 0.02-0.98 mL during discharge. The experimentally measured increase in chamber volume of 0.128 mL from the beginning to the end of discharge falls in line with the predicted bulk electrode volume change.

Figure 5-2 shows the change in temperature versus potential, the change in pressure versus potential, and the change in pressure versus the change in temperature during a 1C discharge at 5, 200, and 500 cycles. While the ideal gas law cannot identify the contributions due to the change in temperature and volume, a trend in the data as the cell ages can be seen. The temperature change during discharge for the three cycles can be seen in the first row, and it can be noted that there is very little variation between the three. The pressure data indicates a non-ideal change in pressure with a lessening peak between 3.26 and 3.0 V that does not correlate to the consistent change in temperature. When plotting the pressure versus temperature, bottom row of Figure 5-2, the evolution of this pressure change can be seen more clearly with the peak reducing with cycle number. A comparison of Figure 5-1 and Figure 5-2 reveal that the peaks occur during the same potential range indicating that this non-ideal pressure change is likely related to the volume change during discharge.

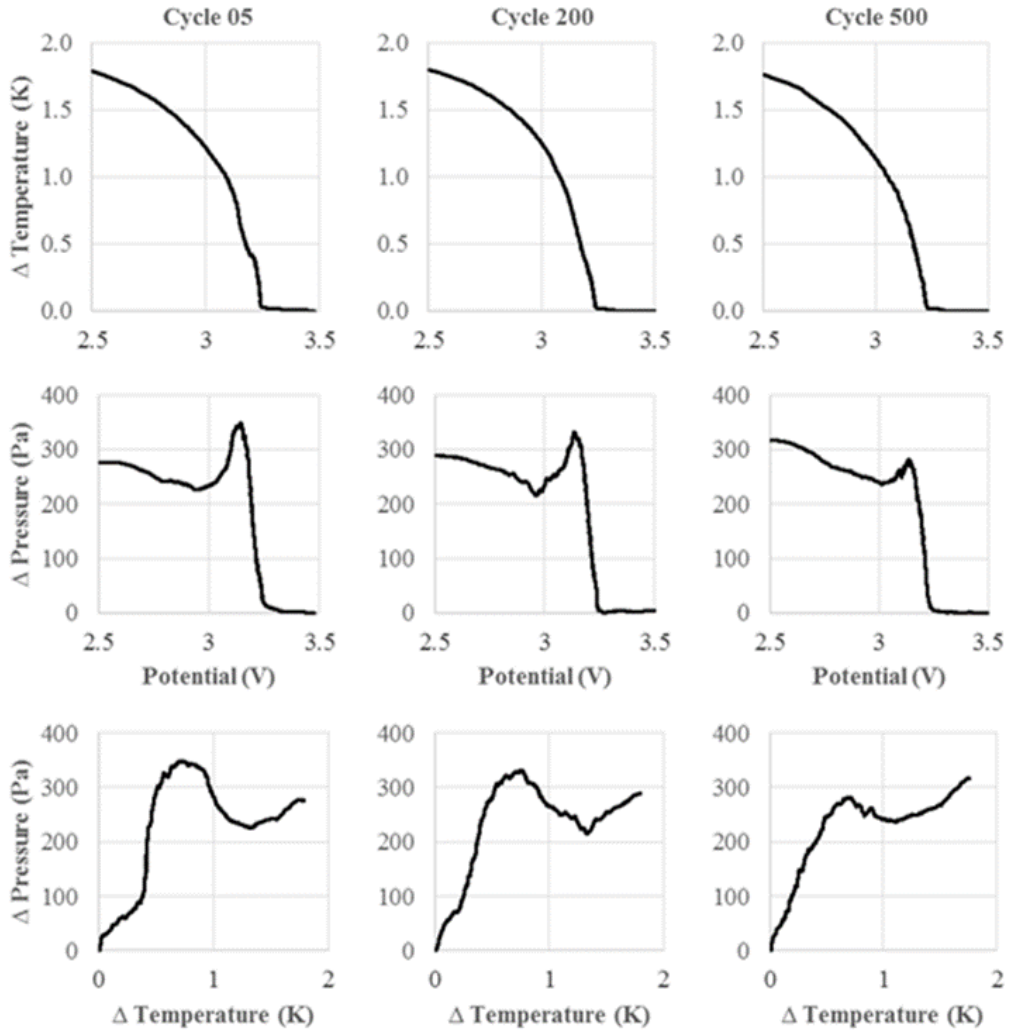

Figure 5-2 Change in measured temperature vs. potential (first row), pressure vs. potential (second row), and pressure vs. temperature (bottom row) during a 1C baseline discharge at 5, 200, and 500 cycles.

Statistical Correlation

An examination of the change in molar density during a 1C discharge measured throughout the cells life reveals an apparent connection to the fade in capacity. The molar density was measured under static conditions before and after the 1C discharge

and the delta was calculated. The relationship of the fade in 1C molar density delta versus the capacity fade across the lifecycle of the battery can be statistically examined using the Spearman's rank correlation coefficient (SRCC). The SRCC is used to assess the closeness of the relationship between the variables using the monotonic function [59]. Equation 5-2 describes the SRCC, for a sample size n, where the data (X_i, Y_i) is converted to a rank (x_i, y_i) and the rank difference is computed ($d_i = x_i - y_i$).

$$r_s = 1 - 6 \sum d_i^2 / n(n^2 - 1) \qquad (5\text{-}2)$$

A SRCC correlation was run to evaluate the relationship between the 1C molar density delta and the capacity, and it was found that there was a strong monotonic correlation between the values ($r_s = 0.7619$, $n = 8$, $d_f = 6$, $P < 0.05$). The statistically significant, strong monotonic relationship supports that there is an association between the change in molar density and capacity, however it does not confirm the direction of causation.

Differential Capacity

It is believed that this correlation relates to the electrodes ability to intercalate/de-intercalated lithium ions. Differential capacity represented by $Q_{diff} = dQ/dV$ or the derivative of the amount of charge removed from the battery during discharge with respect to the change in battery potential is used to understand phase transitions and to aid in understanding the intercalation/de-intercalation mechanism [60], [61]. Figure 5-3 demonstrates the 1C discharge differential capacity of the battery

at 5, 200 and 500 cycles. The peaks seen in the Figure 5-3 correspond to the potential plateaus of the constant current discharge curves of Figure 5-4a. The correlation of the lithium ion transport to the pressure data can be seen through an examination of Figure 5-3 with the peak transport occurring at 3.2 V and the bulk of the charge transfer occurring between 3.26 and 3.0 V. The rise in DC ESR over cycling and its effects on the reduction in capacity is evident in the reduction of charge transfer between 3.22 and 3.26 V.

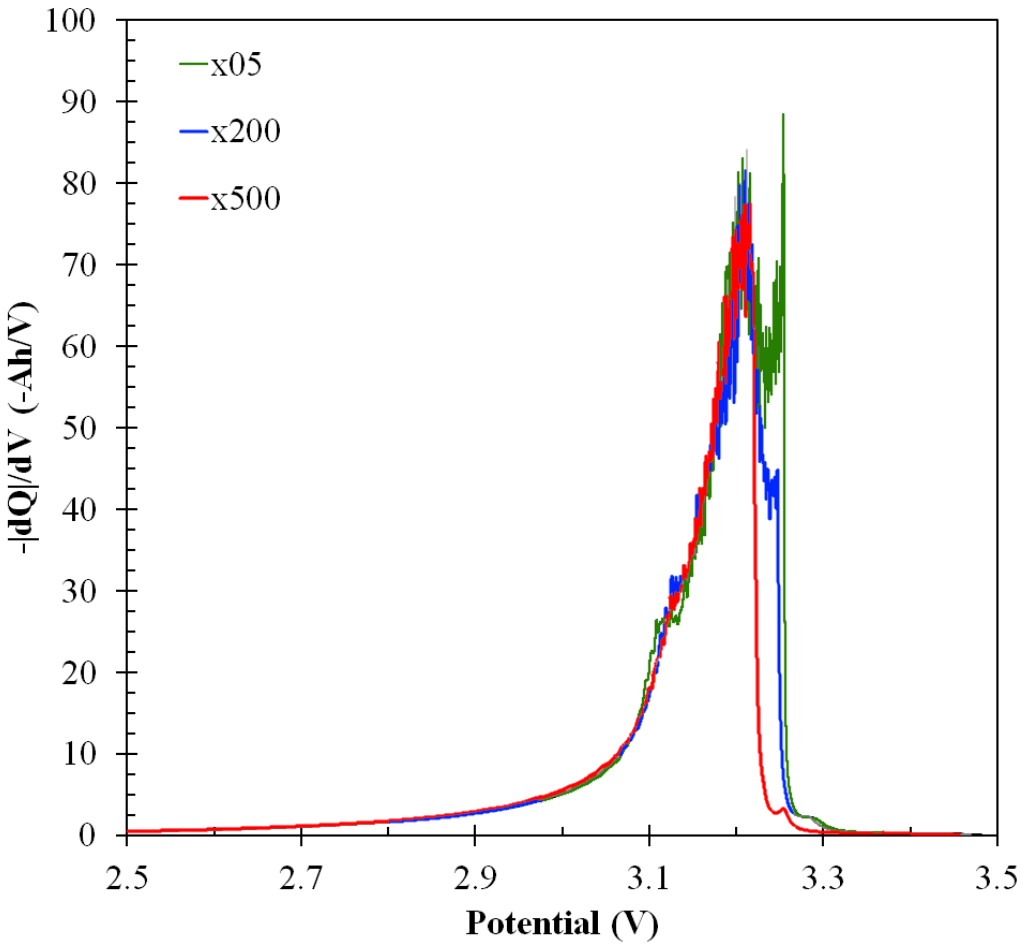

Figure 5-3 1C discharge differential capacity of the LiFePO4//Graphite LIB at 5, 200, and 500 cycles.

Capacity Fade

The evolution of the capacity fade and the DC ESR rise measured during the baseline performance tests are shown in Figure 5-4. The 1 C discharge capacity curves, seen in Figure 5-4a, demonstrate a decrease in capacity from 2.4 Ah to 1.9 Ah after 500 cycles of elevated charge and discharge rates. This reduction indicated end of life for the battery as it had reached 80% of its original capacity. The advanced VDA method [52] was used to determine the DC ESR of the battery at 100% SOC and Figure 5-4b illustrates this rise as a function of cycle number.

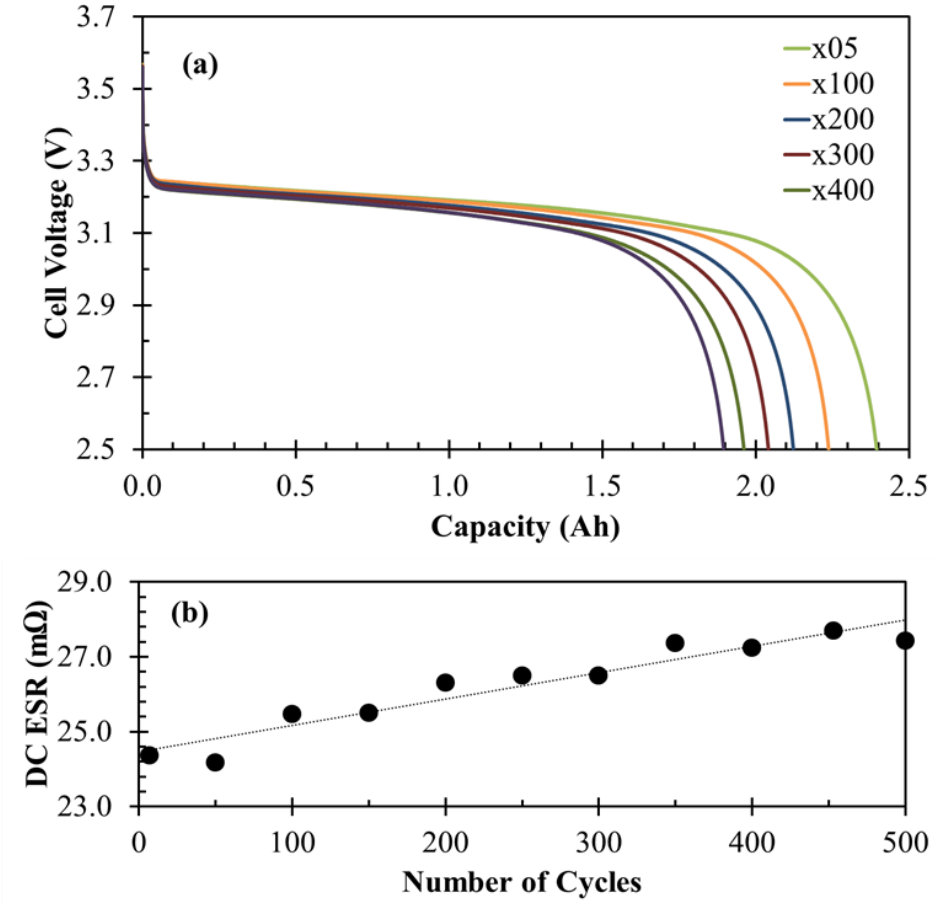

Figure 5-4 (a) Measured LIB potential vs. capacity, demonstrating capacity fade over battery life. (b) Calculated DC ESR climb vs. cycle number over the battery life.

Impedance Analysis

Periodic EIS measurements at 50% SOC of the battery across the 500 cycle life span are shown in Figure 5-5a. For clarity, only the EIS measurements for the 5th, 200th, and 500th cycle are displayed. Additionally, the Nyquist plots have been shifted to the zero point along the real axis in order to normalize the Ohmic resistance (Ro), or the high frequency intercept with the real axis (Z'). This shift allows the evolution of the Nyquist plots at the various cycles to be more easily compared. Figure 5-5b demonstrates the actual Ohmic resistance of the battery throughout the cycle life and thus the original position of the Nyquist plot along the real axis. This plot illustrates the linear nature of the real impedance shift as a function of cycle number. This shift may be attributable to an increase in electrolyte resistance, electronic resistance of active particles and with current collectors, as well as the contact resistance between the measurement instruments, the test chamber, and the battery [49].

With the exception of the Ohmic resistance growth, it is visually evident that the shape of the Nyquist plot did not change with any significance over the 500 cycles. This is supported by simulating this evolution with the modified Randles equivalent circuit shown in Figure 5-5a. The middle frequency arc is related to two processes occurring at the electrode-electrolyte interface, namely the charge-transfer resistance paralleled with the double-layer capacitance, and the SEI resistance coupled with the SEI capacitance. These two phenomena are represented within the model by the bulk R_w and C_{PE} elements because these two phenomena cannot be distinguished. The middle frequency arc width (R_w) had a negligible change between 5 and 200 cycles, and a small growth of 0.6 mΩ between 200 and 500 cycles. The 45° slope behavior at low frequency is indicative of the Warburg impedance corresponding to semi-infinite

diffusion. There is a small shift in the angle of the Warburg impedance between cycles 200 and 500, and may be a result of a change in the porous structure and particle size distribution on the diffusion related impedance in the active particle [49].

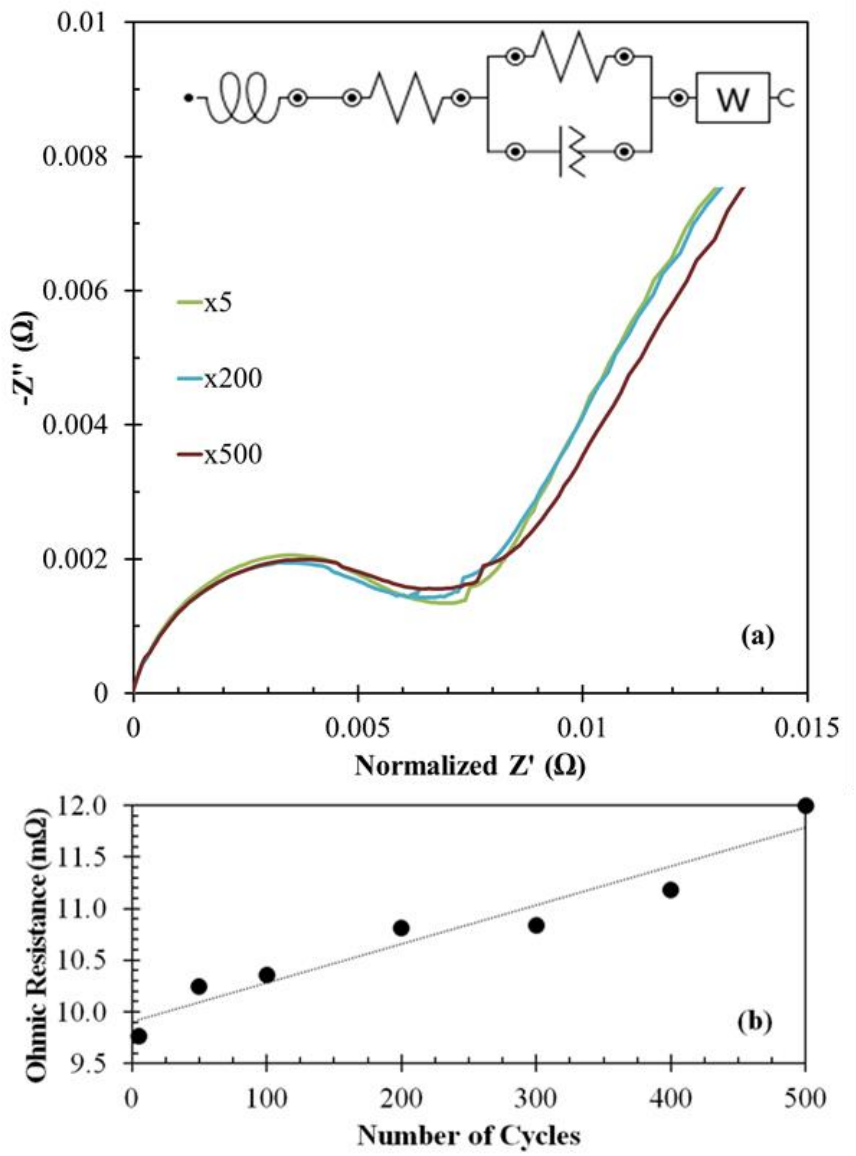

Figure 5-5 (a) Modified Randles equivalent circuit, and Nyquist plots at 50% SOC after 5, 200, and 500 cycles. (b) Linear rise of the Ohmic resistance measurements with respect to cycle number.

Conclusions

Lifecycle testing was performed on a 2.6 Ah, LiFePO4//Graphite, LFP-26650P LIB at elevated rates (3.5C Charge/11.5C Discharge) until the battery reached approximately 80% of its original capacity resulting in the completion of 500 cycles. Baseline tests were performed periodically to measure the change in capacity, DC ESR, EIS, and internal pressure as the battery aged. Capacity measurements and analysis confirmed the battery's accessible capacity faded as a result of the increase in DC ESR. EIS measurements and modeling analysis also established that the most significant material change within the battery during life cycling resulted from the rise in Ohmic resistance. Analysis of the battery's internal pressure evolution during the 1C baseline discharges yielded information elucidating apparent reversible electrode volume changes during the charge and discharge process. A strong SRCC correlation was established between the fade in 1C pressure delta and the capacity over the lifecycle of the battery. While it is well understood that the electrode volume changes during the intercalation / de-intercalation process, this bulk evaluation technique may be used to assess the performance of commercially packaged batteries and potentially as a predictive measure of battery aging. Differential capacity analysis was used to confirm the correlation of the behavior with the deintercalation process. The pressure data and analysis indicate a reduction in the amount of lithium de-intercalated during discharge as a result of the rise in the internal resistance and thus an apparent shift in the volume change over the lifecycle.

Over-Discharge Behavior of Various Lithium-Ion Batteries

Four commercial LIBs with different chemistries were selected for use in this study. The 26650 form factor cells were purchased from different manufacturers, and the LIB characteristics shown in Table 5-1 were obtained from the manufacturer's data sheet.

Table 5-1 Lithium-Ion battery manufacturer specifications.

	MFG. 1: $LiCoO_2/C_6$	**MFG 2: $LiFePO_4/C_6$**	**MFG 3: $LiMn_2O_4/C_6$**	**MFG 4: $LiNiMnCoO_2/C_6$**
Maximum Voltage (V)	4.2	3.65	4.2	4.2
Nominal Voltage (V)	3.6	3.2	3.8	3.65
Minimum Voltage (V)	2.75	2.5	3	2.75
Nominal Capacity (Ah)	4	2.6	3.5	3.6
Nominal Charge Current (A)	2	2.5	1.75	1.8
Max Charge (A)	4	5	1	3.6
Max Discharge (A)	6	42	7	18
Operating Temperature (°C)	0 ~ 50	-20 ~ 60	0 ~ 50	-20 ~ 60

XRD was used to confirm the makeup of the electrode materials. A fresh cell from each manufacturer was fully discharged and disassembled in order to analyze the electrode material. Samples were removed from both the cathode and anode, and the electrode samples were bathed in DMC for one hour to rinse the dried electrolyte from the surface of the electrode. The samples were then transferred to a dry box where they were allowed to remain for a minimum of two hours. The XRD results for the cathode materials can be seen in Figure 5-6 and the results for the anode materials

can be seen in Figure 5-7. The cathode materials were consistent with the manufactures description, and all of the anode materials were hexagonal carbon.

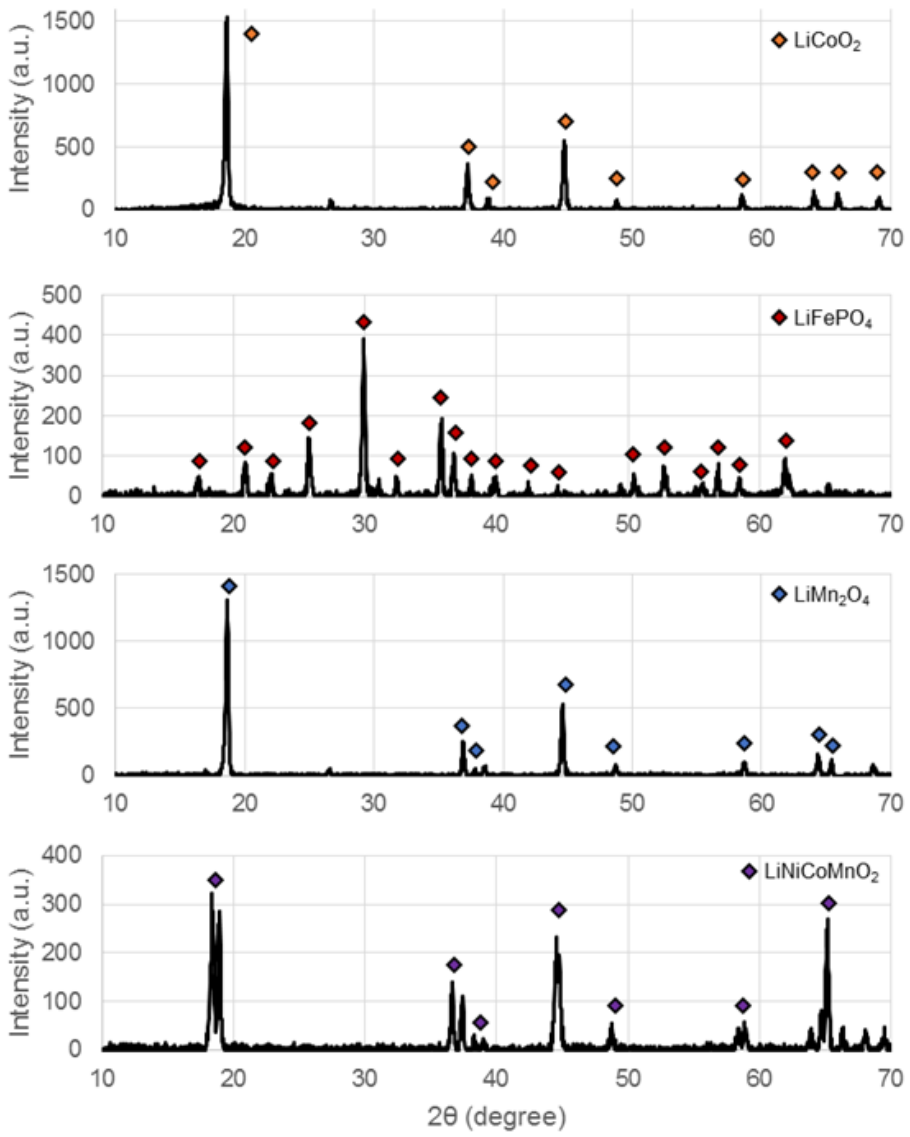

Figure 5-6 XRD analysis of the cathode material from each manufacturer: (a) MFG. 1: $LiCoO_2$, (b) MFG. 2: $LiFePo_4$, (c) MFG. 3: $LiMn_2O_4$, and (d) MFG. 4: $LiNiCoMnO_2$.

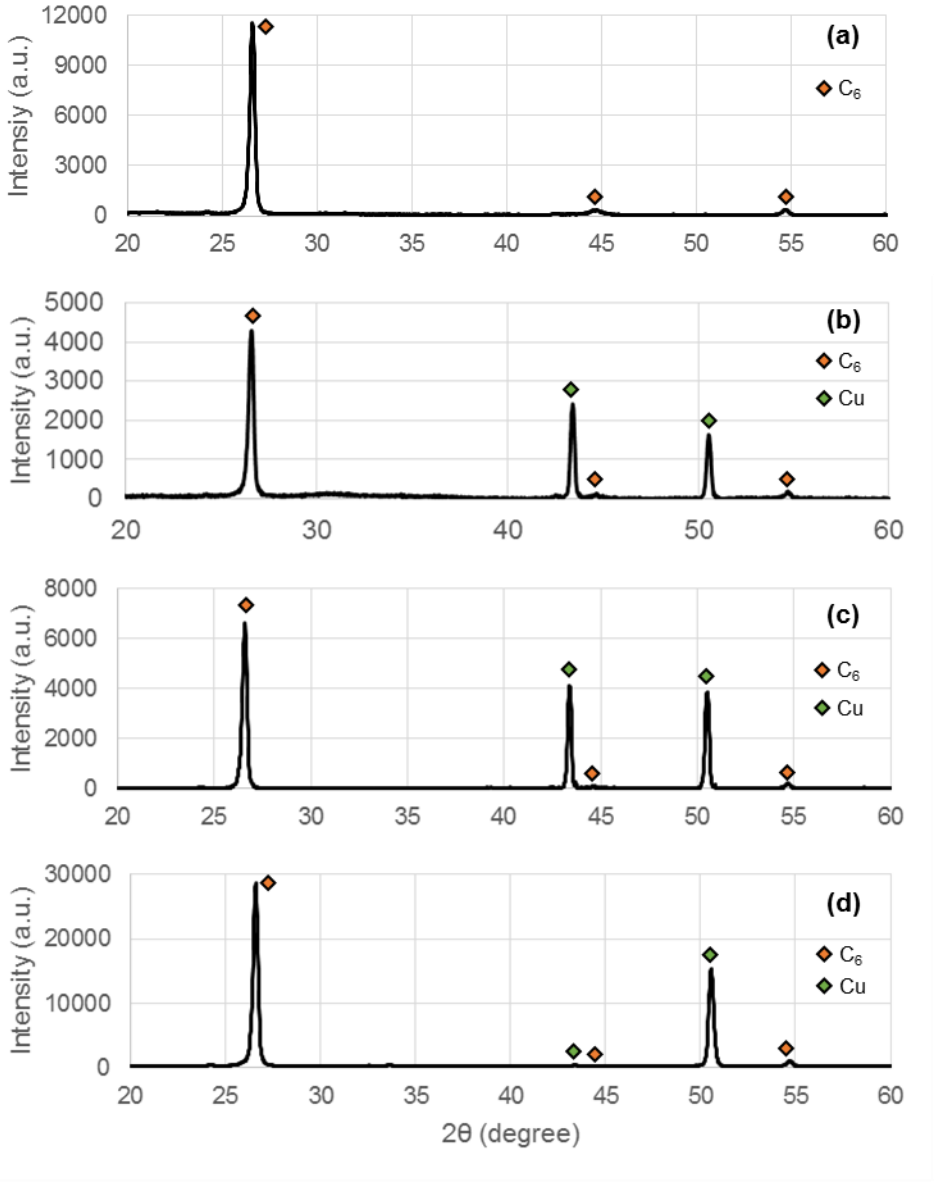

Figure 5-7 XRD analysis of anode material from each manufacturer. (a) MFG. 1: graphite, (b) MFG. 2: graphite, (c) MFG. 3: graphite, and (d) MFG. 4: graphite.

Baseline characterization tests including capacity, impedance, and resting pressure of the cell were performed after transfer into the test chamber and after the over-discharge procedure was complete. The capacity tests were performed using a CC discharge and a CC-CV charge procedure. With this procedure, the cell was

discharged at 1C to the minimum voltage followed by a 60 min rest and then charged at 1C to the maximum charge voltage and held until the current dropped to C/40. A Metrohm PGSTAT 302N potentiostat/ galvanostat with a Metrohm FRA32M frequency response analyzer was used to make EIS measurements after the cell was charged to 100% State of Charge (SOC) and allowed to rest for 1 hr. The impedance data was collected using a 10 mV amplitude potential with a frequency sweep over the range of 2 kHz to 15 mHz.

In this study, each cell was conditioned by cycling five times at a 1C rate using a CC discharge and CC-CV charge procedure. The cell was then charged CC-CV at C/5, allowed to rest for 60 minutes, and then discharged at C/5 to 0.0 V and held for 10 minutes. All cycling, baseline characterization, and over-discharge testing was conducted at 25 °C. The gases generated in the cell were analyzed at the conclusion of testing by gas chromatography. A 5 µl sample of gas was extracted directly from the test chamber into a gas-tight syringe through a septum. The surface morphology for the cathode and anode samples was characterized by a Hitachi S-3000N variable pressure SEM and a Hitachi S-5000H cold field emission scanning electron microscope (FESEM).

Over-Discharge Behavior

The cell potential, temperature and internal pressure were recorded during the over-discharge procedure of each cell. The potential of each cell follows the typical discharge curve for its respective chemistry with a sharp decline toward the end of the typical discharge range. Figure 5-8 through Figure 5-11 illustrates the end of the conventional discharge, the sharp discharge down to 0.0 V, the 10 min hold, and the

rebound time after the load is removed. During over-discharge all of the cells experienced a thermal rise beginning around 2.0 V and peaking when the cell potential reached 0.0 V. The cell with the $LiCoO_2$ cathode reached the highest temperature rise of 6 °C, followed by the $LiMn_2O_4$ with 4 °C, the $LiNiMnCoO_2$ with 3.5 °C, and finally the $LiFePo_4$ with 2.5 °C. The internal pressure rise began when the cell potential fell below 1.5 V indicating that the process likely began with the decomposition of the electrolyte at the lithiated anode surface by means of an ester exchange process [62].

The rate and magnitude of the pressure rise in each cell varied significantly between the four tested. Figure 5-12 through Figure 5-15 illustrates the pressure evolution within the cell during the entire C/5 discharge, over-discharge, and subsequent relaxation of the cell after the load was removed. Each cell shows a pressure decrease from the maximum voltage down to the manufacture's recommended minimum voltage which corresponds to the apparent bulk volume change during discharge as previously discussed. This is followed by steady pressure until the potential drops below 1.5 V, after which the pressure begins to rise due primarily to the production of gas within the cell but also due to the internal rise in temperature. After the potential rebounds, and the temperature stabilizes, the internal pressure differential can be analyzed with the following results: ΔPMFG 01=21 kPa, ΔPMFG 02=39 kPa. ΔPMFG 03=14 kPa, and ΔPMFG 04=6 kPa.

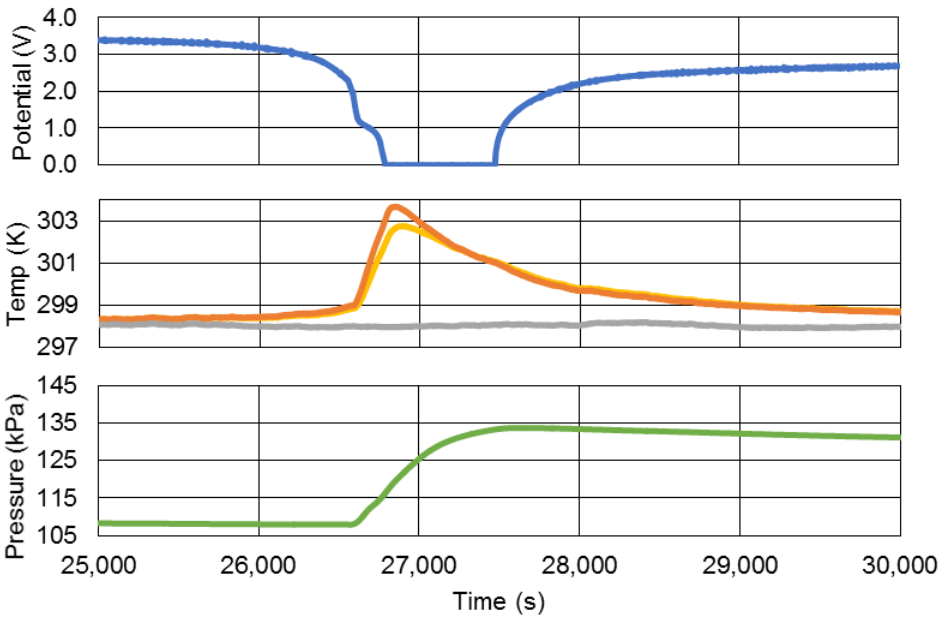

Figure 5-8 Over-discharge behavior potential, temperature, and internal pressure for MFG. 1: LiCoO2.

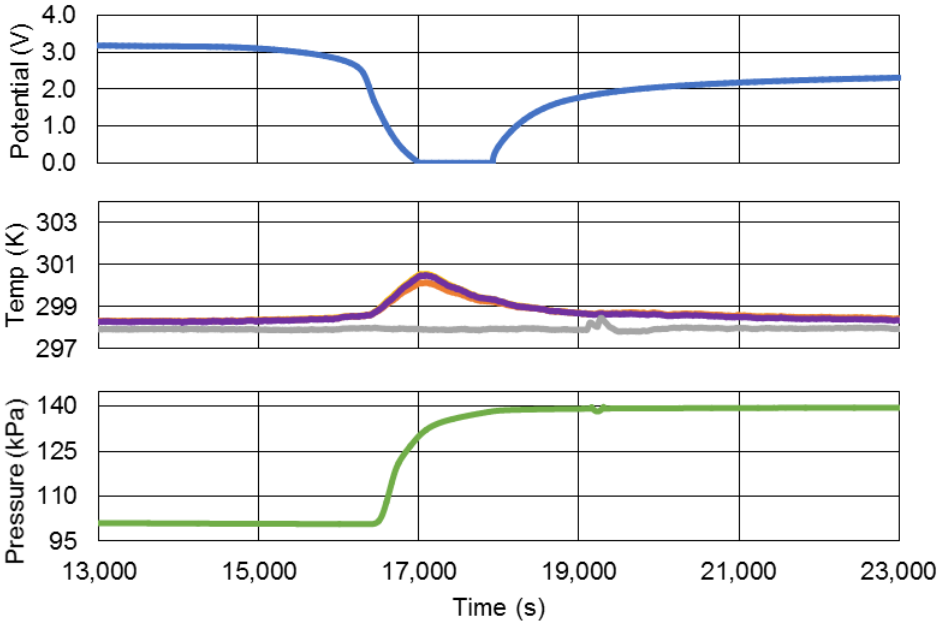

Figure 5-9 Over-discharge behavior potential, temperature, and internal pressure for MFG. 2: LiFePo4.

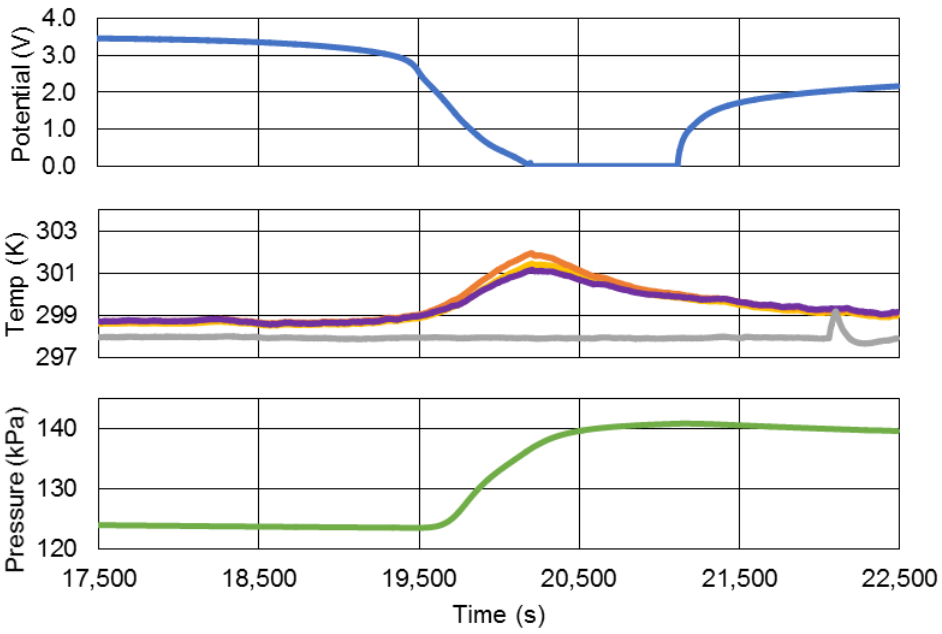

Figure 5-10 Over-discharge behavior potential, temperature, and internal pressure for MFG. 3: $LiMn_2O_4$.

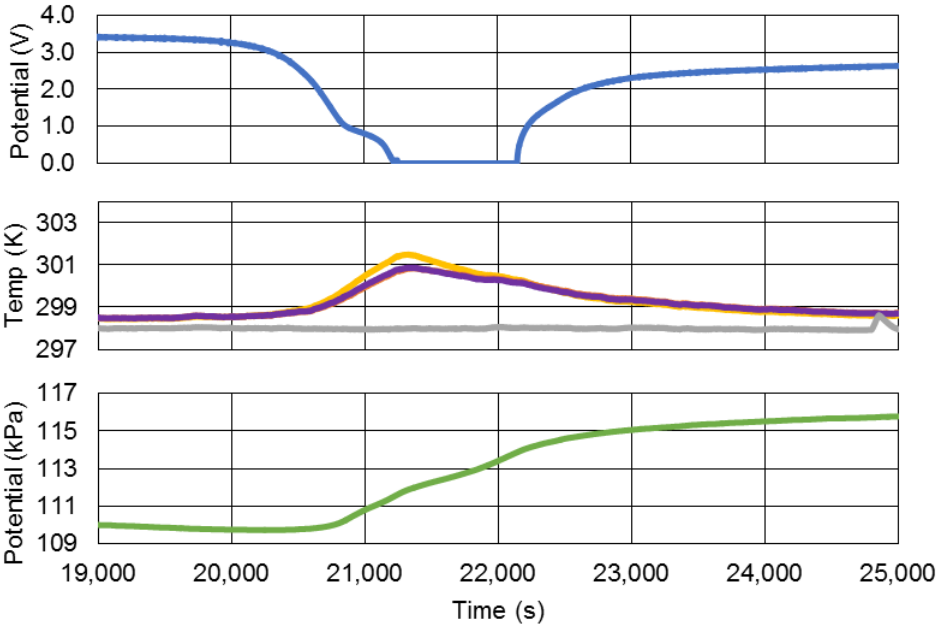

Figure 5-11 Over-discharge behavior potential, temperature, and internal pressure for MFG. 4: $LiNiCoMnO_2$.

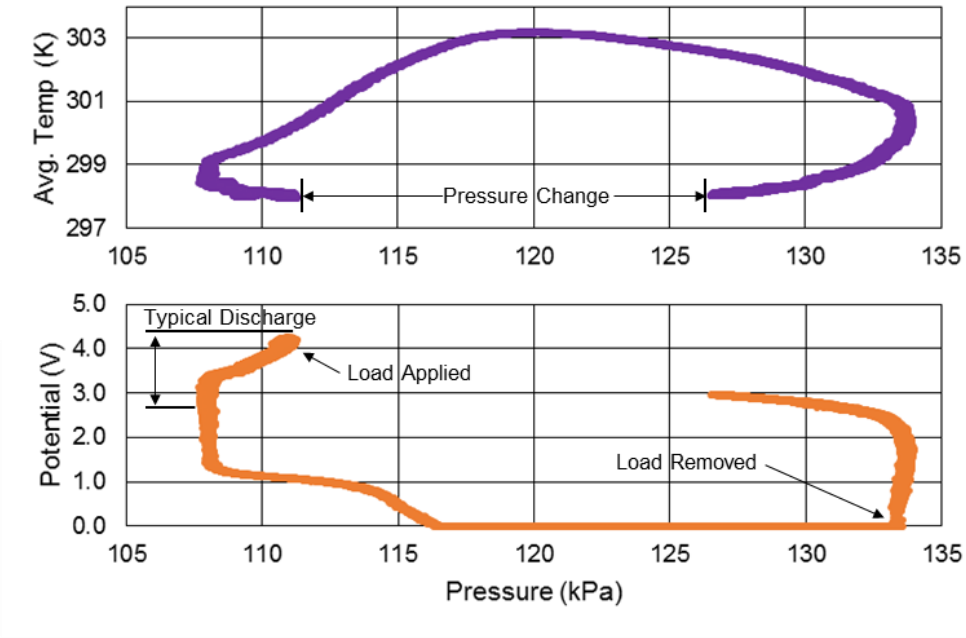

Figure 5-12 Over-discharge behavior including pressure vs. average temperature and pressure vs. potential for MFG. 1: $LiCoO_2$.

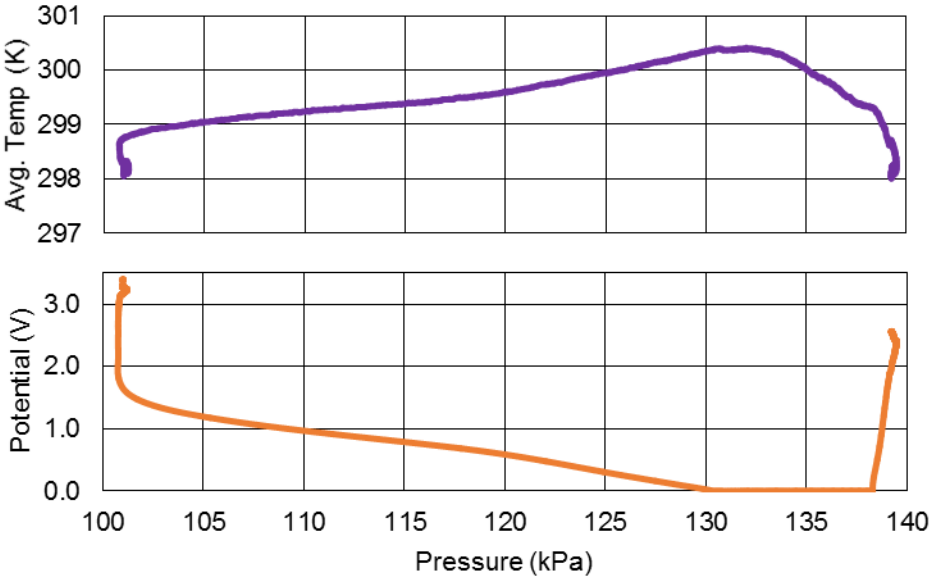

Figure 5-13 Over-discharge behavior including pressure vs. average temperature and pressure vs. potential for MFG. 2: $LiFePo_4$.

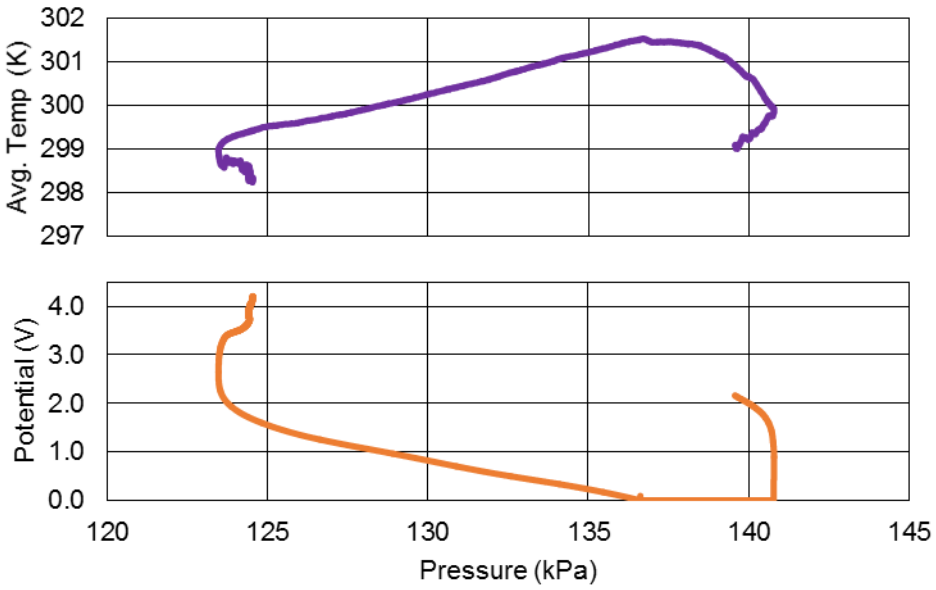

Figure 5-14 Over-discharge behavior including pressure vs. average temperature and pressure vs. potential for MFG. 3: $LiMn_2O_4$.

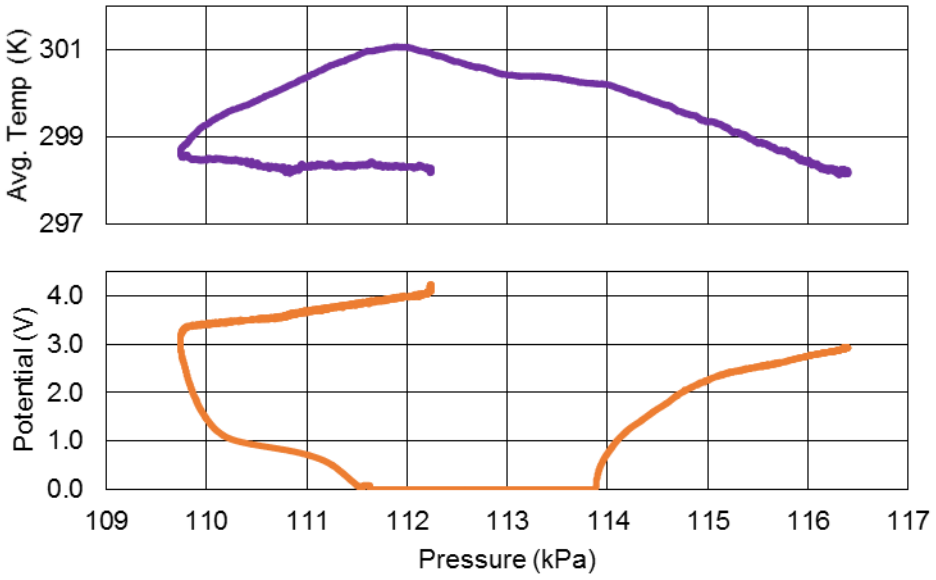

Figure 5-15 Over-discharge behavior including pressure vs. average temperature and pressure vs. potential for MFG. 4: $LiNiCoMnO_2$.

Gas Generation

GC-MS measurements of the gases generated inside of the test chamber were performed at the conclusion of over-discharge testing. The results of the analysis are displayed in Figure 5-16 through Figure 5-19, and the composition of the gas included CO, CO_2, CH_4, C_2H_4, and C_2H_6 as identified in the MS results. As previously mentioned, during over-discharge the relative high potential of the anode causes a dissolution of the copper current collector and the subsequent deposition on the cathode [63]. This accelerates the decomposition of the electrolyte resulting in a large volume of hydrocarbons being produced from the reduction. The gas generation reactions for DMC in the over-discharge conditions are as follows [5]:

$$CH_3OCO_2CH_3 + 2e^- + 2Li^+ \rightarrow 2CH_3OLi \downarrow + CO \uparrow \quad (5\text{-}3)$$

$$CH_30CO_2CH_3 + 2e^- + 2Li^+ + H_2 \rightarrow Li_2CO_3 \downarrow + 2CH_4 \quad (5\text{-}4)$$

$$CH_30CO_2CH_3 + e^- + Li^+ + 1/2\,H_2 \rightarrow CH_3OCO_2Li \downarrow + CH_4 \uparrow \quad (5\text{-}5)$$

Similar reactions could explain the case of DEC or EMC and suggests that the decomposition of the electrolyte takes place during over-discharge, releasing hydrocarbon gases [5]. Each of the cells demonstrated similar behavior in the types and relative intensities of the gases which is consistent with the decomposition of the electrolytes.

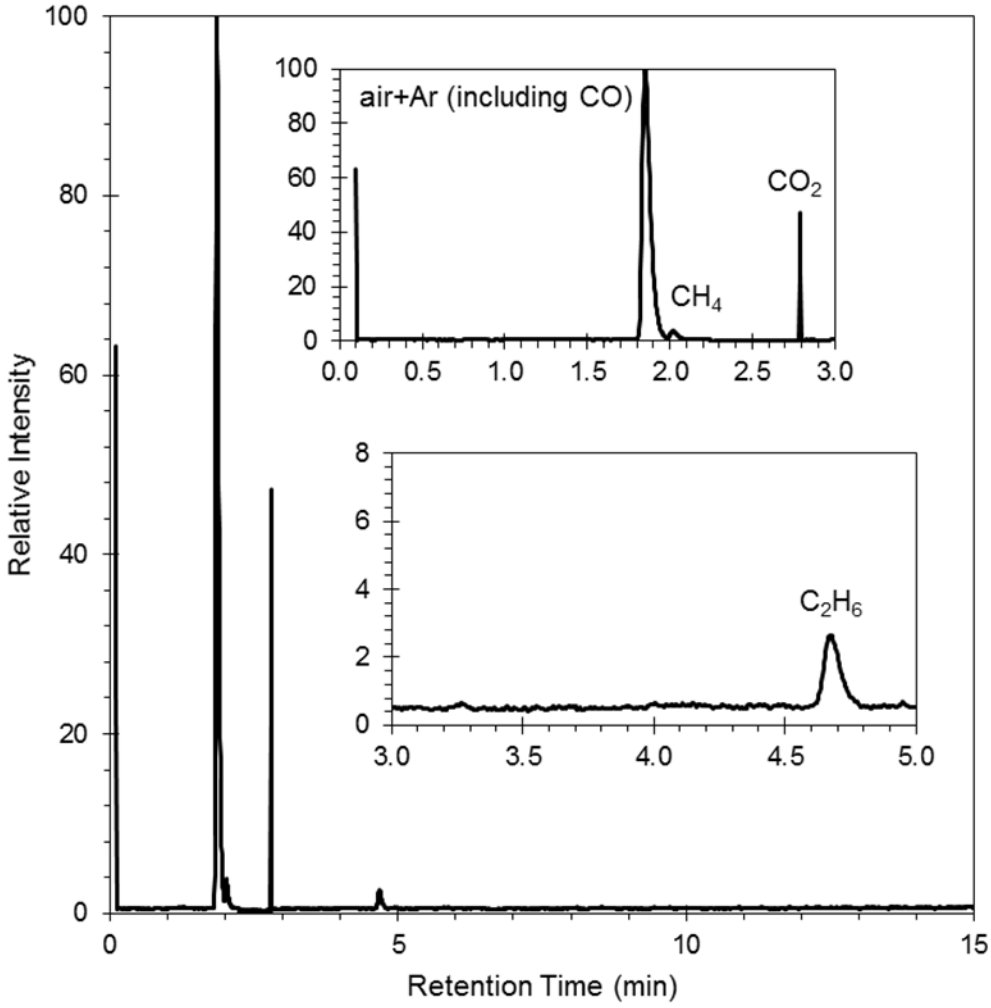

Figure 5-16 Gas-chromatography of the extracted gas at the conclusion of testing. Species marked in the figures are determined by corresponding mass-spectrometry results for MFG. 1: $LiCoO_2$.

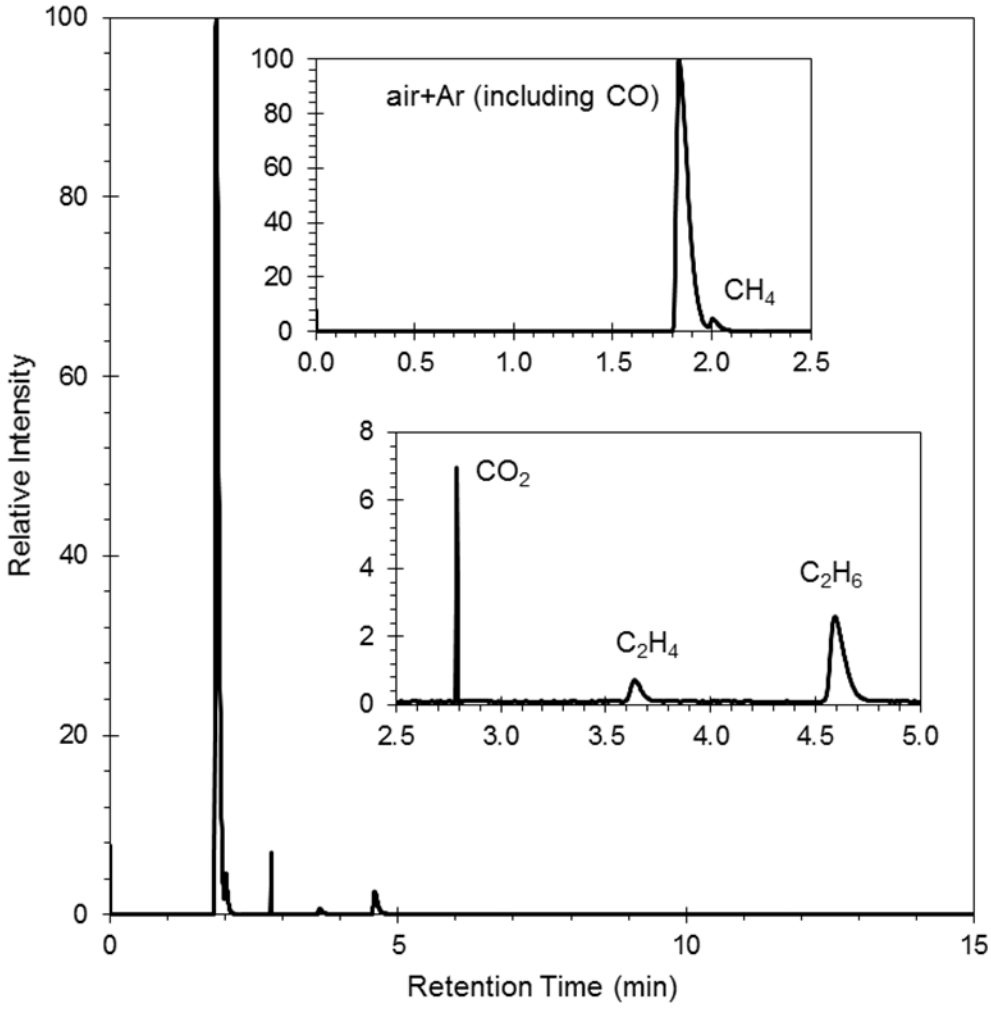

Figure 5-17 Gas-chromatography of the extracted gas at the conclusion of testing. Species marked in the figures are determined by corresponding mass-spectrometry results for MFG. 2: $LiFePo_4$.

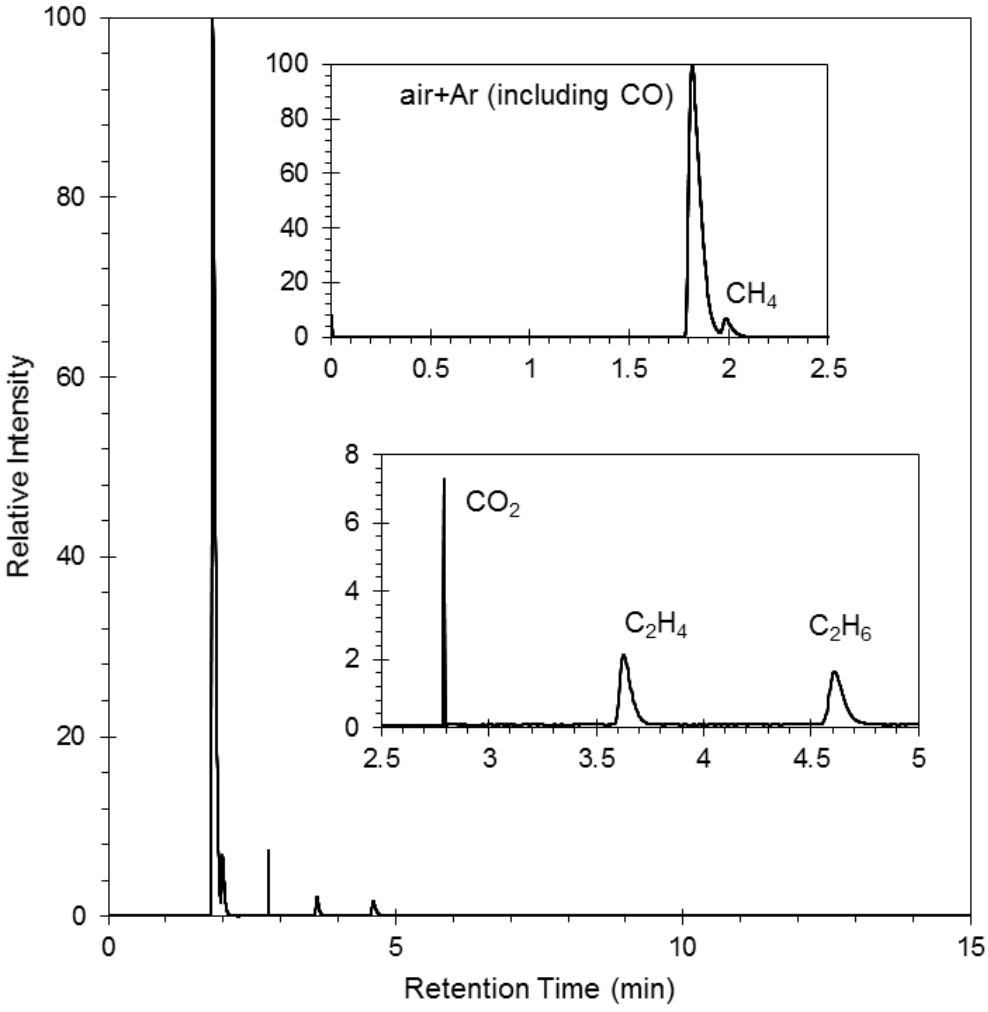

Figure 5-18 Gas-chromatography of the extracted gas at the conclusion of testing. Species marked in the figures are determined by corresponding mass-spectrometry results for MFG. 3: $LiMn_2O_4$.

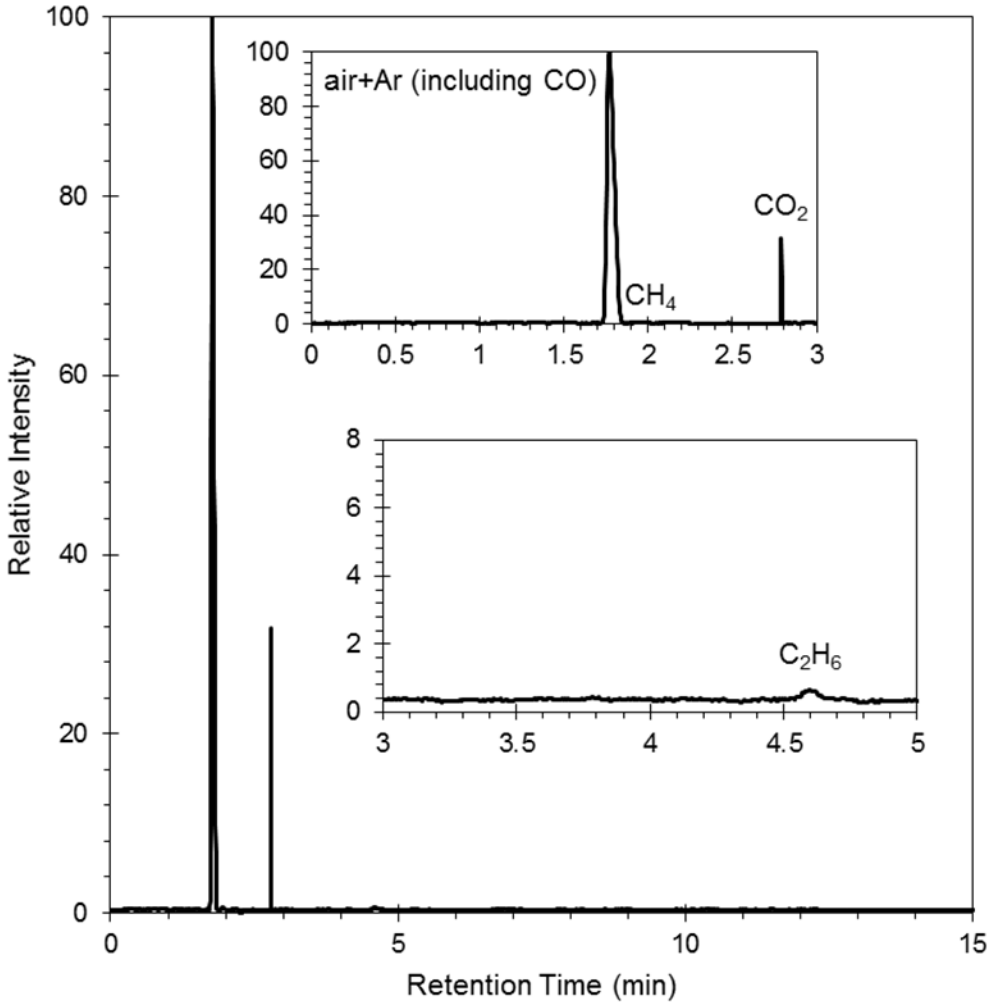

Figure 5-19 Gas-chromatography of the extracted gas at the conclusion of testing. Species marked in the figures are determined by corresponding mass-spectrometry results for MFG. 4: $LiNiCoMnO_2$.

SEM Analysis

The surface morphology for the cathode and anode samples were characterized by a Hitachi S-5000H cold FESEM. By dismantling the cell after cycling and GCMS testing, an image of the surface of the electrodes using FESEM can be

compared with the fresh state, non-cycled cells. If the side reactions occur, there should be some deposited byproduct on the platelets of the graphite anode. Figure 5-20 through Figure 5-22 show the anode (a-d) and cathode (e-h) in their post-test state where there is a clear contrast in the platelets of the hexagonal graphite and the individual grains of the various cathode materials. The signal from the microscope is not impeded by nonconductive impurities resulting in a very high resolution image. There is minimal evidence of large cracks formed in the non-cycled electrodes indicating that the process of dismantling the cell did not induce significant damage to the electrodes.

Multiple samples were examined on both sides of the cathode and anode at various points along the roll and, while there were minor variations, these images are representative throughout. Due to the fact that the samples were not bathed in DMC before imaging, there appears to be deposited $LiPF_6$ on the surfaces of all of the electrodes. In addition to the $LiPF_6$, there is clearly a deposited layer on the surface of the anode of MFG: 1 (Figure 5-20), which is considered to be a passivated surface layer [3], [64]. The previously discussed side reactions form this layer at areas of contact between electrolyte and bare carbon. The samples from the $LiMn_2O_4/C_6$ and the $LiNiCoMnO_2/C_6$ show minimal deposition on the surface of the electrodes which corresponds with the significantly lower ΔP during testing. While this experiment only over-discharged the cells once, repeated cycling after an over-discharge event demonstrates that additional gases are produced and a growth of the passivation layer is more prevalent on the surface of the anode [29].

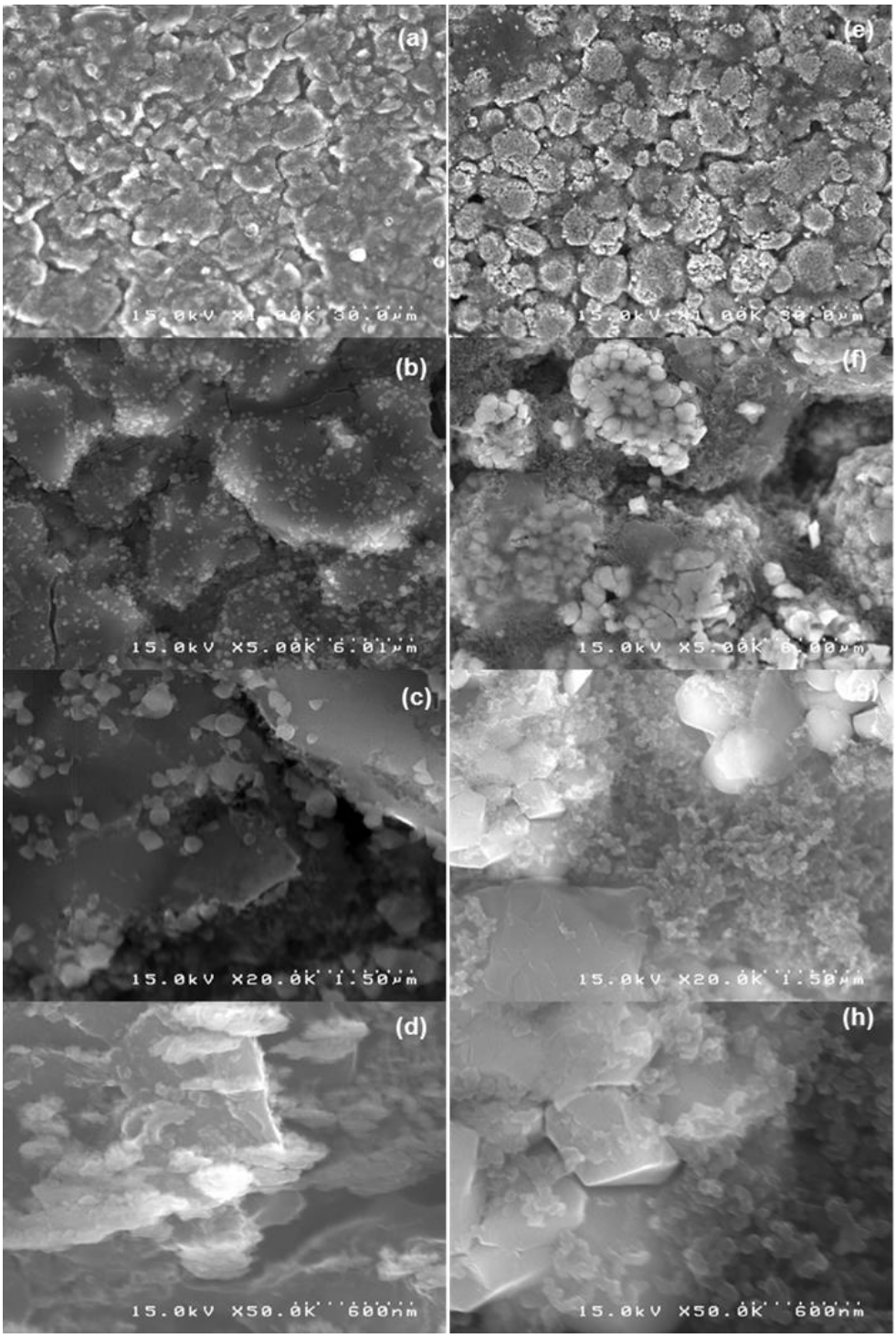

Figure 5-20 Increasing magnitude FESEM images of the post-test MFG01 graphite anode (a-d), and LiCoO2 cathode (e-h).

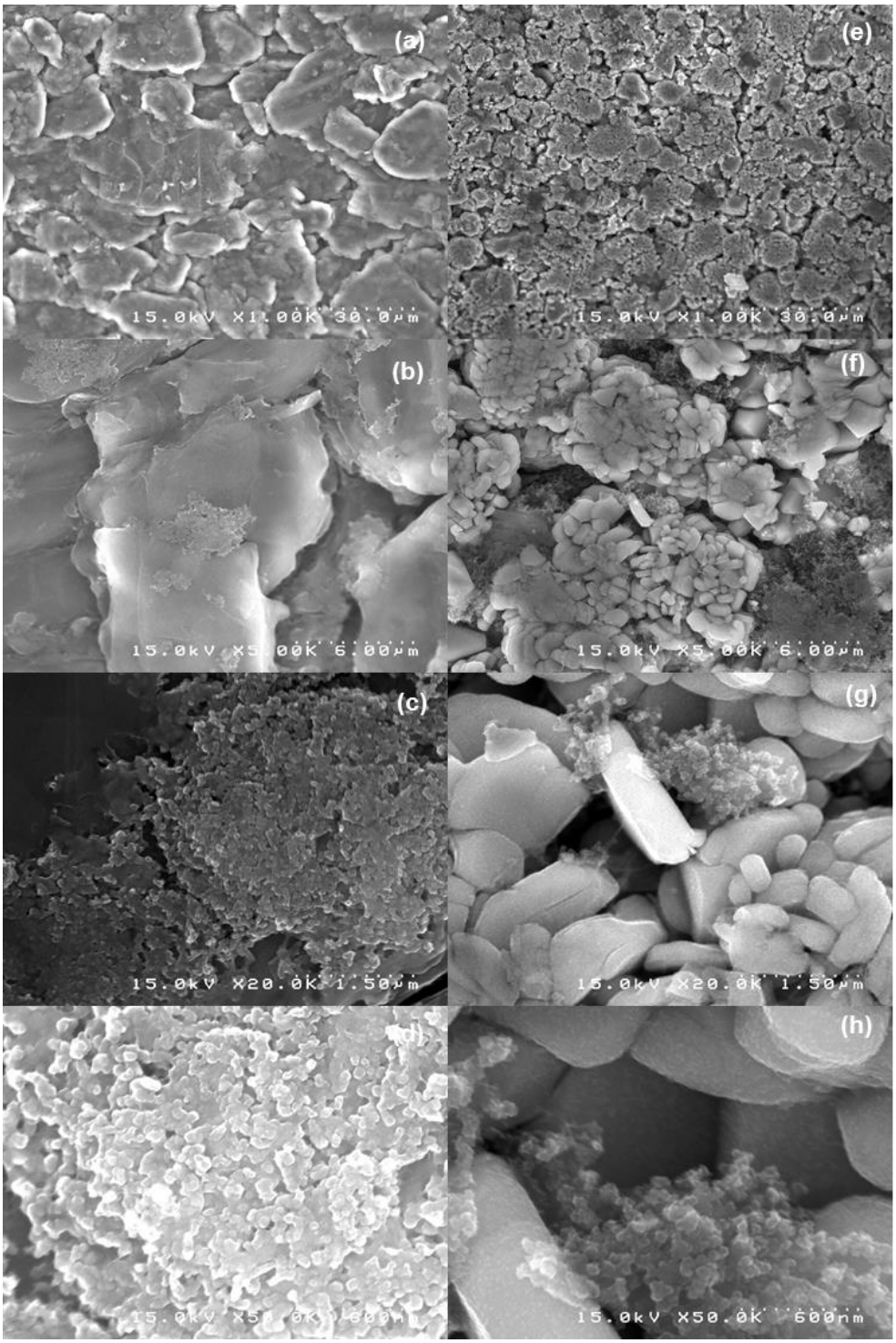

Figure 5-21 Increasing magnitude FESEM images of the post-test MFG03 graphite anode (a-d), and $LiMn_2O_4$ cathode (e-h).

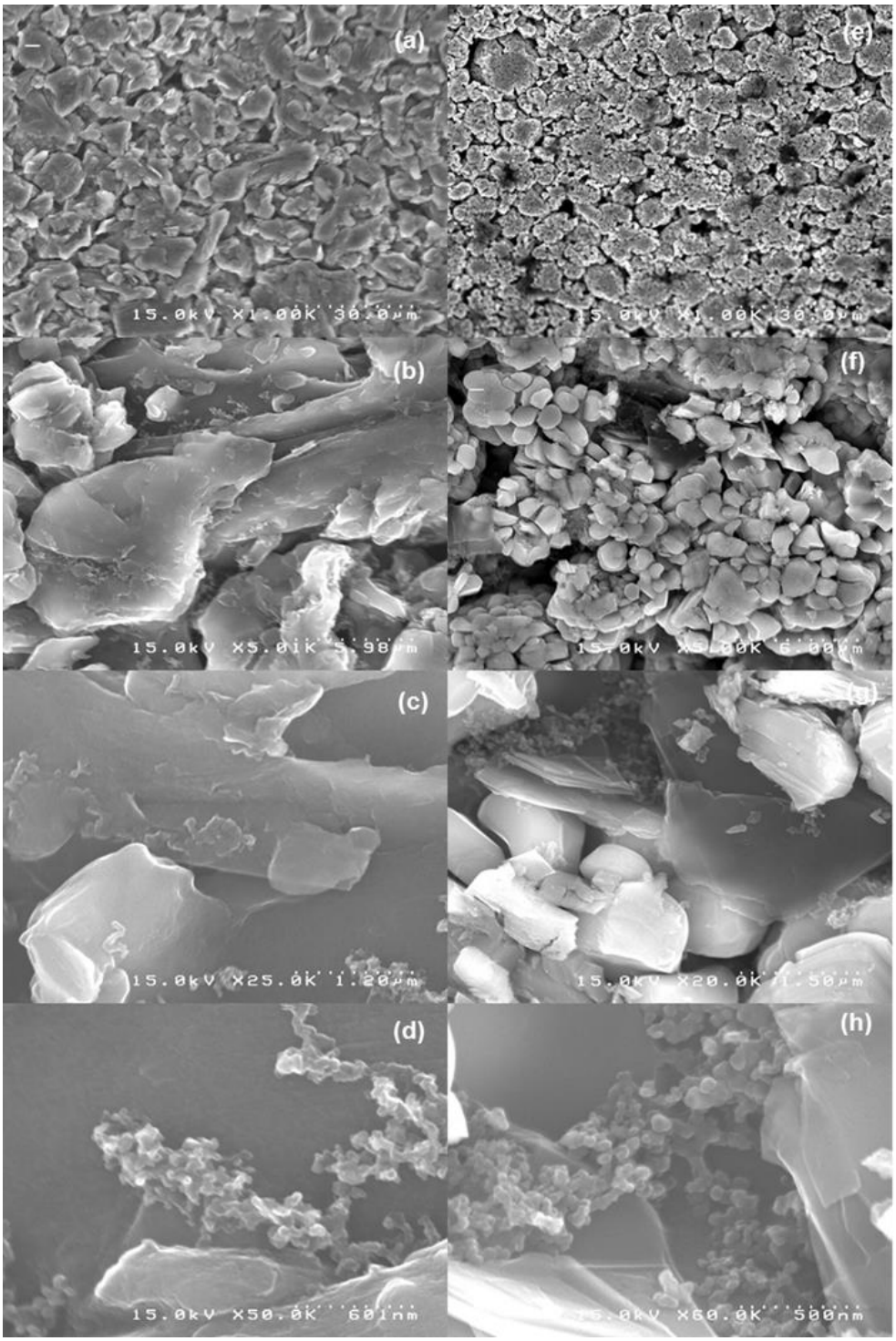

Figure 5-22 Increasing magnitude FESEM images of the post-test MFG04 graphite anode (a-d), and $LiNiCoMnO_2$ cathode (e-h).

Electrochemical Impedance

The EIS measurements and modeling results seen in Figure 4 19 through Figure 4 22 were conducted at 100% SOC and performed before and after the C/5 over-discharge test. This figure is representative of a typical EIS spectra for the various cells. The EIS curve begins with a semicircular arc at the middle frequencies followed by a sloped diffusion tail at the lower frequencies. The middle frequency arc is related to two processes occurring at the electrode-electrolyte interface, namely the SEI resistance (R_{SEI}) coupled with the SEI capacitance (C_{SEI}), and the charge-transfer resistance (R_{CT}) paralleled with the double-layer capacitance (C_{DL}) [51].

While it is evident that there is minimal change in the shape of the EIS spectra for each cell, the schematic in Figure 4-5 was used to model the response of the system before and after the over-discharge test in order to quantify any shift. Table 5-2 contains the modeling values of each cell before and after the test. With the exception of the Ohmic Resistance, or the high frequency intercept with the real axis, it can be seen that there is minimal change in the response of the cell. While irreversible damage has taken place within the cell, the only indication within the EIS data is that the Ohmic Resistance has increased. It has been shown that with repeated over-discharge cycling or continued cycling after an over-discharge event that the EIS curves will shift more rapidly [29], [32]. However, immediately after an over-discharge event there may not be any significant change in the diagnostic examination.

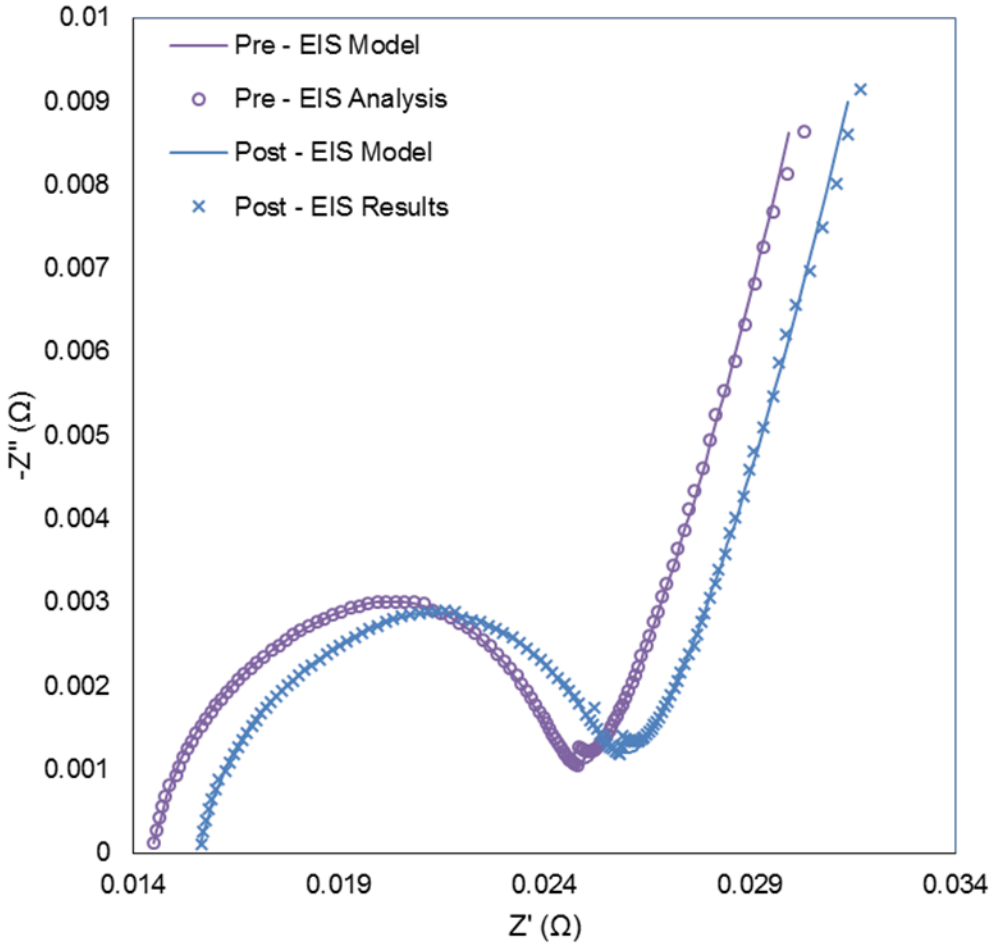

Figure 5-23 Nyquist plots of electrochemical impedance spectra measured at 100% SOC before and after over-discharge test for MFG. 1: $LiCoO_2$.

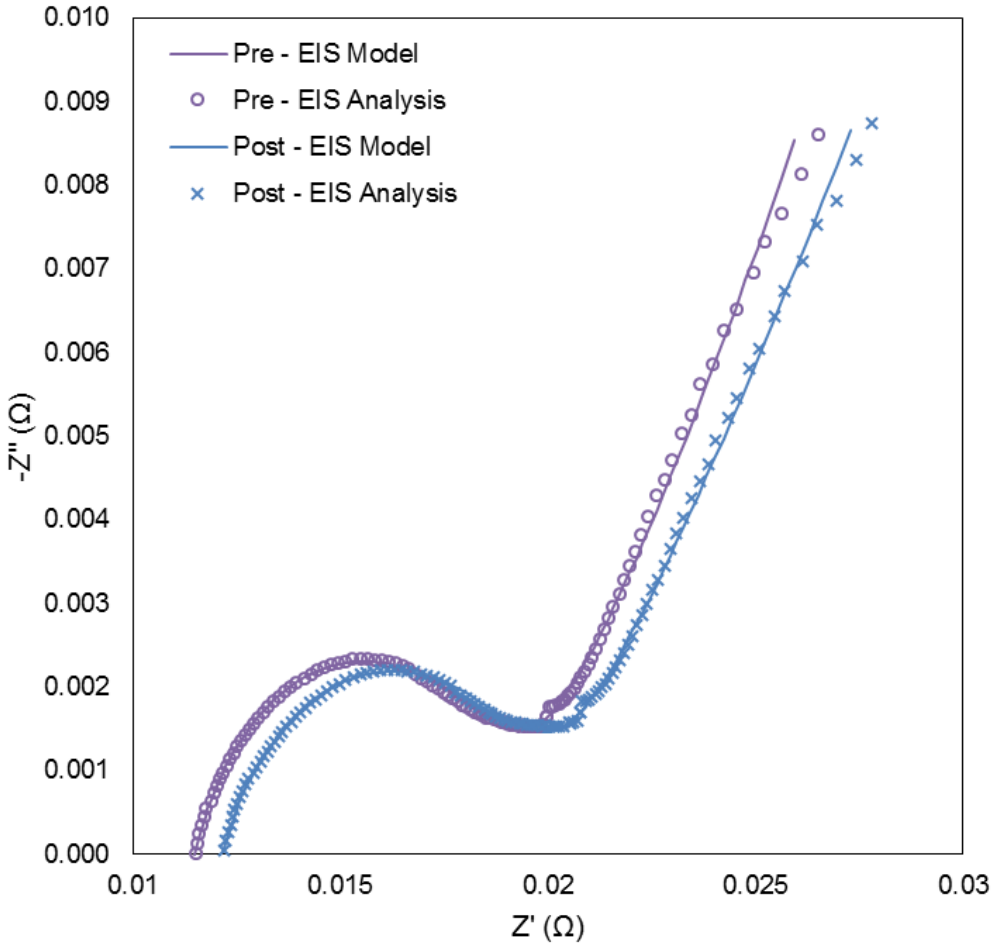

Figure 5-24 Nyquist plots of electrochemical impedance spectra measured at 100% SOC before and after over-discharge test for MFG. 2: $LiFePo_4$.

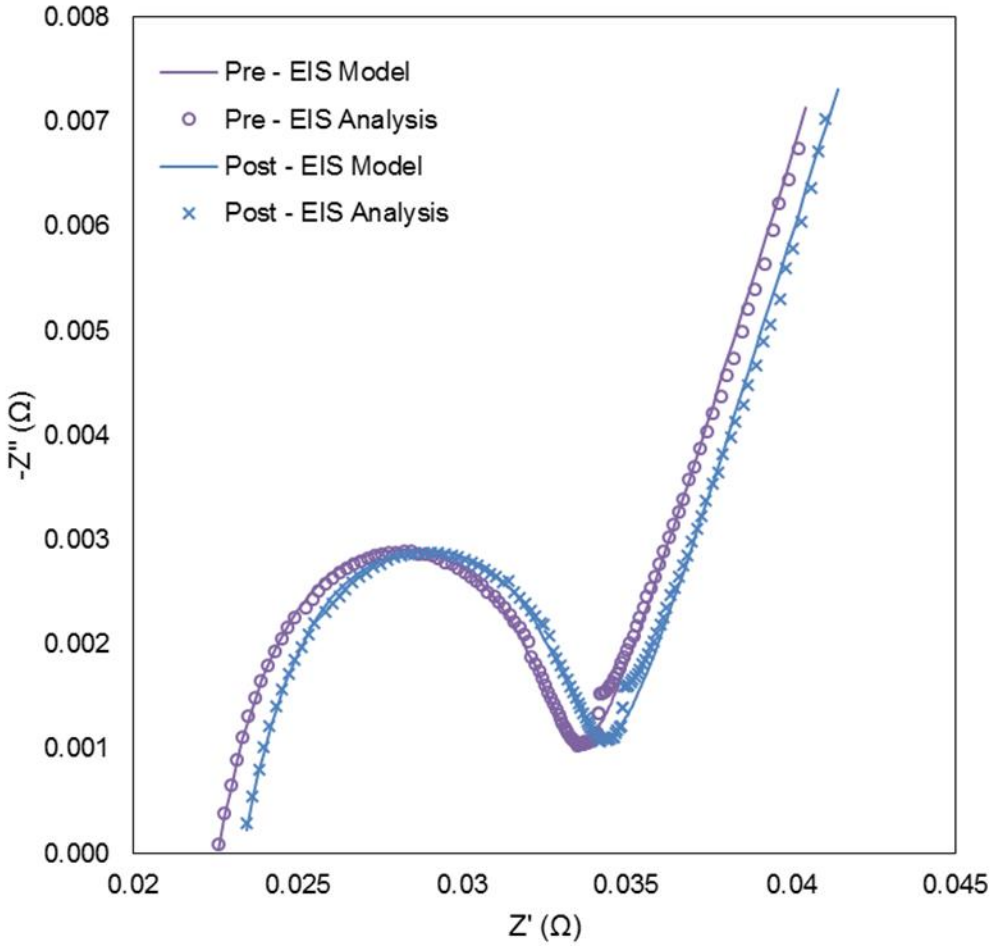

Figure 5-25 Nyquist plots of electrochemical impedance spectra measured at 100% SOC before and after over-discharge test for MFG. 3: $LiMn_2O_4$.

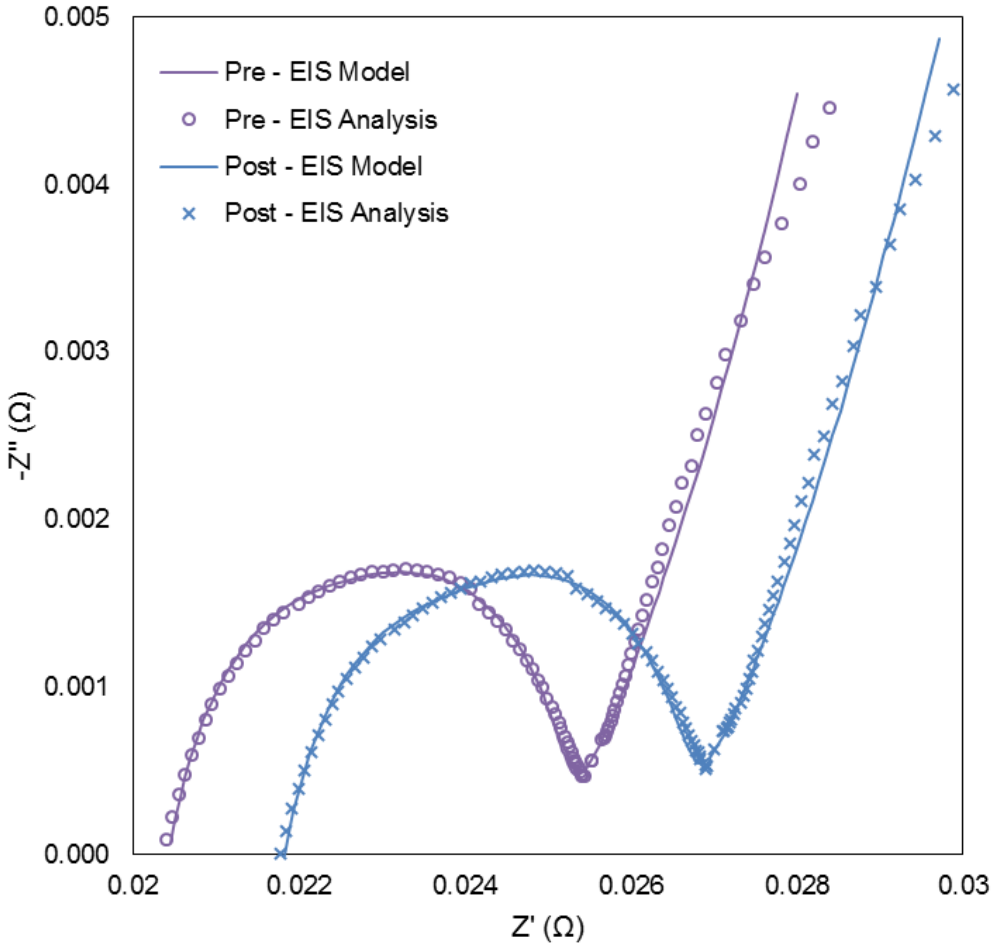

Figure 5-26 Nyquist plots of electrochemical impedance spectra measured at 100% SOC before and after over-discharge test for MFG. 4: $LiNiCoMnO_2$.

Table 5-2 Model fitting parameters for the impedance spectra of each cell pre and post over-discharge.

		R_S (mΩ)	R_{SEI} (mΩ)	C_{SEI}		R_{CT} (mΩ)	C_{PE}		W (Mho)
				Y0	N		Y0	N	
MFG 01: $LiCoO_2$	Pre	13.4	5.59	2.82	0.802	5.56	1.89	0.612	519
	Post	14.3	6.35	3.52	0.749	4.96	2.10	0.59	491
MFG 02: $LiFePO_4$	Pre	10.8	8.04	2.85	0.634	0.322	0.120	1.1	258
	Post	11.2	7.98	2.88	0.606	0.606	0.080	0.982	235
MFG 03: $LiMn_2O_4$	Pre	18.6	2.0	2.07	0.888	12.9	0.751	0.534	303
	Post	19.2	1.67	2.07	0.923	13.4	0.873	0.519	296
MFG 04: $LiNiMnCoO_2$	Pre	20.1	1.97	2.6	1.01	3.05	724	0.876	727
	Post	21.4	2.15	3.12	0.99	3.00	908	0.846	672

Conclusions

While the damage to the cell during over-discharge is well understood, this study examined the evolution of the gases produced during the over-discharge process and studied this gas production as a potential predictive measure of damage to the cell. Nondestructive measurements and characterization of the cell during testing included the cell potential, temperature, and EIS. While the cell potential indicates that the voltage dropped below the typical minimums for the cell, the behavior post over-discharge was indicative of typical cell operation and would be challenging to use as a diagnostic measure. The temperature rise of the cell during C/5 over-discharge was well within the typical range and would not be a useful measure of damage to the cell. Finally, the EIS characterization of the cell pre and post over-discharge showed

minimal change other than the rise in the Ohmic resistance. These nondestructive diagnostic measurements proved to be insufficient in predicting damage to the cell during an over-discharge event.

Additional destructive testing of the cell using GCMS and FESEM was performed, and confirmed that CO, CO_2, CH_4, C_2H_4, and C_2H_6 gases were produced and likely deposited on the electrode surfaces of the cells. While these tests are useful for post-mortem damage assessment, they are not practical for use as a predicative measure for cell damage during operation. However, measuring the internal pressure of the cell does indicate that a non-normal event has occurred to the cell due to the step change in pressure. This change in pressure is indicative of damage to the cell and could be used as a predictive measure in advance of a significant loss in capacity or complete cell failure.

Correlation of Internal Pressure Rise and Capacity Degradation

4 amp-hour (Ah) capacity commercial cells, manufactured in the cylindrical 26650 configuration and purchased from the Tenergy Corporation was used as test samples in this study. According to the manufacture data sheet, the operating voltage range is from 2.75 to 4.2 V, the temperature range is from 0 to 50 °C, and the maximum continuous cycle rate is 4 A charge and 6 A discharge. XRD confirmed that the electrode material consisted of a hexagonal carbon anode and a $LiCoO_2$ cathode. All cycling and baseline characterization testing was conducted at 25 °C in a custom designed constant-temperature environmental test chamber.

Baseline characterization tests including capacity, impedance, and resting pressure of the cell were performed after transfer into the test chamber and at

subsequent 25 cycle intervals. The capacity tests were performed using a CC discharge and a CC-CV charge procedure. With this procedure, the cell was discharged at C/5 (0.8 A) to 2.8 V followed by a 60 min rest and then charged at C/5 to 4.2 V and held at 4.2 V until the current dropped to C/40 (0.1 A). A Metrohm PGSTAT 302N potentiostat/ galvanostat with a Metrohm FRA32M frequency response analyzer was used to make EIS measurements after the cell was charged to 100% State of Charge (SOC) and allowed to rest for 1 hr. The impedance data was collected using a 10 mV amplitude potential with a frequency sweep over the range of 2 kHz to 15 mHz.

In this study, the cells were cycled at elevated rates, using a CC discharge and CC-CV charge procedure. Multiple cells were studied under different cycling profiles and their cycling characteristics can be seen in Table 5 1. Each cell was discharged at its respective max discharge rate until the potential reached 2.5 V followed by a 10 min rest and then charged at its max charge rate until the potential reached 4.2 V and held at 4.2 V until the current dropped to C/40. This was followed by another 10 min rest and then the cycle would begin again. At 25 cycle intervals, the cell was allowed to rest between 6-12 hr and then a baseline characterization was performed. This was followed by an additional 6-12 hr rest period and then the next 25 cycle interval would begin. The cells were cycled until the 1C capacity reached approximately 60% of the manufacturer value.

Table 5-3 Study cycling characteristics.

	Cell 01	Cell 02	Cell 03
Max Potential	4.2 V	4.2 V	4.2 V
Min Potential	2.5 V	2.5 V	2.5 V
Max Charge Rate	4 A / 1C	8 A / 2C	8 A / 2C
Max Discharge Rate	8 A / 2C	4 A / 1C	8 A / 2C

The gases generated in the cell were analyzed at the conclusion of cycling by gas chromatography. A Shimadzu GC-2010 Plus series GC equipped with a MS-QP 2010 Ultra mass detector was used. A bonded polystyrene-divinylbenzene column (J&W HP-PLOT Q) supplied by Agilent was used for GC separation, with helium as the carrier gas at a constant flow of 1.5 mL/min. The gas from each cell was extracted directly from the test chambers into a gas-tight syringe through a septum. Cell 03 utilized a 5 µl sample, while Cell 01 and Cell 02 utilized a 50 µl sample. The surface morphology for the cathode and anode samples from each cell was characterized by a Hitachi S-3000N variable pressure SEM and a Hitachi S-5000H cold FESEM. The samples were prepared by bathing in DMC for one hour and then placed in a dry box and allowed to dry for 2-5 hr before examination in the SEM.

Internal Pressure Rise

A snap shot of the internal pressure was recorded at the beginning of each baseline procedure, and Figure 5-27 through Figure 5-29 illustrates this pressure as a function of cycle number (N) for each cell. There appears to be three distinct regions within the pressure evolution. Cell 01 experiences a linear pressure rise of 0.205

kPa/cycle over the first 150 cycles, and the rate begins to slow and transition into the third region. The third region begins at about 275 cycles and continues through the end of cycling at significantly lower rate of pressure rise (0.037029 kPa/cycle) compared to the first region. Cell 02 experiences a comparatively high rate of pressure rise that begins with an average 4.027 kPa rise over the first 25 cycles, and a 10.899 kPa average over the remaining cycles. The first region of Cell 03, from 0-50 cycles, experiences a linear pressure rise of 0.567 kPa/cycle. The third region begins at cycle 150 and continues through the final 100 cycles. Again, this linear region has a significantly lower rate of pressure rise (0.0198 kPa/cycle) compared to the first region. This shift in behavior between the three regions implies two primary effects causing the pressure rise with a transitional period bridging the two as well as a dependence on the rate of cycling.

Utilizing nonlinear regression to fit the data, a paralinear behavior with regard to cycle number can be seen. The early stages demonstrated a primarily parabolic behavior that is dependent on $N^{1/2}$, while the later stage transitions into a linear region that is dependent on N [65]. The paralinear behavior can be described by $a + k_p N^{1/2} + k_l N$, where a is the original internal cell pressure, N is the cycle number, and k_p and k_l are the parabolic constant and linear constant. The r^2 values for each cell demonstrate a good fit of the internal pressure with cycle number [49].

Table 5-4 Parabolic and linear constants for the pressure rise of each cell including goodness of fit.

	Cell 01	Cell 02	Cell 03
K_p	3.292	1.947	5.696
K_l	-0.02574	0.1433	-0.158
r^2	0.9675	0.9406	0.9652

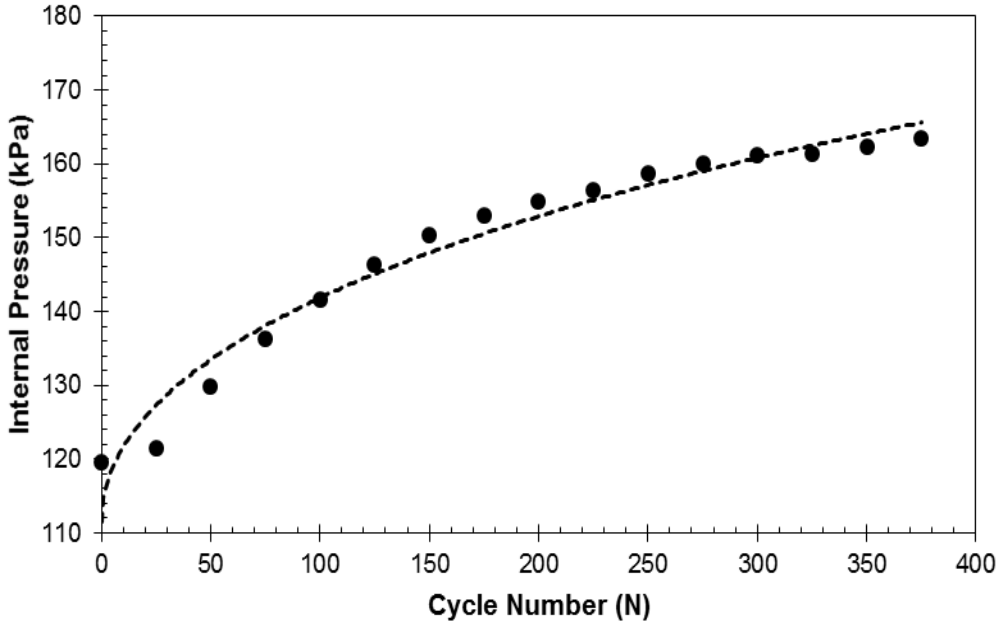

Figure 5-27 Internal pressure evolution of Cell 01 cycled at 1C charge and 2C discharge. The measurements recorded at the beginning of each baseline procedure.

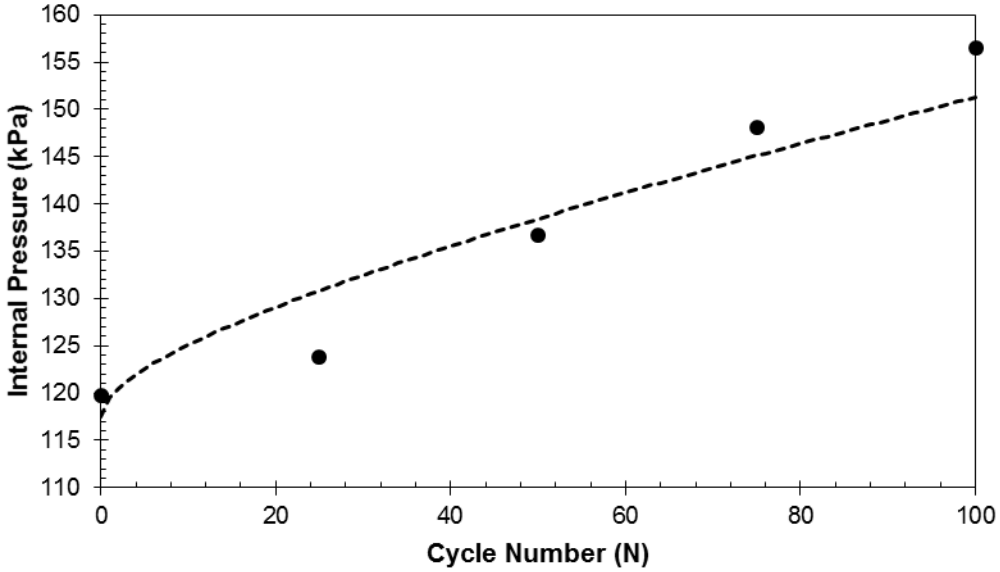

Figure 5-28 Internal pressure evolution of Cell 02 cycled at 2C charge and 1C discharge. The measurements recorded at the beginning of each baseline procedure.

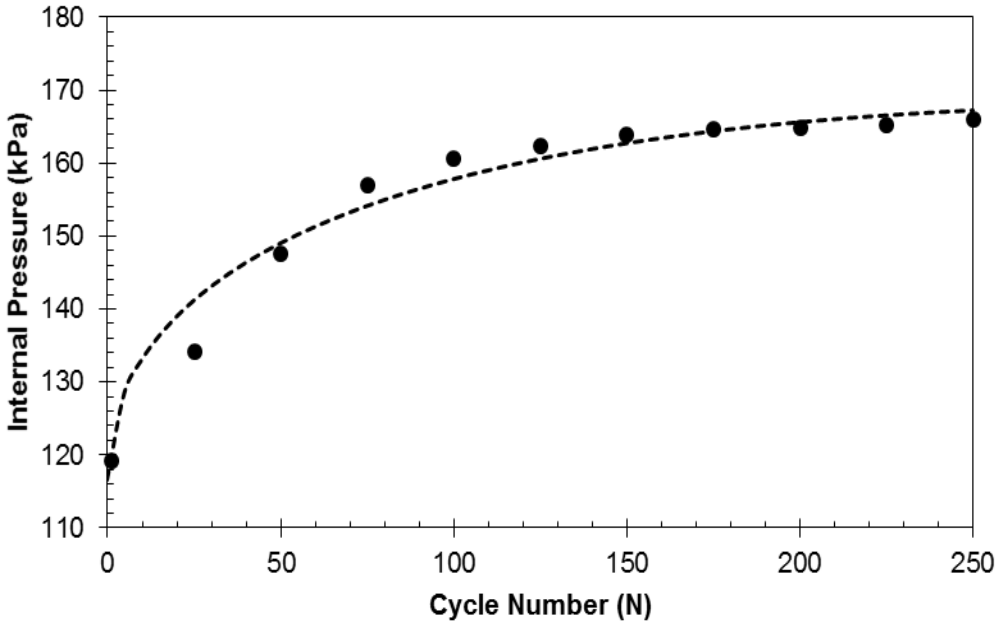

Figure 5-29 Internal pressure evolution of Cell 03 cycled at 2C charge and 2C discharge. The measurements recorded at the beginning of each baseline procedure.

A comparison of all three cells (Figure 5-30) illustrates the variance of internal pressure evolution versus cycle number for the given cycling rates. All three cells experienced a similar pressure rise over the full lifecycle ranging from 36.7 to 46.8 kPa, however it is apparent that the rate of pressure rise increases with cycling rate. It can be seen that the progression follows the following order Cell 01 < Cell 02 < Cell 03. Examining the average rate of rise of each cell over the first region, 0.205, 0.3672, and 0.567 kPa/cycle, quantifies this difference and illustrates an apparent cumulative effect that the high rate charge (Cell 02) and subsequent high rate charge and discharge (Cell 03) have on the system.

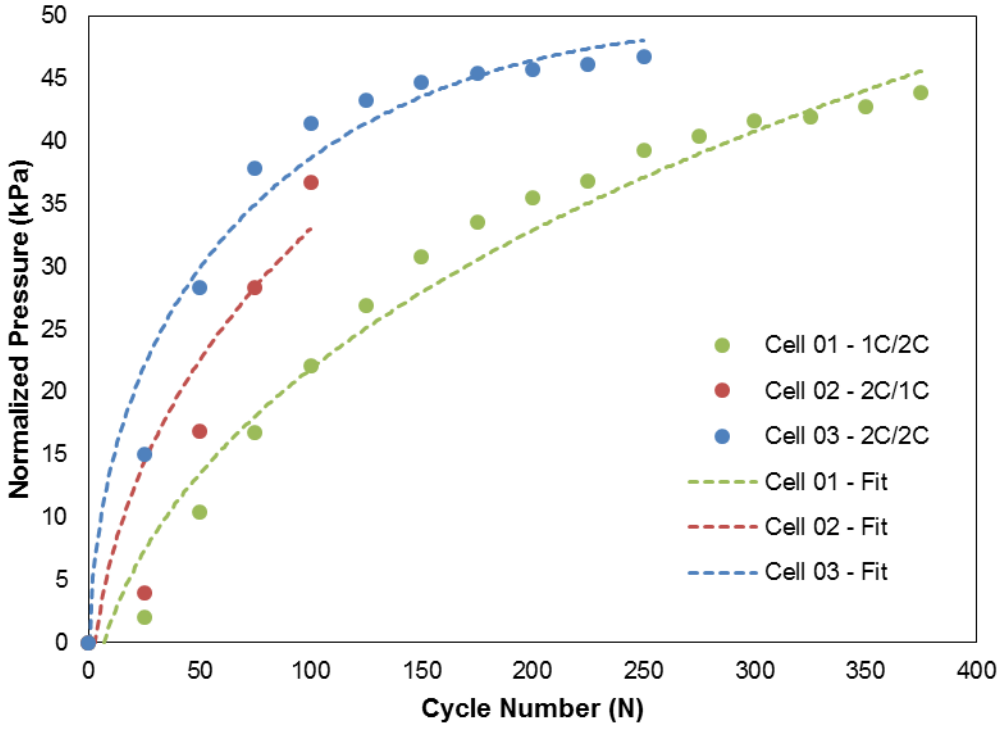

Figure 5-30 Internal pressure evolution of Cells 01-03 cycled at various charge and discharge rates.

Capacity Fade

Full cell discharge capacity curves, as seen in Figure 5-31 through Figure 5-33, were measured at the terminals of the test chamber during the baseline discharge at C/5 rate and 25 °C ambient discharge from 4.2-2.8 V. Cell 01 has a relatively linear capacity fade averaging 0.16% per cycle over the first region, 0.12% per cycle over regions two and three. The capacity of Cell 02 fades rather quickly with an average capacity fade of 0.56% per cycle over the first 75 cycles and increasing to 0.88% per cycle over the final 25 cycles. Cell 03 experiences a distinct capacity fade of 18% after the first 25 cycles, with a 6.6, 5.5 and 5.2% drop after 50, 75 and 100 cycles respectively. The capacity fade continues to slow to 3.8% after 125 cycles, and then falls off to an average 1% fade every 25 cycles out to 250.

During the first region of Cells 01 and 03 the principal cell degradation is evident in the low voltage region (below 3.5 V) associated with the depth of discharge. The discharge curves show minimal difference above this voltage. In contrast, the discharge cycles in the third region demonstrate minimal change in the low voltage region and a larger shift in the higher voltage region. Cell 02 appears to experience degradation in the low voltage region over the first 75 cycles, while the final 25 cycles experience degradation in both the low and high voltage regions. The shift in the discharge capacity curves of the higher voltage region is thought to primarily originate from an increase in total cell impedance. The behavior of the capacity degradation compared to the pressure rise appear to have similar behaviors for each of the cells.

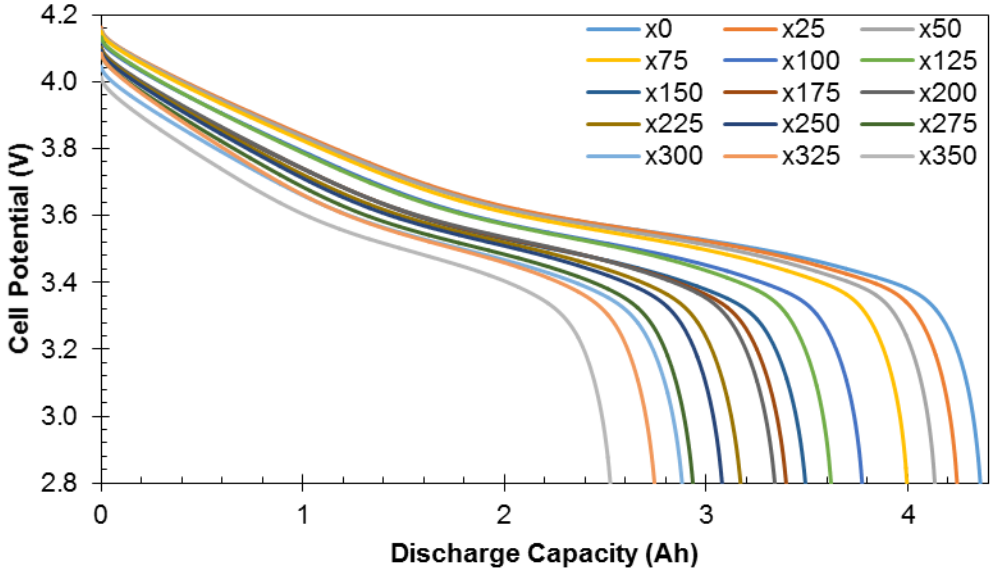

Figure 5-31 Cell 01 C/5 discharge capacity curves from 4.2 to 2.8 V at various cycles.

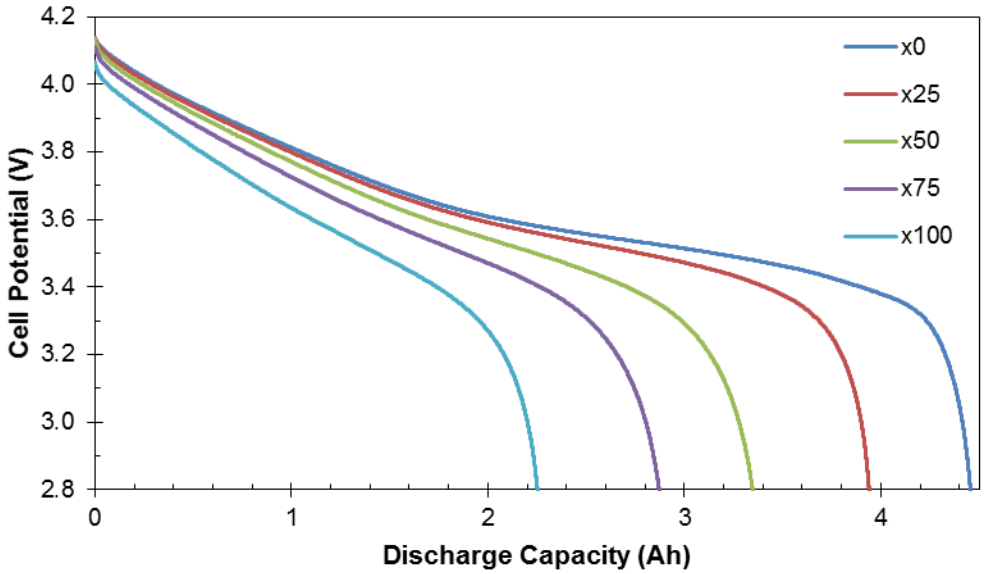

Figure 5-32 Cell 02 C/5 discharge capacity curves from 4.2 to 2.8 V at various cycles.

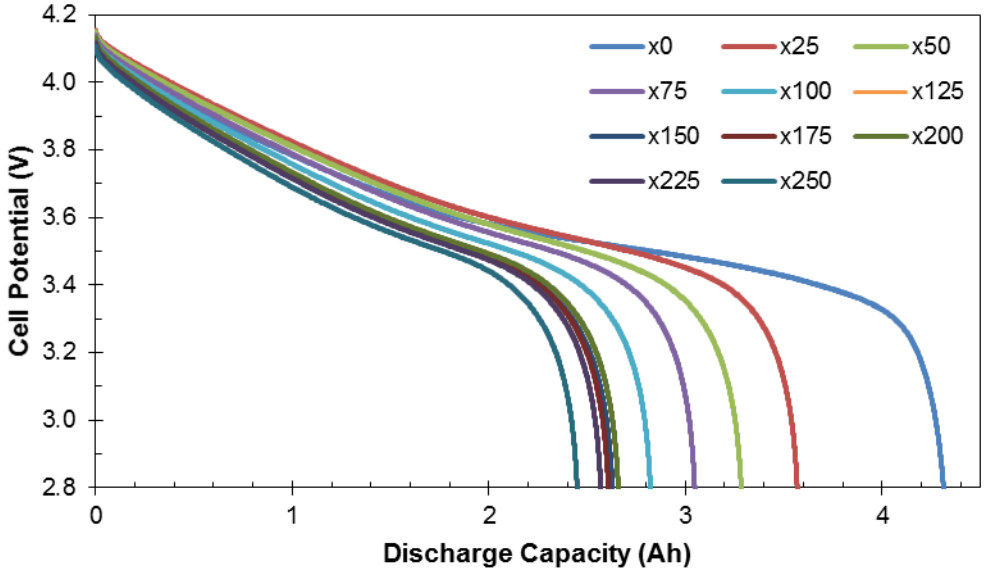

Figure 5-33 Cell 03 C/5 discharge capacity curves from 4.2 to 2.8 V at various cycles.

Employing the previously described nonlinear regression approach to fit the capacity data, Figure 5-34 demonstrates a similar paralinear behavior to that seen in the internal pressure data. Again, the early stages demonstrate a parabolic behavior that is dependent on $N^{1/2}$, and the later stages transition into an N dependent linear region. The behavior is described by $b + k_p N^{1/2} + k_l N$, where b is the original cell capacity, and N is the cycle number. Again, the r^2 values for each cell demonstrate a good fit of the internal pressure with cycle number

Table 5-5 Parabolic and linear constants for the capacity fade of each cell.

	Cell 01	Cell 02	Cell 03
K_p	-0.1361	-0.1581	-0.3223
K_l	-0.00445	-0.00475	0.01039
r^2	0.9934	0.9638	0.9511

A comparison of all three cells in Figure 5-34 illustrates the difference in capacity fade versus cycle number for each cell. It is apparent that the cycling rate of each of the cells has a significant effect on the capacity fade of the cell. While Cell 01 has a has a typical capacity fade curve, Cells 02 and 03 experience a much higher rate of reduction in capacity at the early stages of cycling. It can also be seen that Cell 03 appears to stabilize before reaching the 60% capacity fade test point, while Cell 02 does not.

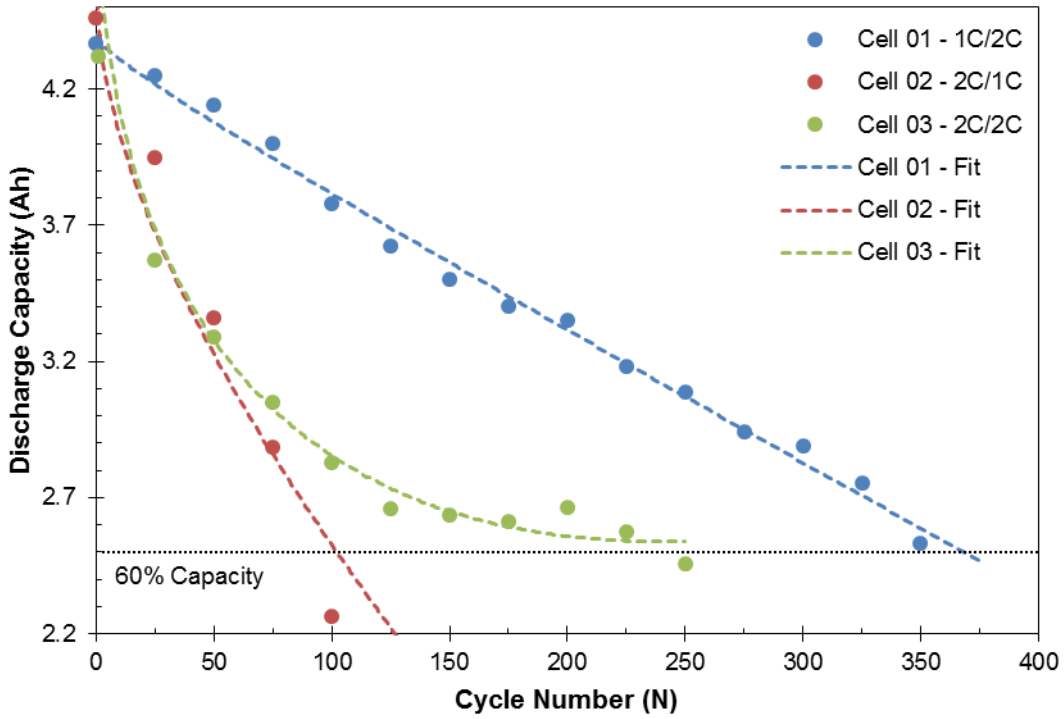

Figure 5-34 Discharge capacity fade and nonlinear regression fit of Cells 01-03 from.

Statistical Correlation

Examining the behavior of both the pressure rise and capacity fade over the lifecycle of each cell, it is evident that both experience similar regions in which the rate

of change varies with cycle number. In order to examine this parallel, a statistical dependence between the two variables can be assessed. Figure 5-35 through Figure 5-37 demonstrates an apparent linear relationship between the pressure and capacity over the lifecycle of the cell. Due to the small sample size and non-normal distribution of the data, the Spearman's rank correlation coefficient (SRCC) is used to assess the closeness of the relationship between the variables using the monotonic function [59]. Equation 5-6 describes the SRCC, for a sample size n, where the data (X_i, Y_i) is converted to a rank (x_i, y_i) and the rank difference is computed ($d_i = x_i - y_i$).

$$r_s = 1 - 6\sum d_i^2 / n(n^2 - 1) \tag{5-6}$$

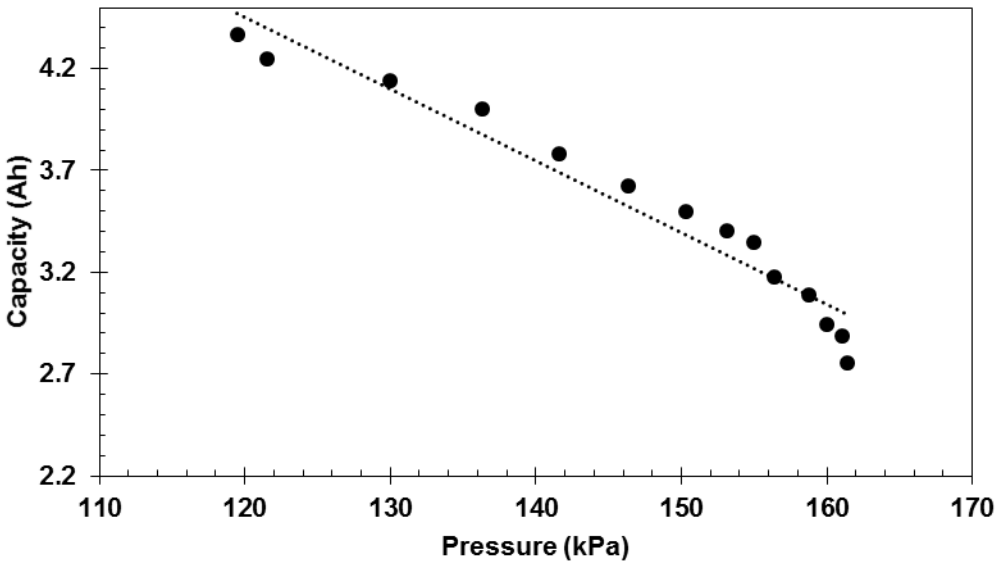

Figure 5-35 Cell 01 linear relationship of capacity versus internal pressure over the full lifecycle, with a very strong, statistically significant SRCC.

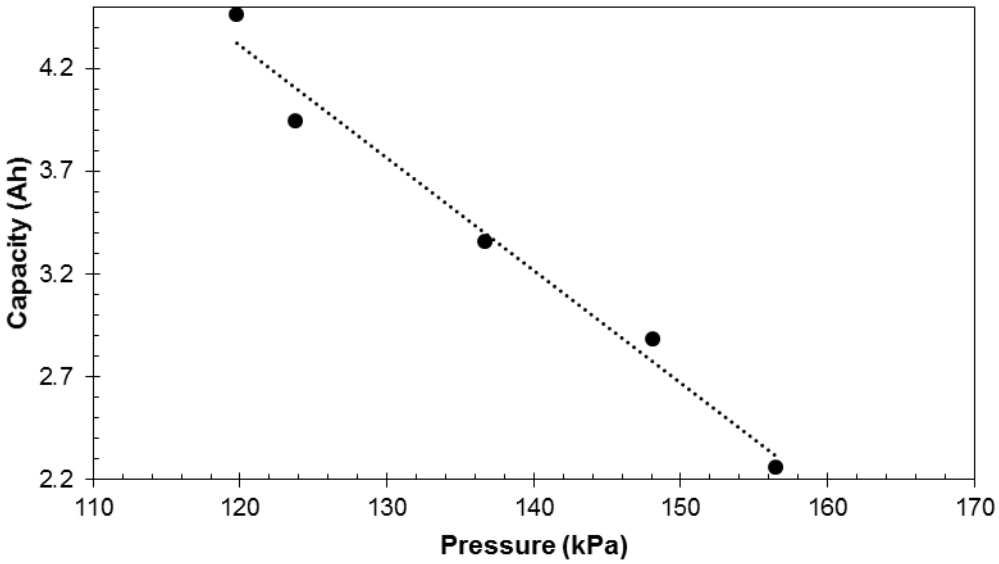

Figure 5-36 Cell 02 linear relationship of capacity versus internal pressure over the full lifecycle, with a very strong, statistically significant SRCC.

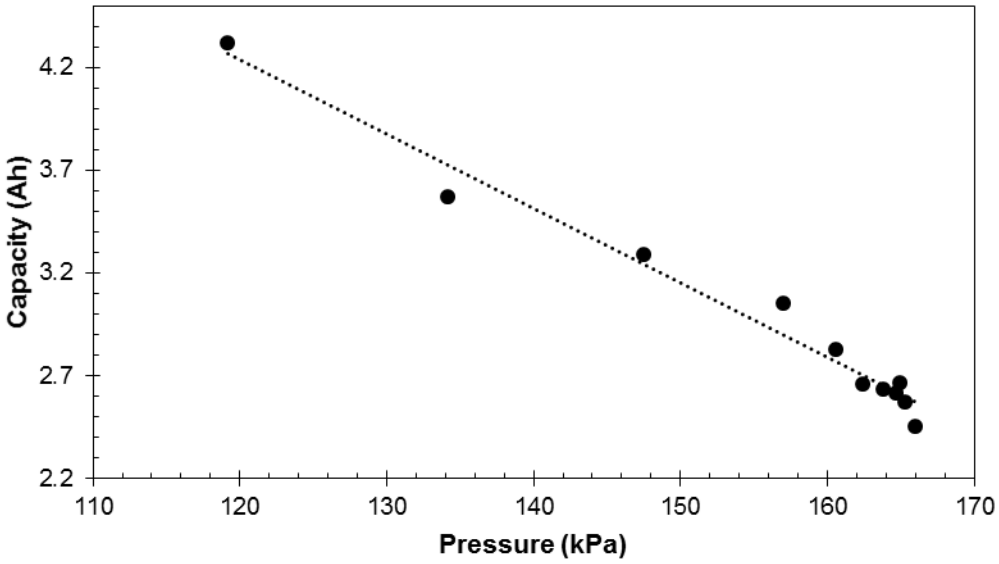

Figure 5-37 Cell 03 linear relationship of capacity versus internal pressure over the full lifecycle, with a very strong, statistically significant SRCC.

The resulting SRCC value for these variables can be seen in Table 5-6, and indicate a very strong monotonic relationship between the rise in pressure and the fade in capacity for all three cells. A two tail t-test was performed on the data set (Table 5-6), and the Spearman correlation was found to have statistical significance for all three cells. The very strong monotonic relationship with statistical significance, supports that there is an association between the pressure rise and capacity fade, however it does not confirm the direction of causation. In other words, the change in pressure can be correlated to the change in capacity, but it is unclear as to the cause and effect. To better understand the aging mechanisms present in this cell and to identify the direction of causation, additional testing, modeling, and analysis was conducted including GC-MS, SEM, and EIS.

Table 5-6 SRCC and two tail t-test results for the comparison of the pressure rise and capacity fade for Cells 01-03.

	Cell 01	Cell 02	Cell 03
r_s	-1.0	-1.0	-0.9455
n	15	5	11
d_f	-	-	9
$P_{two\text{-}tail}$	P < 0.5	P < 0.5	0.000011 < 0.05

Gas Generation Behavior

GC-MS measurements of the gases generated inside of the test chamber were performed at the conclusion of lifecycle testing for each cell. The results of the analysis are displayed in Figure 5-38 through Figure 5-40 and the composition of the gas

included CO, CO_2, CH_4, C_2H_6, and C_3H_8 as identified in the MS results. CO has been shown to be a product of the reduction reaction of EC [5], [66], and CO2 has been shown to primarily be the product of either dry room contaminates (CO_2 or O_2) during production or from two internal processes. The first process is the reaction of CH_3OCO_2Li with trace amounts of H_2O or HF impurities in the electrolyte [39], [66].

$$2C_2H_5OCO_2Li + H_2O \rightarrow Li_2CO_3 + 2C_2H_5OH + CO_2 \quad (5\text{-}7)$$

$$C_2H_5OCO_2Li + HF \rightarrow LiF + C_2H_5OH + CO_2 \quad (5\text{-}8)$$

The second process is an oxidation reaction of DEC with O_2 [39], [66].

$$(C_2H_5O)_2CO + 6O_2 \rightarrow 5CO_2 + 5H_2O \quad (5\text{-}9)$$

The production of the hydrocarbon gases are understood to be as follows [66].

$$DEC + 2Li^+ + 2e^- + H_2 \rightarrow Li_2CO_3 \downarrow + 2C_2H_6 \uparrow \quad (5\text{-}10)$$

$$DEC + 2Li^+ + 2e^- + H_2 \rightarrow CH_3CH_2CO_2OLi \downarrow + 2C_2H_6 \uparrow \quad (5\text{-}11)$$

$$CH_3OCO_2CH_3 + e^- + Li^+ \rightarrow CH_3OCO_2Li \downarrow + CH_3^{\bullet} \quad (5\text{-}12)$$

$$CH_3OCO_2Li + e^- + Li^+ \rightarrow Li_2CO_3 \downarrow + CH_3^{\bullet} \quad (5\text{-}13)$$

$$CH_3^{\bullet} + \tfrac{1}{2}H_2 \rightarrow CH_4 \uparrow \quad (5\text{-}14)$$

$$CH_3^{\bullet} + CH_3^{\bullet} \rightarrow C_2H_6 \uparrow \quad (5\text{-}15)$$

$$C_2H_5OCO_2C_2H_5 + e^- + Li^+ \rightarrow CH_3OCO_2Li \downarrow + C_2H_5^{\bullet} \quad (5\text{-}16)$$

$$C_2H_5OCO_2Li + e^- + Li^+ \rightarrow Li_2CO_3 \downarrow + C_2H_5^{\bullet} \quad (5\text{-}17)$$

$$C_2H_5^{\bullet} + \tfrac{1}{2}H_2 \rightarrow C_2H_6 \uparrow \quad (5\text{-}18)$$

$$C_2H_5^{\bullet} + CH_3^{\bullet} \rightarrow C_3H_8 \uparrow \quad (5\text{-}19)$$

The production of CH_4, C_2H_6, and C_3H_8 is a result of the reduction of DEC and radical reactions on the surface of the graphite anode as discussed by Shin et al. [66]. These processes and results demonstrate that the gas products are not related to the type of cathode material. Furthermore, the reduction products are the primary components of the SEI film formation on the anode and can be accelerated by high rate cycling or high temperatures [4], [39].

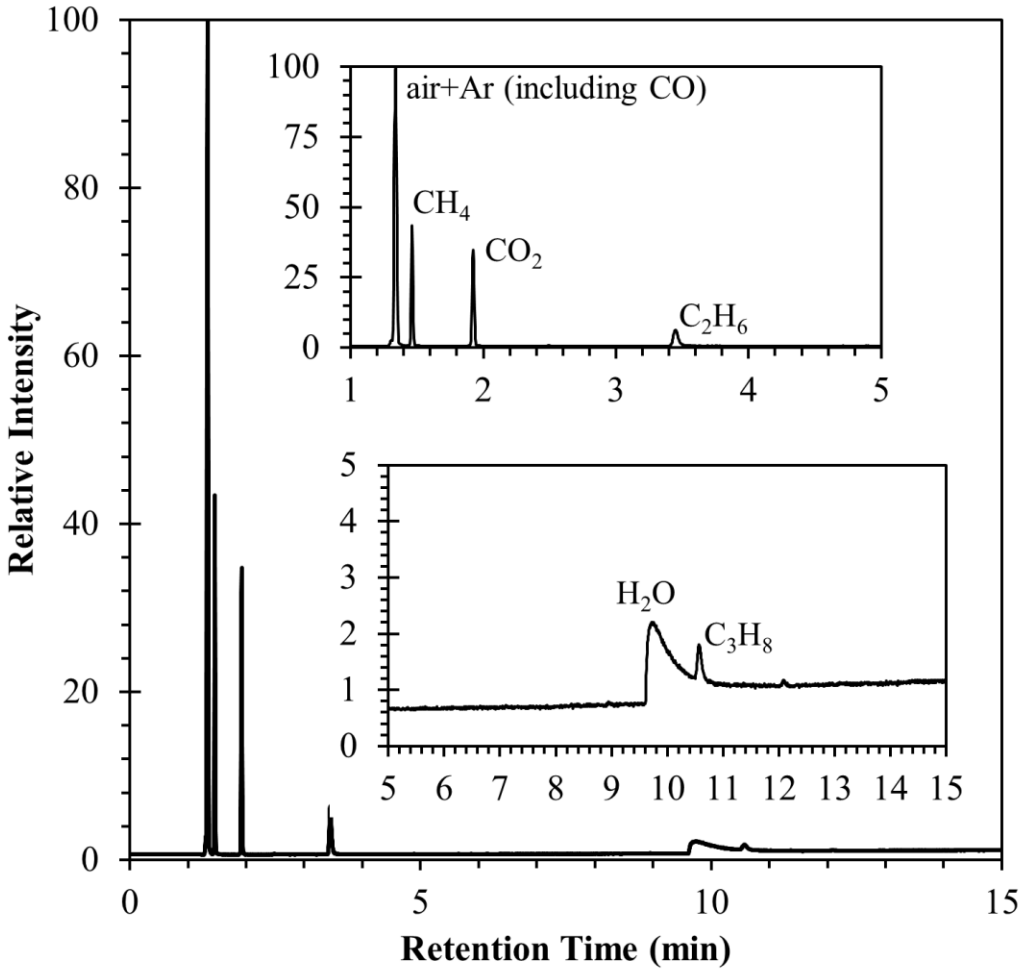

Figure 5-38 Cell 01 gas-chromatography of the extracted gas at the conclusion of cycling. Species marked in the figures are determined by corresponding mass-spectrometry results.

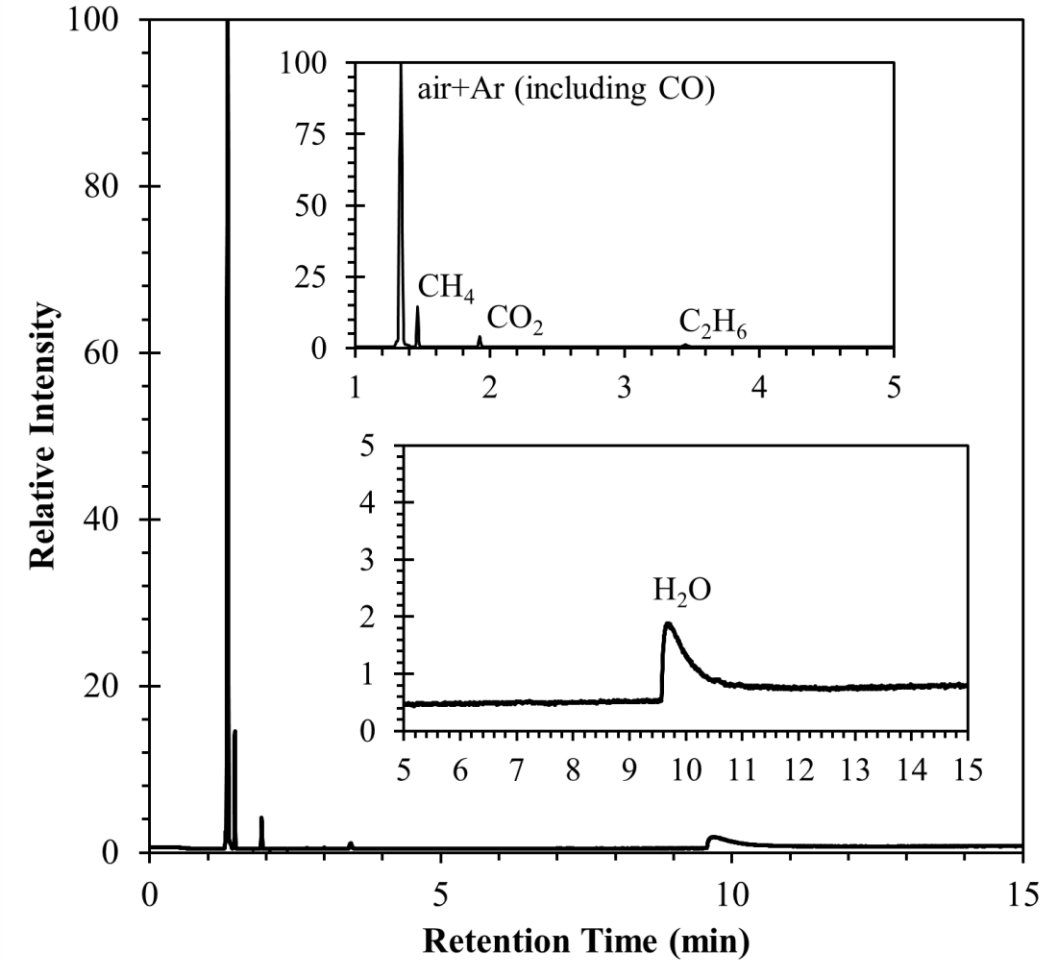

Figure 5-39 Cell 02 gas-chromatography of the extracted gas at the conclusion of cycling. Species marked in the figures are determined by corresponding mass-spectrometry results.

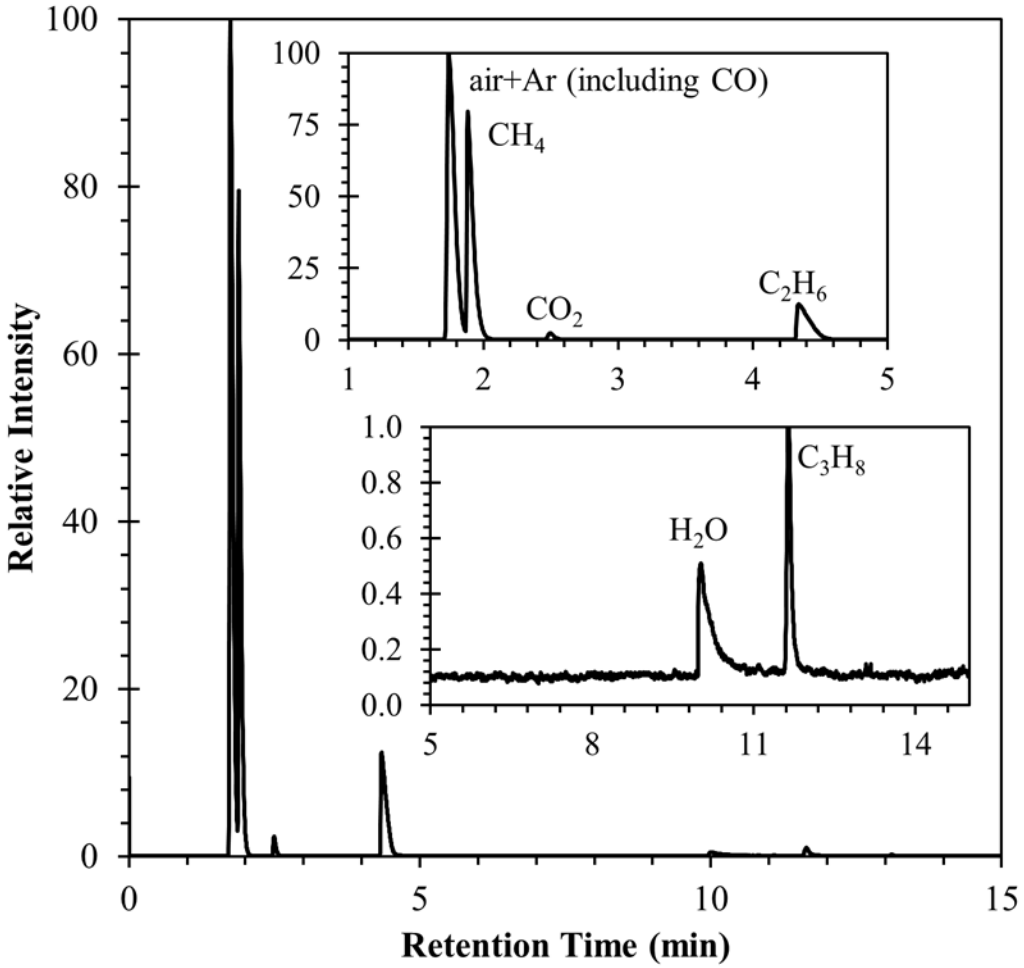

Figure 5-40 Cell 03 gas-chromatography of the extracted gas at the conclusion of cycling. Species marked in the figures are determined by corresponding mass-spectrometry results.

SEM Analysis

In the previous section, GCMS analysis shows the presence of gaseous byproducts of the electrolyte reduction occurring in each cell, however further analysis is required to identify any deposited layers on the electrode surface. By dismantling the cells after cycling and GCMS testing, an image of the surface of the electrodes using

SEM can be compared with the fresh state, non-cycled cells. Figure 5-41 shows the anode (a-c) and cathode (d-f) in their pre-cycled state where there is a clear contrast in the platelets of the hexagonal graphite and the individual grains of the $LiCoO_2$. The signal from the microscope is not impeded by nonconductive impurities resulting in a high resolution image. There is minimal evidence of large cracks formed in the non-cycled electrodes indicating that the process of dismantling the cell did not induce significant damage to the electrodes. Figure 5-42 through Figure 5-44 show the post cycled anode (a-c) and cathode (d-f) for Cells 01-03. Multiple samples were examined on both sides of the cathode and anode at various points along the roll and, while there were minor variations, these images are representative throughout. The contrast in these images are slightly blurred due to the easy charging of the electrode surfaces indicating that the surface chemistry of both cathode and anode have changed slightly due to the cycling conditions.

Examining the cathode images of the fresh cell compared to the cycled cells reveals little change. While some minor deposits can be seen in Figure 5-42f and Figure 5-43f, the various images of the cathodes from each cell indicate that the passivation layer on the cathode is relatively stable. While it is not visible in the SEM images, previous research by Li et al. utilized Transmission Electron Microscopy (TEM) to identify cracks and pores that appeared in the $LiCoO_2$ particle after elevated cycling [42], [67]. This causes a decrease in utilization of active material on the cathode and contributes to the loss in capacity at the cathode of cells that are cycled at high rates.

An examination of each of the cycled anodes clearly demonstrates a deposited layer on the surface of the electrode, which is considered to be a passivated surface layer because the binder cannot be observed by SEM [3], [64], [68]. The previously

discussed side reactions form this layer at areas of contact between electrolyte and bare carbon. The corrosion of the graphite changes the surface chemistry of the anode to the point where these reactions are no longer favorable causing these reactions to slow as is evidenced in the gas evolution in Figure 5-27 and Figure 5-29.

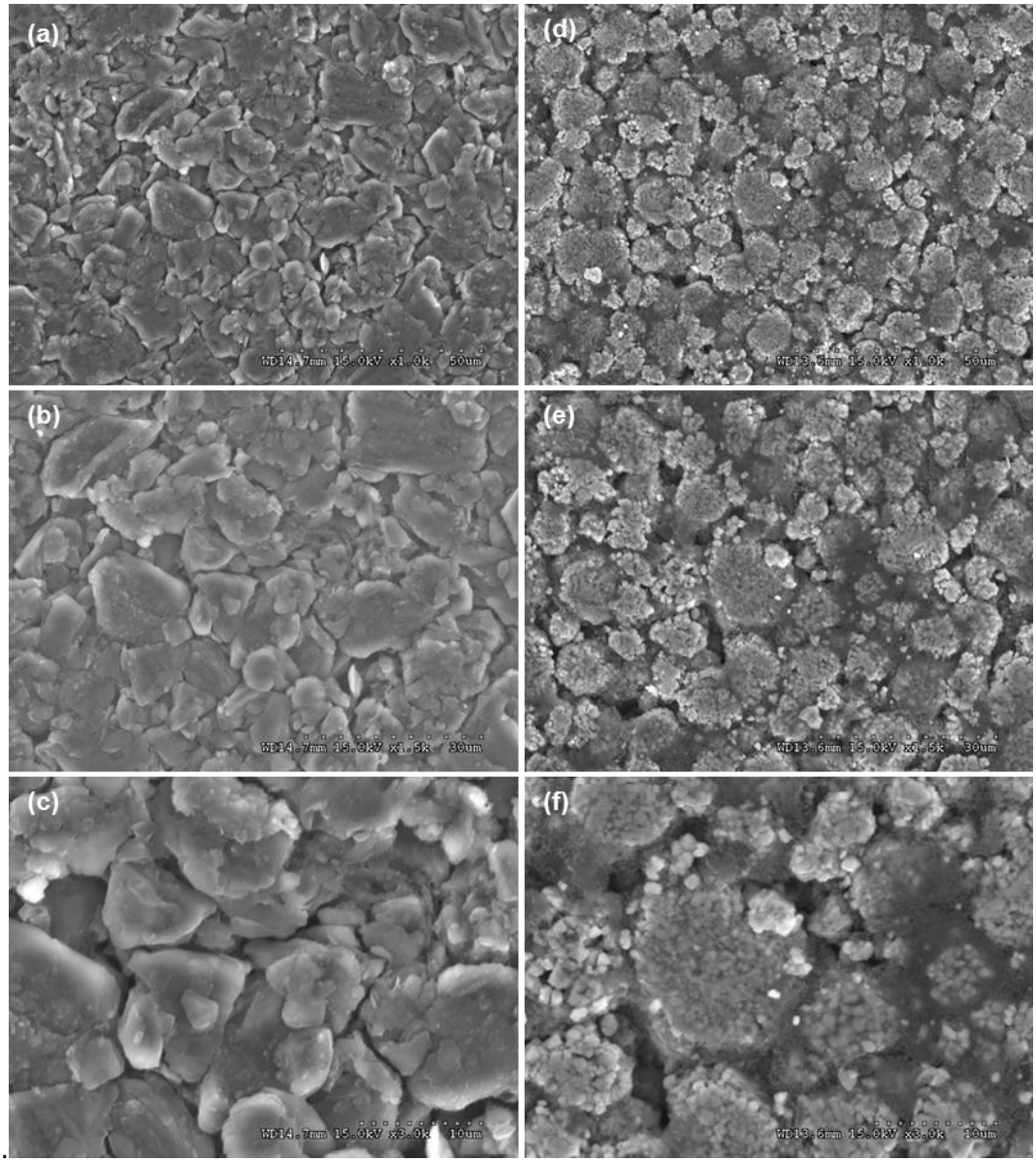

Figure 5-41 Increasing magnitude SEM images of a fresh graphite anode (a-c), and $LiCoO_2$ cathode (d-f).

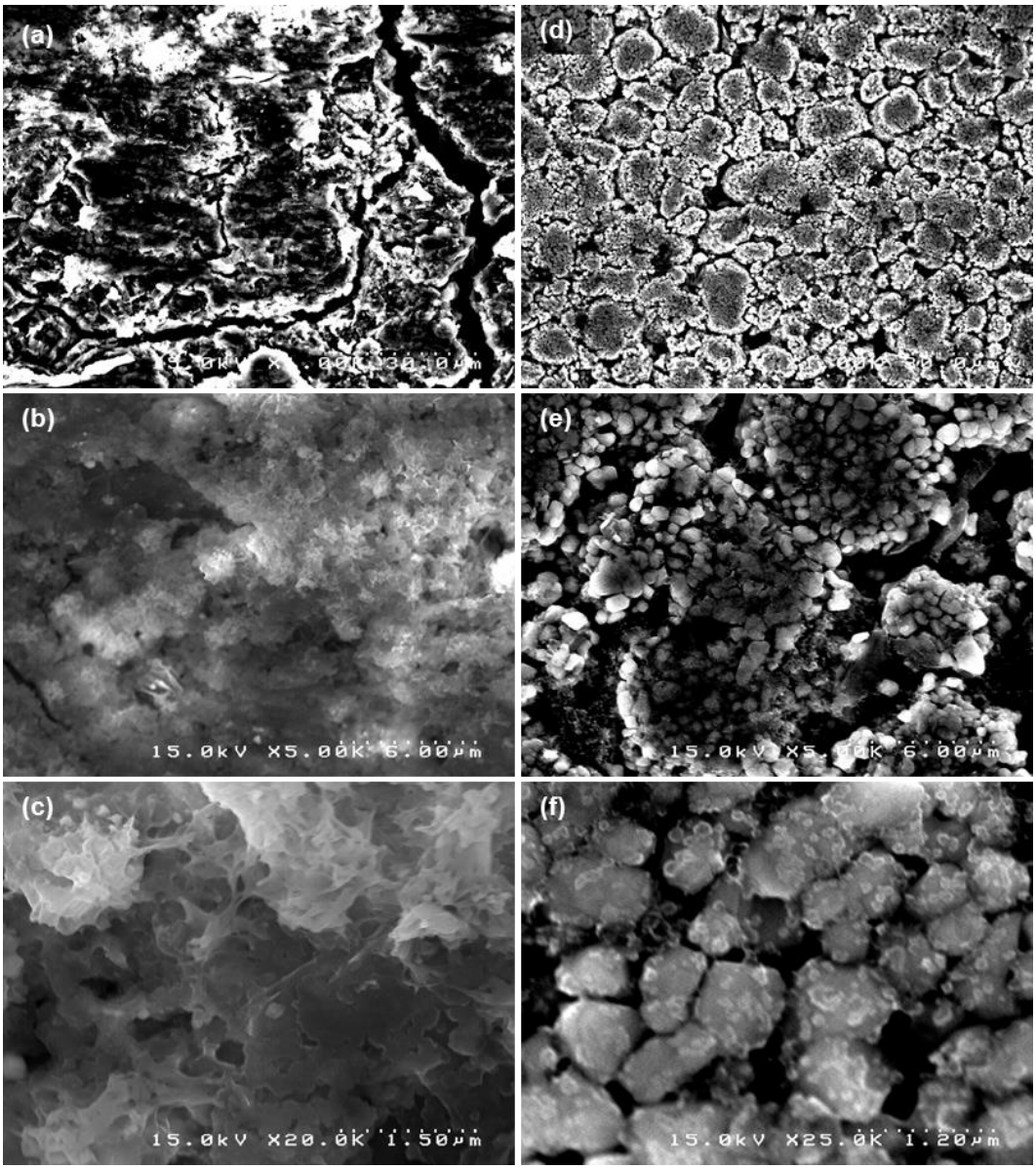

Figure 5-42 Increasing magnitude SEM images of Cell 01 graphite anode (a-c), and $LiCoO_2$ cathode (d-f).

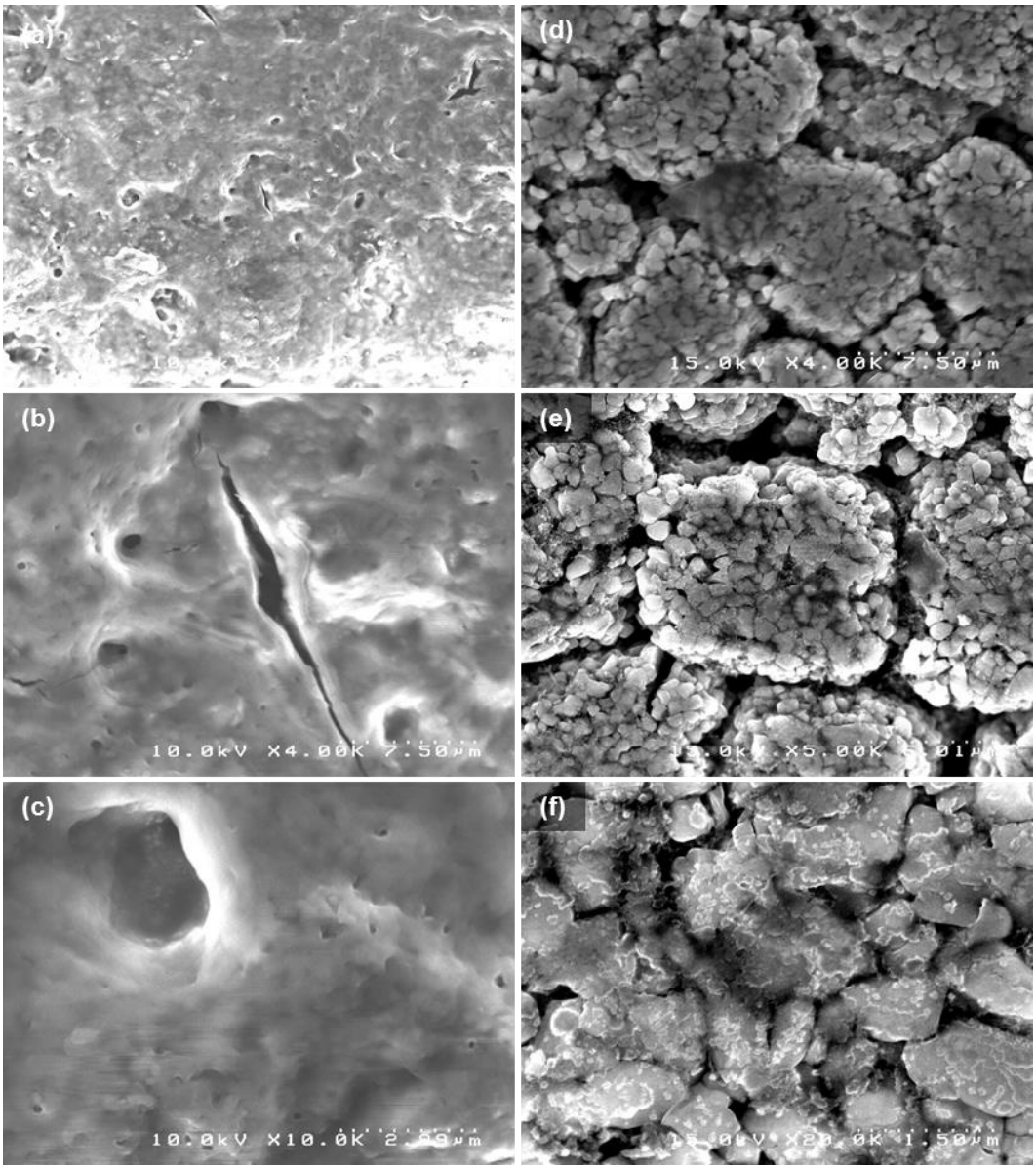

Figure 5-43 Increasing magnitude SEM images of Cell 02 graphite anode (a-c), and $LiCoO_2$ cathode (d-f).

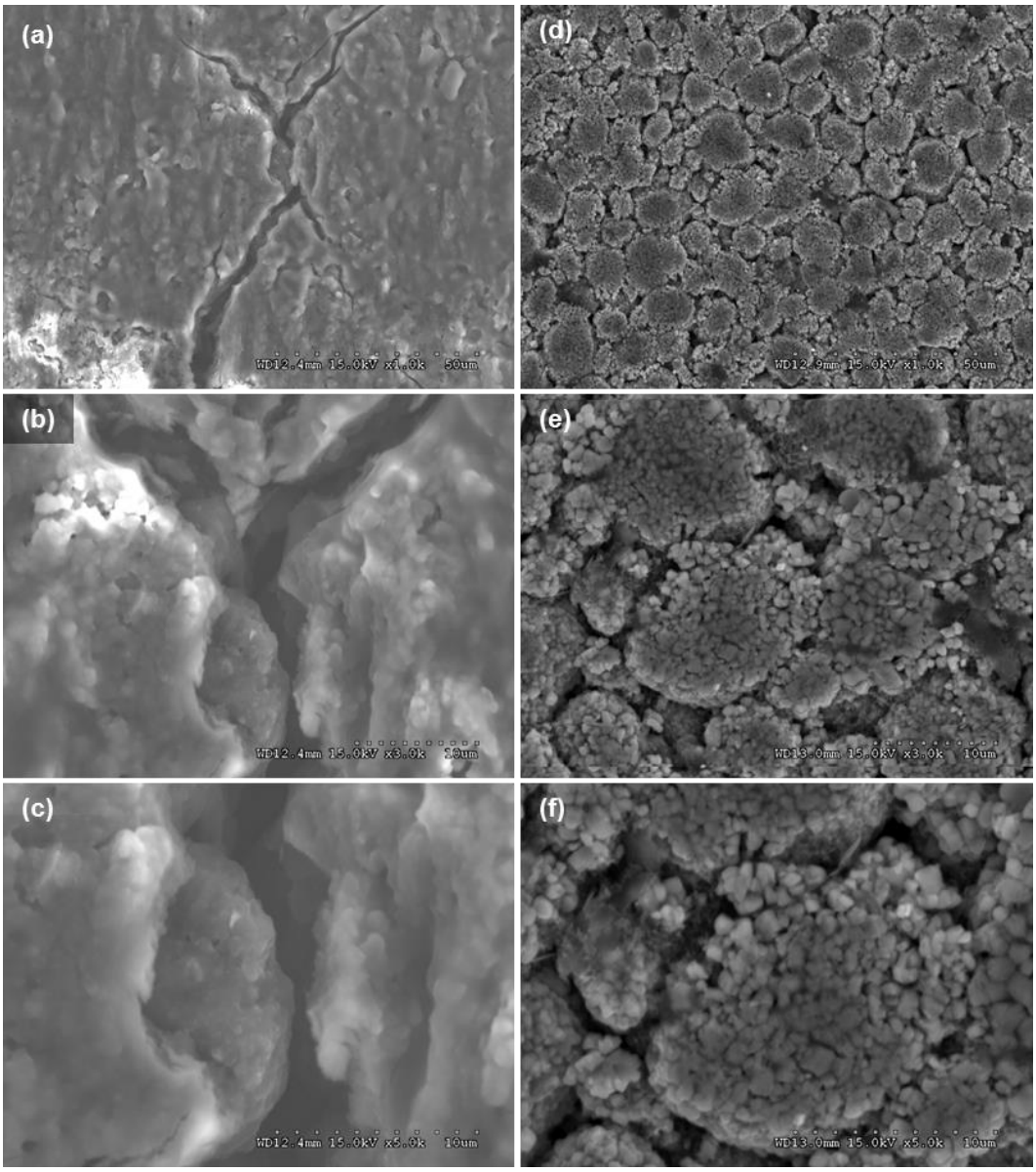

Figure 5-44 Increasing magnitude SEM images of Cell 03 graphite anode (a-c), and $LiCoO_2$ cathode (d-f).

A large crack formation in the deposited layer of the anode can be seen in the center of Figure 5-44a. The high rate cycling and high state of charge can induce mechanical strain on the graphite lattice caused by insertion and de-insertion leading to cracks, fissures, and splits. These openings allow further surface reaction at these

sites potentially leading to the continued slow pressure rise in the cell at higher cycle numbers [3]. While this layer is ionically conductive, it leads to an increase in charge transfer resistance, impedance, and clogged pores on the carbon anode leading to an irreversible capacity loss. Additionally, the lithium molecules can become trapped in the layer contributing to a loss in capacity.

EIS Analysis

Figure 5-45a through Figure 5-47a illustrates the evolution of the normalized EIS spectra for Cells 01-03 as they are cycled at 100% SOC. The symbols represent the experimental data, while the solid lines represent the simulation using the modified Randles circuit shown in Figure 4-5. The progression of the Ohmic resistance for each cell is seen in Figure 5-45b through Figure 5-47b. The EIS curves begin with a semicircular arc at the middle frequencies followed by a sloped diffusion tail at the lower frequencies. The middle frequency arc is related to two processes occurring at the electrode-electrolyte interface, namely the SEI resistance (R_{SEI}) coupled with the SEI capacitance (C_{SEI}), and the charge-transfer resistance (R_{CT}) paralleled with the double-layer capacitance (C_{DL}) [69], [70]. While it is not possible to positively identify the contribution of each electrode to the overall EIS spectrum without a three electrode or split cell setup, the full cell EIS data coupled with the previous analysis can provide insight. Similar to the behavior seen in the pressure and capacity, the EIS spectra has an early stage in which the middle frequency arc width (R_W) grows presumably due to the growth of the SEI layer on the anode and the resultant increase in R_{SEI}. The EIS then begins to transition to two distinguishable arcs implying a stronger contribution of the charge-transfer kinetics and Li^+ transport through the SEI [49].

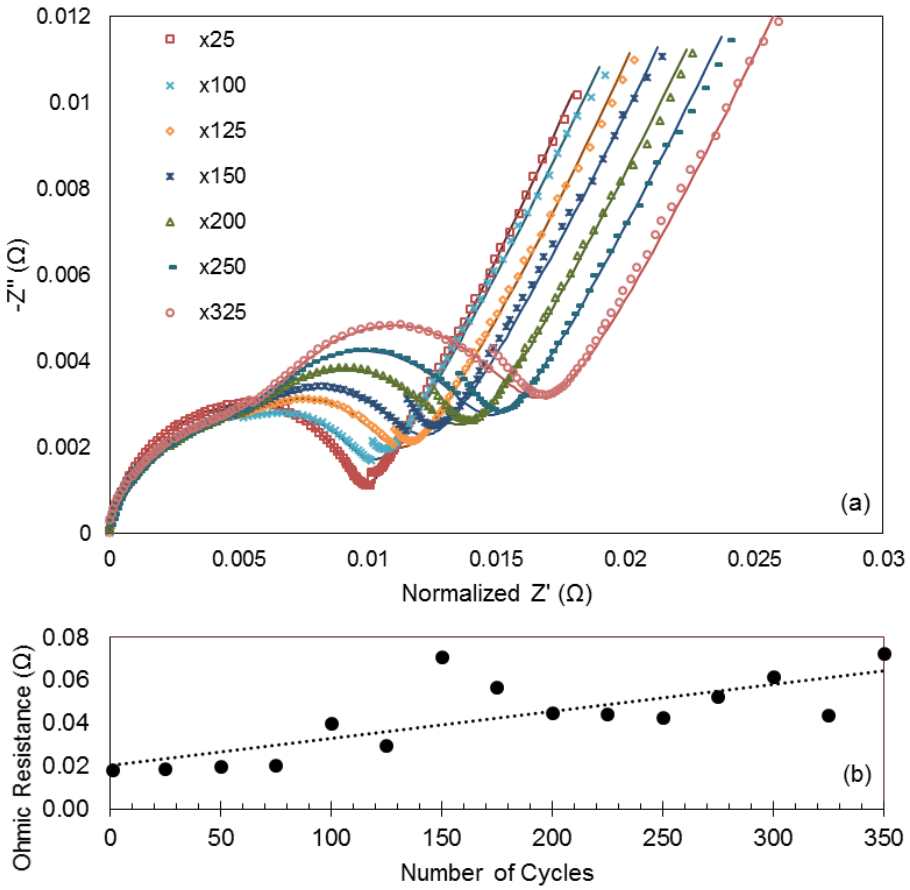

Figure 5-45 Cell 01 (a) Normalized Nyquist plots and (b) ohmic resistance progression of electrochemical impedance spectra measured at 100% SOC after various cycles.

Table 5-7 Model fitting parameters for the impedance spectra of Cell 01.

Cycle	R_S	R_{SEI}	C_{SEI}		R_{CT}	C_{PE}		W
			Y0	N		Y0	N	
25	17.9	5.87	956	0.725	4.19	2.36	0.88	328
100	39	7.14	2.38	0.655	3.03	8.81	0.934	297
125	28.8	7.44	2.78	0.632	3.75	9.41	0.937	290
150	70	6.77	2.44	0.651	5.2	9.52	0.882	281
200	43.8	7.32	2.71	0.62	6.02	9.18	0.904	283
250	41.3	7.42	2.56	0.615	7.07	8.53	0.901	276
325	42.4	7.89	2.35	0.61	8.36	7.89	0.898	254

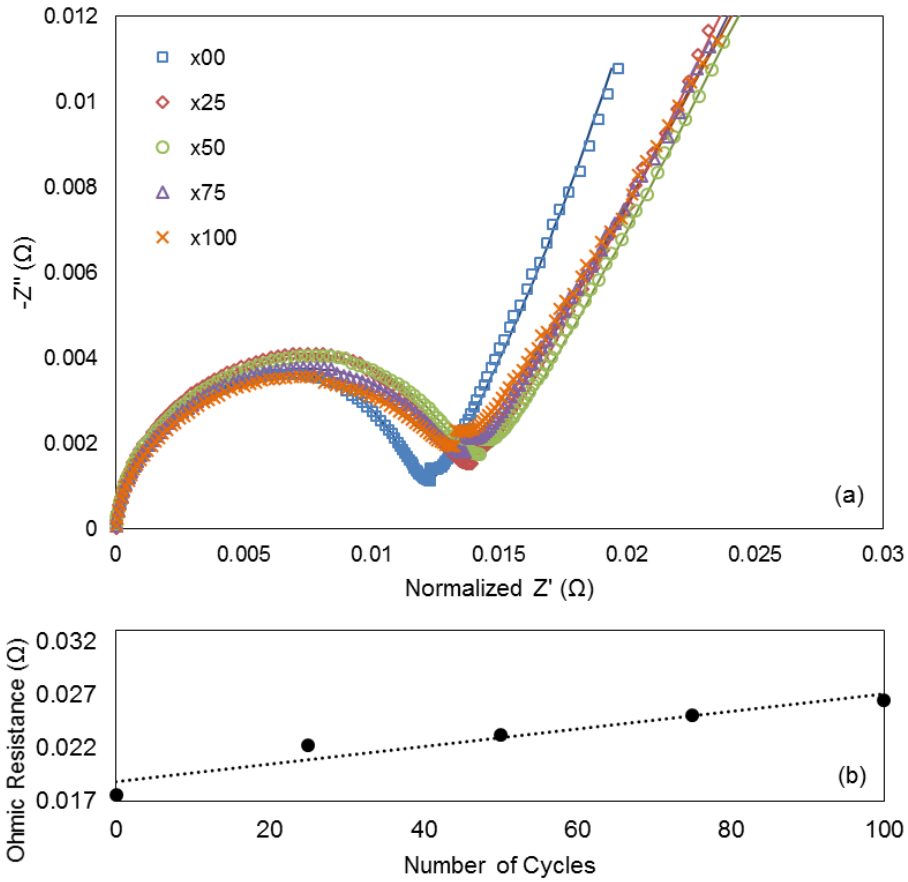

Figure 5-46 Cell 02 (a) Normalized Nyquist plots and (b) ohmic resistance progression of electrochemical impedance spectra measured at 100% SOC after various cycles.

Table 5-8 Model fitting parameters for the impedance spectra of Cell 02.

Cycle	R_S	R_{SEI}	C_{SEI}		R_{CT}	C_{PE}		W
			Y0	N		Y0	N	
0	16.8	5.87	546	0.753	6.59	1.58	0.838	365
25	21.5	5.15	487	0.786	8.6	1.48	0.797	262
50	22.2	8.14	1100	0.67	6.29	2.8	0.81	247
75	24	8.41	1320	0.648	5.47	3.78	0.799	244
100	16.8	5.87	546	0.753	6.59	1.58	0.838	365

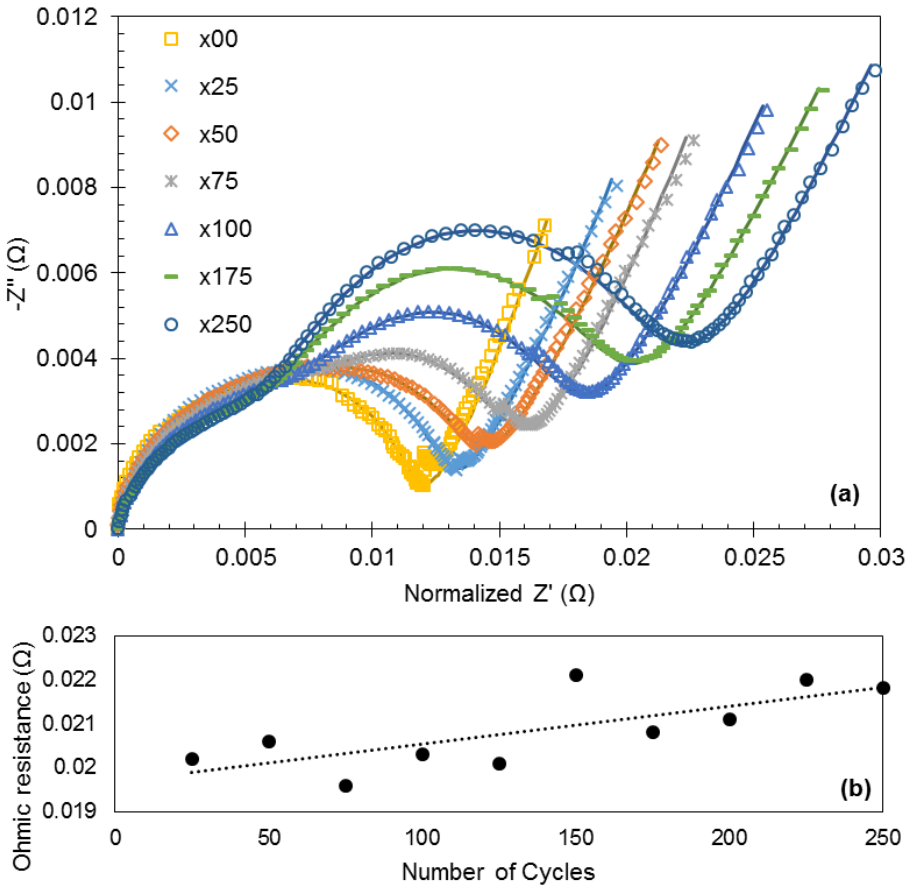

Figure 5-47 Cell 03 (a) Normalized Nyquist plots and (b) ohmic resistance progression of electrochemical impedance spectra measured at 100% SOC after various cycles.

Table 5-9 Model fitting parameters for the impedance spectra of Cell 03.

Cycle	R_S	R_{SEI}	C_{SEI}		R_{CT}	C_{PE}		W
			Y0	N		Y0	N	
0	74.2	7.81	1.57	0.804	4.38	0.276	0.851	449
25	20.2	7.97	0.967	0.685	5.82	2.72	0.85	351
50	20.6	9.94	1.83	0.621	4.84	6.21	0.854	311
75	19.6	11.8	2.91	0.566	4.63	9.49	0.938	323
100	20.3	11.6	3.81	0.531	6.96	9.64	0.935	284
175	20.8	9.28	3.84	0.539	10.6	8.68	0.9	259
250	21.8	8.59	3.6	0.549	12.9	7.98	0.898	250

An examination of previous research suggests that the medium frequency semicircle is derived from the passive film on the electrodes, particularly the cathode [42], [50], [70]. An examination of the R_{SEI} values for Cells 01-03 (Table 5-7 through Table 5-9) illustrate a minimal variation during cycling implying a stable passivation layer on the cathode of each cell which is consistent with the SEM analysis. As both the cathode and anode contribute to the low frequency semicircle, R_{CT} is the sum of the interfacial resistances including the surface film resistance and internal charge transfer resistance. Examining the modeling values for Cell 01 and 03 shows a significant growth in the R_{CT} value which is evident in the Nyquist plots. When combined with the SEM analysis it appears that this rise is primarily due to the excessive passivation layer on the anode. The R_{CT} values for Cell 02 remain relatively stable throughout cycling implying that while the electrolyte may be decomposing with the elevated charge rate, the excessive passivation layer has not yet formed.

Conclusions

Internal pressure evolution and capacity fade of commercially available 26650 lithium-ion cells with $LiCoO_2$/graphite electrodes were examined throughout high rate charge-discharge cycle testing at 25 °C. The cells demonstrated poor cycling capability with Cell 01 experiencing 37% capacity fade or 2.53 Ah after 375 cycles, Cell 02 experiencing 43% capacity fade or 2.26 Ah after 100 cycles, and Cell 03 experiencing 39% capacity fade or 2.45 Ah after 250 cycles. Both the internal pressure rise and capacity fade demonstrated a paralinear behavior that is primarily parabolic in the early stage with a dependence on the square root of the cycle number. This was followed by a transition to the final region with a linear dependence on cycle number. A closer

examination of the pressure and capacity evolution presented a direct correlation indicating a very strong, statistically significant monotonic relationship.

From the GC-MS analysis, the gases generated during repeated cycling are CO, CO_2, CH_4, C_2H_6, and C_3H_8 with CH_4 being the main gaseous product. The gases are produced at a high rate in the early stage of cycling with a transition to a slow linear production in the later stage. Previous work has indicated that the hydrocarbon gases are a product of the reduction of DEC on the surface of the anode and are the primary components of the SEI film formation. A comparison of the low and high resolution SEM images for all three cells clearly demonstrates that the decomposition of the electrolyte seen in the GC-MS analysis was dominated by the reduction reaction at the surface of the anode, as well as crack formations inducing continued electrolyte reduction. Images of the cathode demonstrated minimal changes between the pre and post cycled cells indicating minimal contribution to the production of gas. EIS analysis demonstrated the same staged behavior experienced by the pressure and capacity with a small R_{SEI} growth in the early stages, and a transition to a stronger contribution of the charge-transfer kinetics and Li^+ transport through the SEI in the later stages.

The data and analysis presented of pressure evolution, capacity fade, and the correlation of the two for a given system can be a useful diagnostic tool aiding in the prediction of cell life or damage. While the work presented here is representative of $LiCoO_2/C_6$ cells manufactured by the Tenergy company, systems in which the primary degradation mechanisms feature gas evolution can be analyzed by this method adding an additional in-situ measurement that can be used as a substitute or to supplement other more conventional diagnostic tools. Additionally, this method may be of particular use for systems that are cycled at high rate, high temperatures, or both.

Chapter 6

Summary and Conclusions

Summary

The study of in-situ internal pressure behavior of a lithium-ion battery during cycling, aging, and damage was conducted in order to examine the metric as a means of predicting the aging or damage of a battery. Various studies were conducted in order to examine the internal pressure evolution of cells while being cycled at high rates or experiencing damaging events such as over-discharge. While these tests were not able to address all cycling and damage conditions, they have established the bulk internal pressure behavior and the ability to correlate its behavior to aging.

Single Cycle Internal Pressure Evolution

The intent of this study was to examined the micro behavior of the internal pressure evolution inside of a cell during a single 1C cycle and compare that behavior periodically throughout high-rate lifecycle testing. Lifecycle testing was performed on a 2.6 Ah, LiFePO4//Graphite, LFP-26650P LIB at elevated rates (3.5C Charge/11.5C Discharge) until the battery reached approximately 80% of its original capacity resulting in the completion of 500 cycles. Baseline performance tests were conducted post transfer (5 cycles), and at 100 cycle intervals throughout the lifecycle testing in order to measure the battery performance with respect to time. These baseline performance tests included DC ESR, capacity, and EIS measurements. The constant current full discharge tests were conducted at 1 C to measure the amount of accessible capacity within the battery. The discharge tests were also used to evaluate the internal pressure

change within the battery with respect to cycle number. EIS measurements were conducted at 100% SOC to assess the change in internal impedance as the battery was cycled.

Capacity measurements and analysis confirmed the battery's accessible capacity faded as a result of the increase in DC ESR. EIS measurements and modeling analysis also established that the most significant material change within the battery during life cycling resulted from the rise in Ohmic resistance. Analysis of the battery's internal pressure evolution during the 1C baseline discharges yielded information elucidating apparent reversible electrode volume changes during the charge and discharge process. A strong SRCC correlation was established between the fade in 1C pressure delta and the capacity over the lifecycle of the battery. While it is well understood that the electrode volume changes during the intercalation / de-intercalation process, this bulk evaluation technique may be used to assess the performance of commercially packaged batteries and potentially as a predictive measure of battery aging. Differential capacity analysis was used to confirm the correlation of the behavior with the deintercalation process. The pressure data and analysis indicate a reduction in the amount of lithium de-intercalated during discharge as a result of the rise in the internal resistance and thus an apparent shift in the volume change over the lifecycle.

Over-Discharge Behavior of Various Li-Ion Batteries

This study focused on identifying the behavior of pressure evolution during an over discharge event of various li-ion chemistries as a means to identify damage to a cell as a precursor to failure. Four commercial LIBs with different chemistries

($LiCoO_2/C_6$, $LiFePo_4/C_6$, $LiMn_2O_4/C_6$, $LiNiCoMnO_2/C_6$) were selected for use in this study. Each cell was conditioned by cycling five times at a 1C rate using a CC discharge and CC-CV charge procedure. The cell was then charged CC-CV at C/5, allowed to rest for 60 minutes, and then discharged at C/5 to 0.0 V and held for 10 minutes. Baseline characterization tests including capacity, impedance, and resting pressure of the cell were performed after transfer into the test chamber and after the over-discharge procedure was complete. The gases generated in the cell were analyzed at the conclusion of testing by gas chromatography. The surface morphology for the cathode and anode samples was characterized by SEM cold FESEM.

Conventional means of non-destructive diagnostic testing including, capacity, DC ESR, and EIS were used before and after the over discharge event, and these tests did not reveal any significant degradation to the cell that would alert the user that fundamental damage had been done to the cell. Further destructive testing was conducted including SEM imaging of the electrodes, and GC-MS analysis of extracted gas and did indicate that the cell experienced a damaging event. GC-MS confirmed that CO, CO_2, CH_4, C_2H_4, and C_2H_6 gases were produced as a product of electrolyte decomposition. While these tests are useful for post-mortem damage assessment, they are not practical for use as a predicative measure for cell damage during operation. However, measuring the internal pressure of the cells showed a significant pressure change due to the gas production, and clearly indicated that a non-normal event occurred due to the step change in pressure. This change in pressure is indicative of damage to the cell and could be used as a predictive measure in advance of a significant loss in capacity or complete cell failure with further cycles.

Correlation of internal Pressure Rise and Capacity Degradation

The intent of this study was to examine the correlation of internal pressure rise and capacity fade of $LiCoO_2/C_6$ cells cycled at elevated rates over a full lifecycle. Multiple cells were cycled using a CC discharge and CC/CV charge at 1C/2C, 2C/1C, and 2C/2C charge and discharge rates respectively until the capacity had reached 60% of the nameplate value. Baseline characterization tests, including capacity, impedance, and resting pressure of the cell were performed after transfer into the test chamber and at subsequent 25 cycle intervals. Post cycling analysis included GC-MS of the gases produced as well as SEM imaging of the electrodes.

The cells demonstrated poor cycling capability with Cell 01 experiencing 37% capacity fade or 2.53 Ah after 375 cycles, Cell 02 experiencing 43% capacity fade or 2.26 Ah after 100 cycles, and Cell 03 experiencing 39% capacity fade or 2.45 Ah after 250 cycles. Both the internal pressure rise and capacity fade demonstrated a paralinear behavior that is primarily parabolic in the early stage with a dependence on the square root of the cycle number. This was followed by a transition to the final region with a linear dependence on cycle number. A closer examination of the pressure and capacity evolution presented a direct correlation indicating a very strong, statistically significant monotonic relationship.

From the GC-MS analysis, the gases generated during repeated cycling are CO, CO_2, CH_4, C_2H_6, and C_3H_8 with CH_4 being the main gaseous product. The gases are produced at a high rate in the early stage of cycling with a transition to a slow linear production in the later stage. Previous work has indicated that the hydrocarbon gases are a product of the reduction of DEC on the surface of the anode and are the primary components of the SEI film formation. A comparison of the low and high resolution

SEM images for all three cells clearly demonstrates that the decomposition of the electrolyte seen in the GC-MS analysis was dominated by the reduction reaction at the surface of the anode, as well as crack formations inducing continued electrolyte reduction. Images of the cathode demonstrated minimal changes between the pre and post cycled cells indicating minimal contribution to the production of gas. EIS analysis demonstrated the same staged behavior experienced by the pressure and capacity with a small R_{SEI} growth in the early stages, and a transition to a stronger contribution of the charge-transfer kinetics and Li^+ transport through the SEI in the later stages.

The data and analysis presented of pressure evolution, capacity fade, and the correlation of the two for a given system can be a useful diagnostic tool aiding in the prediction of cell life or damage. While the work presented here is representative of $LiCoO_2/C_6$ cells manufactured by the Tenergy Company, systems in which the primary degradation mechanisms feature gas evolution can be analyzed by this method adding an additional in-situ measurement that can be used as a substitute or to supplement other more conventional diagnostic tools. Additionally, this method may be of particular use for systems that are cycled at high rate, high temperatures, or both.

Conclusions

The results shown in this dissertation illustrate the ability to use the bulk internal pressure inside of a li-ion cell as an in-situ metric of cell degradation. This methodology relies on various side reactions within the cell, namely the decomposition of electrolyte, to identify damage to the cell in events such as over-discharge and long term cycling. This is particularly useful for cells cycled at elevated rates and temperatures as these will accelerate the aging of the cell and the decomposition of the electrolyte. While it is

not practical to use the test setup described in this dissertation outside of a laboratory setting, it is envisioned that the outer case of the sealed cell could be used to measure deflection due to internal pressure change with a simple strain gage. While this methodology would need to be verified, its simplicity coupled with the knowledge gained through these studies could enable a powerful low cost diagnostic tool to be added to a battery management system aiding in the prediction of aging or damage to the battery system.

Appendix A

Critical Values for Spearman's Rank Correlation Coefficient

Table A-1 Critical Values for Spearman's Rank Correlation Coefficient

	Probability that the result occurred by chance				
n	**0.1**	**0.05**	**0.025**	**0.01**	**0.005**
4	1.0000	1.0000	1.0000	1.0000	1.0000
5	0.7000	0.9000	0.9000	1.0000	1.0000
6	0.6571	0.7714	0.8286	0.9429	0.9429
7	0.5714	0.6786	0.7857	0.8571	0.8929
8	0.5476	0.6429	0.7381	0.8095	0.8571
9	0.4833	0.6000	0.6833	0.7667	0.8167
10	0.4424	0.5636	0.6485	0.7333	0.7818
11	0.4182	0.5273	0.6091	0.7000	0.7545
12	0.3986	0.5035	0.5874	0.6713	0.7273
13	0.3791	0.4780	0.5604	0.6484	0.6978
14	0.3670	0.4593	0.5385	0.6220	0.6747
15	0.3500	0.4429	0.5179	0.6000	0.6536
16	0.3382	0.4265	0.5029	0.5824	0.6324
17	0.3271	0.4124	0.4821	0.5577	0.6055
18	0.3170	0.4000	0.4683	0.5425	0.5897
19	0.3077	0.3887	0.4555	0.5285	0.5751
20	0.2992	0.3783	0.4438	0.5155	0.5614
21	0.2914	0.3687	0.4329	0.5034	0.5487
22	0.2841	0.3598	0.4227	0.4921	0.5368
23	0.2774	0.3515	0.4132	0.4815	0.5256
24	0.2711	0.3438	0.4044	0.4716	0.5151
25	0.2653	0.3365	0.3961	0.4622	0.5052
26	0.2598	0.3297	0.3882	0.4534	0.4958
27	0.2546	0.3233	0.3809	0.4451	0.4869
28	0.2497	0.3172	0.3739	0.4372	0.4785
29	0.2451	0.3115	0.3673	0.4297	0.4705
30	0.2407	0.3061	0.3610	0.4226	0.4629

Appendix B

Pressure Test Chamber CAD Drawings

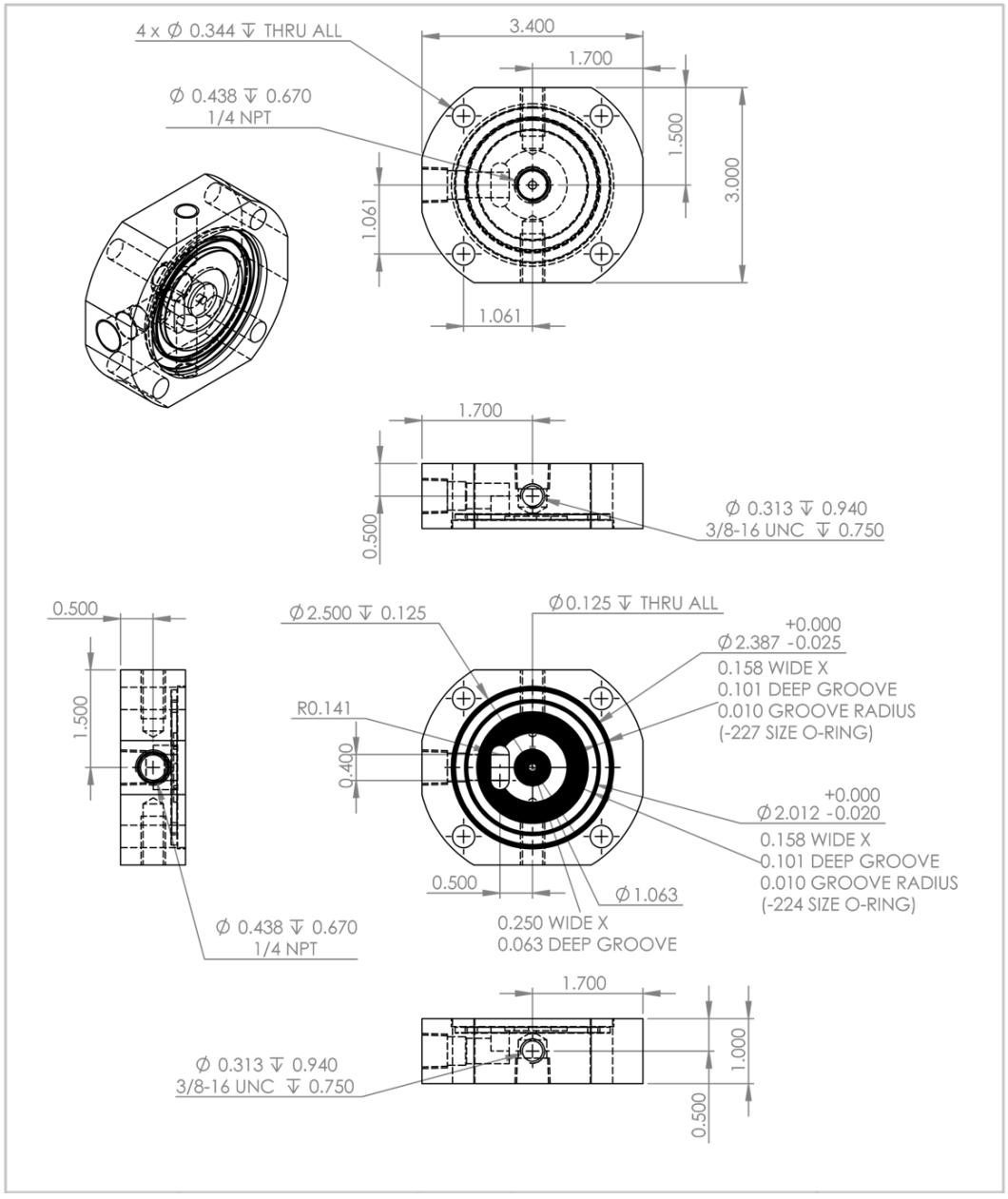

Figure B-1 Pressure test chamber – top disk CAD drawing.

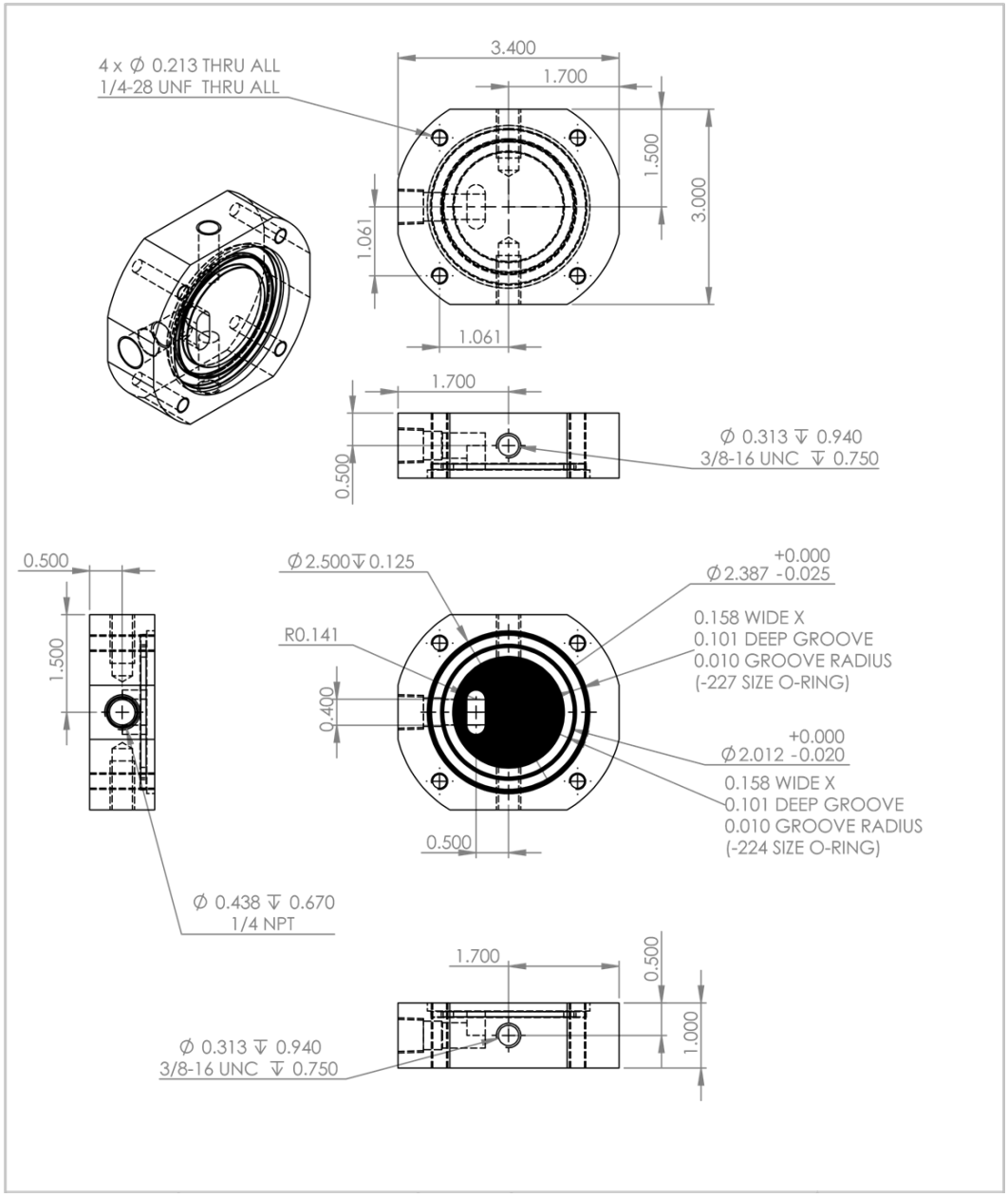

Figure B-2 Pressure test chamber – bottom disk CAD drawing.

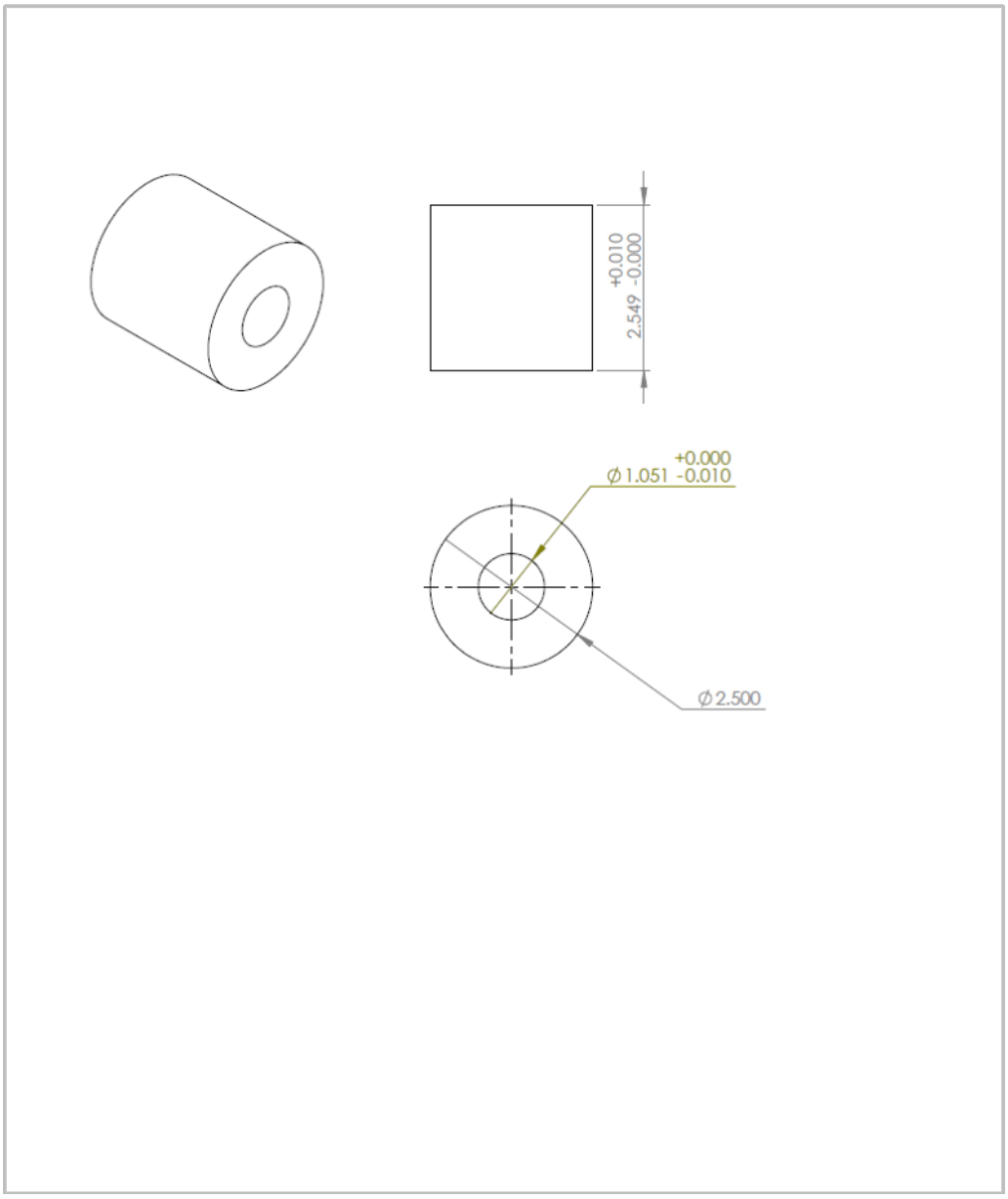

Figure B-3 Pressure test chamber – PTFE CAD drawing.

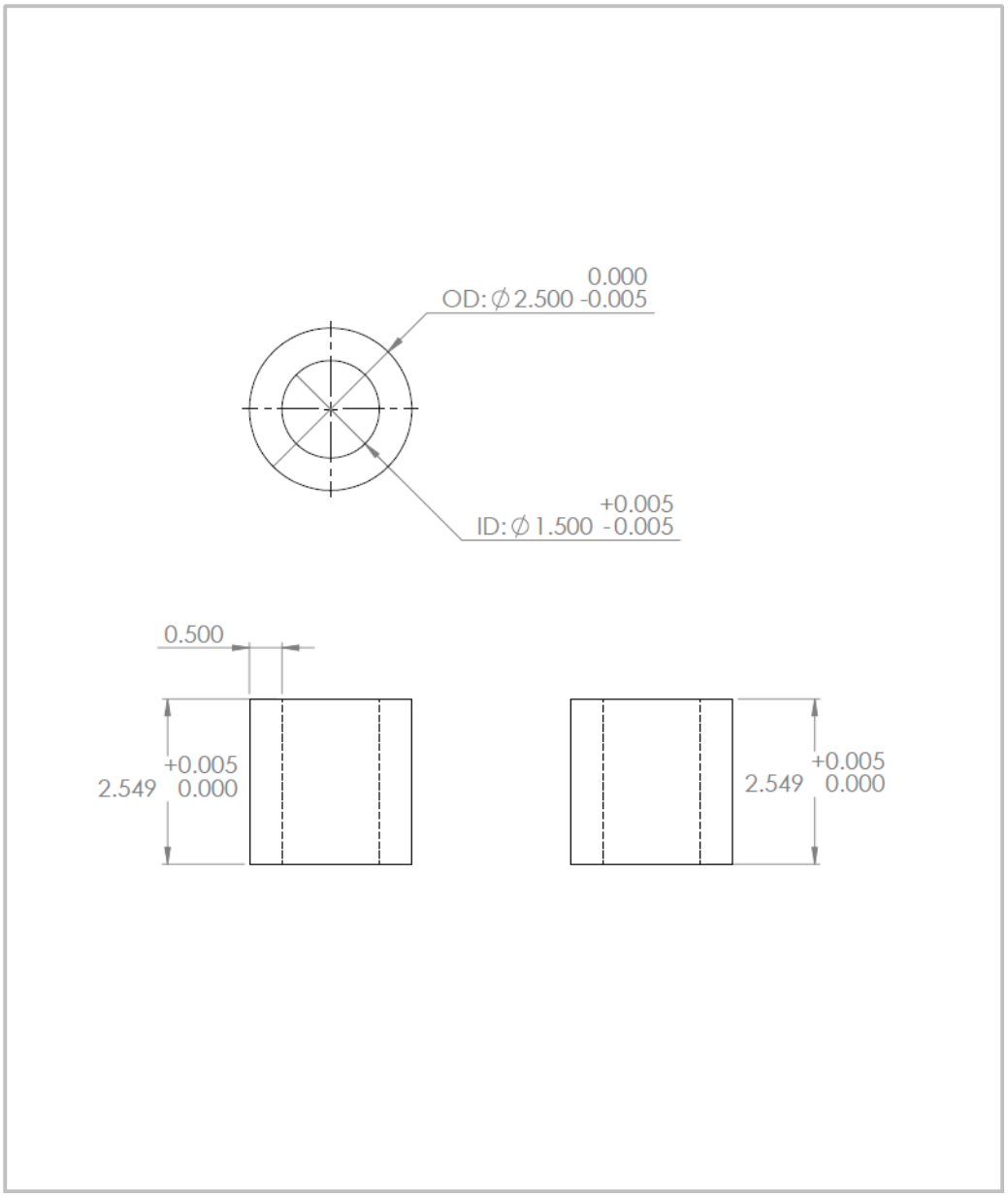

Figure B-4 Pressure test chamber – quartz CAD drawing.

References

[1] J. Vetter, P. Novák, M. R. Wagner, C. Veit, K.-C. Möller, J. O. Besenhard, M. Winter, M. Wohlfahrt-Mehrens, C. Vogler, and A. Hammouche, “Ageing mechanisms in lithium-ion batteries,” *J. Power Sources*, vol. 147, no. 1–2, pp. 269–281, Sep. 2005.

[2] R. Spotnitz, “Simulation of capacity fade in lithium-ion batteries,” *J. Po*, vol. 113, no. August 2002, pp. 72–80, 2003.

[3] V. Agubra and J. Fergus, “Lithium Ion Battery Anode Aging Mechanisms,” *Materials (Basel).*, vol. 6, no. 4, pp. 1310–1325, Mar. 2013.

[4] G. Ning, B. Haran, and B. N. Popov, “Capacity fade study of lithium-ion batteries cycled at high discharge rates,” *J. Power Sources*, vol. 117, no. 1–2, pp. 160–169, May 2003.

[5] K. Kumai, H. Miyashiro, Y. Kobayashi, K. Takei, and R. Ishikawa, “Gas generation mechanism due to electrolyte decomposition in commercial lithium-ion cell,” *J. Power Sources*, vol. 81–82, pp. 715–719, Sep. 1999.

[6] “Voltaic Pile,” *IEEE Global History Network*, 2013. [Online]. Available: http://www.ieeeghn.org/wiki/index.php/Voltaic_Pile.

[7] L. Nazar and O. Crosnier, “Anodes and Composite Anodes: An Overview,” in *Lithium Batteries Science and Technology*, G.-A. Nazri and G. Pistoia, Eds. Springer, 2009, pp. 112–143.

[8] “Ni-Cad Batteries - 26650,” *Radio Shack*, 1990. [Online]. Available: http://support.radioshack.com/support_tutorials/batteries/images/nicad.gif.

[9] D. Kopeliovich, “General information about graphite,” *Substances and Technologies*, 2013. [Online]. Available: http://www.substech.com/dokuwiki/doku.php?id=graphite.

[10] X. Y. Song and K. Kinoshita, “Microstructural Characterization of Lithiated Graphite,” *J. Electrochem. Soc.*, vol. 143, no. 6, pp. L120–L123, 1996.

[11] M. Wohlfahrt-Mehrens, C. Vogler, and J. Garche, “Aging mechanisms of lithium cathode materials,” *J. Power Sources*, vol. 127, no. 1–2, pp. 58–64, Mar. 2004.

[12] M. Pasquali, S. Passerini, and G. Pistoia, “Trends in Cathode Materials for Rechargeable Batteries,” in *Lithium Batteries Science and Technology*, G.-A. Nazri and G. Pistoia, Eds. Springer, 2009, pp. 315–360.

[13] S. Nakhal, M. Lerch, J. Koopman, M. M. Islam, and T. Bredow, “Crystal Structure of 3R-LiTiS 2 and its Stability Compared to Other Polymorphs,” *Zeitschrift für Anorg. und Allg. Chemie*, vol. 639, no. 15, pp. 2822–2825, Dec. 2013.

[14] N. Yabuuchi, Y. Kawamoto, R. Hara, T. Ishigaki, A. Hoshikawa, M. Yonemura, T. Kamiyama, and S. Komaba, “A comparative study of LiCoO2 polymorphs: structural and electrochemical characterization of O2-, O3-, and O4-type phases.,” *Inorg. Chem.*, vol. 52, no. 15, pp. 9131–42, Aug. 2013.

[15] E. Meza, J. Ortiz, D. Ruíz-León, J. F. Marco, and J. L. Gautier, “Lithium-nickel cobalt oxides with spinel structure prepared at low temperature. XRD, XPS, and EIS measurements,” *Mater. Lett.*, vol. 70, pp. 189–192, Mar. 2012.

[16] M. Lengyel, X. Zhang, G. Atlas, H. L. Bretscher, I. Belharouak, and R. L. Axelbaum, “Composition Optimization of Layered Lithium Nickel Manganese Cobalt Oxide Materials Synthesized via Ultrasonic Spray Pyrolysis,” *J. Electrochem. Soc.*, vol. 161, no. 9, pp. A1338–A1349, Jun. 2014.

[17] M. S. Islam and C. a J. Fisher, “Lithium and sodium battery cathode materials: computational insights into voltage, diffusion and nanostructural properties.,” *Chem. Soc. Rev.*, vol. 43, no. 1, pp. 185–204, Jan. 2014.

[18] M. S. Whittingham, Y. Song, S. Lutta, P. Y. Zavalij, and N. a. Chernova, “Some transition metal (oxy)phosphates and vanadium oxides for lithium batteries,” *J. Mater. Chem.*, vol. 15, no. 33, p. 3362, 2005.

[19] H. Huang, S. Yin, and L. Nazar, “Approaching Theoretical Capacity of LiFePO4 at Room Temperature at High Rates,” *Electrochem. Solid-State Lett.*, vol. 4, no. 10, pp. A170–A172, 2001.

[20] M. Nazari, “Liquid Electrolytes: Some Theoretical and Practical Aspects,” in *Lithium Batteries Science and Technology*, G.-A. Nazri and G. Pistoia, Eds. Springer, 2009, pp. 509–529.

[21] D. Aurbach, Y. Talyosef, B. Markovsky, E. Markevich, E. Zinigrad, L. Asraf, J. S. Gnanaraj, and H.-J. Kim, “Design of electrolyte solutions for Li

and Li-ion batteries: a review," *Electrochim. Acta*, vol. 50, no. 2–3, pp. 247–254, Nov. 2004.

[22] D. Aurbach, E. Zinigrad, Y. Cohen, and H. Teller, "A short review of failure mechanisms of lithium metal and lithiated graphite anodes in liquid electrolyte solutions," *Solid State Ionics*, vol. 148, pp. 405–416, 2002.

[23] A. Wuersig, W. Scheifele, and P. Novák, "CO[sub 2] Gas Evolution on Cathode Materials for Lithium-Ion Batteries," *J. Electrochem. Soc.*, vol. 154, no. 5, p. A449, 2007.

[24] J. Vetter, M. Holzapfel, A. Wuersig, W. Scheifele, J. Ufheil, and P. Novák, "In situ study on CO2 evolution at lithium-ion battery cathodes," *J. Power Sources*, vol. 159, no. 1, pp. 277–281, Sep. 2006.

[25] F. La Mantia, F. Rosciano, N. Tran, and P. Novák, "Direct evidence of oxygen evolution from Li1+x (Ni1/3Mn1/3Co1/3)1−x O2 at high potentials," *J. Appl. Electrochem.*, vol. 38, no. 7, pp. 893–896, Feb. 2008.

[26] J. H. Seo, J. Park, G. Plett, and A. M. Sastry, "Gas-Evolution Induced Volume Fraction Changes and Their Effect on the Performance Degradation of Li-Ion Batteries," *Electrochem. Solid-State Lett.*, vol. 13, no. 9, p. A135A137, 2010.

[27] M. Winter and G. Wrodnigg, "Dilatometric investigations of graphite electrodes in nonaqueous lithium battery electrolytes," *J. Electrochem. Soc.*, vol. 147, no. 7, pp. 2427–2431, 2000.

[28] H. Yoshida, T. Fukunaga, T. Hazama, M. Terasaki, M. Mizutani, and M. Yamachi, "Degradation mechanism of alkyl carbonate solvents used in lithium-ion cells during initial charging," *J. Power Sources*, vol. 68, no. 2, pp. 311–315, Oct. 1997.

[29] H. Maleki and J. N. Howard, "Effects of overdischarge on performance and thermal stability of a Li-ion cell," *J. Power Sources*, vol. 160, no. 2, pp. 1395–1402, Oct. 2006.

[30] H.-F. Li, J.-K. Gao, and S.-L. Zhang, "Effect of Overdischarge on Swelling and Recharge Performance of Lithium Ion Cells," *Chinese J. Chem.*, vol. 26, pp. 1585–1588, 2008.

[31] J. Shu, M. Shui, D. Xu, D. Wang, Y. Ren, and S. Gao, "A comparative study of overdischarge behaviors of cathode materials for lithium-ion batteries," *J. Solid State Electrochem.*, vol. 16, pp. 819–824, 2011.

[32] D. Belov and M.-H. Yang, “Failure mechanism of Li-ion battery at overcharge conditions,” *J. Solid State Electrochem.*, vol. 12, no. 7–8, pp. 885–894, Nov. 2007.

[33] F. Xu, H. He, Y. Liu, C. Dun, Y. Ren, Q. Liu, M. Wang, and J. Xie, “Failure Investigation of LiFePO4 Cells under Overcharge Conditions,” *J. Electrochem. Soc.*, vol. 159, no. 5, pp. A678–A687, 2012.

[34] T. Ohsaki, T. Kishi, T. Kuboki, N. Takami, N. Shimura, Y. Sato, M. Sekino, and A. Satoh, “Overcharge reaction of lithium-ion batteries,” *J. Power Sources*, vol. 146, no. 1–2, pp. 97–100, Aug. 2005.

[35] A. Hammami, N. Raymond, and M. Armand, “Runaway risk of forming toxic compounds,” *Science*, vol. 424, pp. 635–636, Aug. 2003.

[36] D. P. Abraham, E. P. Roth, R. Kostecki, K. McCarthy, S. MacLaren, and D. H. Doughty, “Diagnostic examination of thermally abused high-power lithium-ion cells,” *J. Power Sources*, vol. 161, no. 1, pp. 648–657, Oct. 2006.

[37] I. Belharouak, G. M. Koenig, and K. Amine, “Electrochemistry and safety of Li4Ti5O12 and graphite anodes paired with LiMn2O4 for hybrid electric vehicle Li-ion battery applications,” *J. Power Sources*, vol. 196, no. 23, pp. 10344–10350, Dec. 2011.

[38] J. Wen, Y. Yu, and C. Chen, “A Review on Lithium-Ion Batteries Safety Issues: Existing Problems and Possible Solutions,” *Mater. Express*, vol. 2, no. 3, pp. 197–212, Sep. 2012.

[39] W. Kong, H. Li, X. Huang, and L. Chen, “Gas evolution behaviors for several cathode materials in lithium-ion batteries,” *J. Power Sources*, vol. 142, no. 1–2, pp. 285–291, Mar. 2005.

[40] K. Tagawa and R. Brodd, “Cylindrical-Cell Fabrication,” in *Lithium-Ion Batteries: Science and Technologies*, M. Yoshio, R. Brood, and A. Kozawa, Eds. Springer Science & Business Media, 2010, pp. 181–194.

[41] J. Kim, “Cylindrical rechargeable battery with improved stability,” WO2011019237 A2, 2009.

[42] J. Li, E. Murphy, J. Winnick, and P. . Kohl, “Studies on the cycle life of commercial lithium ion batteries during rapid charge–discharge cycling,” *J. Power Sources*, vol. 102, no. 1–2, pp. 294–301, Dec. 2001.

[43] J. R. Macdonald, “Impedance spectroscopy: Old Problems and New Developments,” *Electrochim. Acta*, vol. 35, no. 10, pp. 1483–1492, Oct. 1990.

[44] H. Shih and T. Lo, “Electrochemical Impedance Spectroscopy for Battery Research and Development,” *Cortech Corp. CA, Tech. Rep*, 1996.

[45] J. Macdonald, “Impedance spectroscopy: Models, data fitting, and analysis,” *Solid State Ionics*, vol. 176, no. 25–28, pp. 1961–1969, Aug. 2005.

[46] J. Zhao, L. Wang, and X. He, “Kinetic investigation of LiCOO2 by electrochemical impedance spectroscopy (EIS),” *Int. J. Electrochem. Sci.*, vol. 5, pp. 478–488, 2010.

[47] E. Barsoukov, J. H. Kim, D. H. Kim, K. S. Hwang, C. O. Yoon, and H. Lee, “Parametric analysis using impedance spectroscopy : relationship between material properties and battery performance,” *J. New Mater. Electrochem. Syst.*, vol. 310, pp. 303–310, 2000.

[48] E. Barsoukov and J. R. Macdonald, Eds., *Impedance Spectroscopy Theory, Experiment, and Applications*, 3rd ed. John Wiley & Sons, 2005.

[49] Y. Zhang and C.-Y. Wang, “Cycle-Life Characterization of Automotive Lithium-Ion Batteries with LiNiO[sub 2] Cathode,” *J. Electrochem. Soc.*, vol. 156, no. 7, p. A527, 2009.

[50] M. Thomas, P. Bruce, and J. Goodenough, “AC Impedance Analysis of Polycrystalline Insertion Electrodes: Application to Li1− x CoO2,” *J. …*, p. 1521, 1985.

[51] J. Goodenough, “Design Considerations,” *Solid State Ionics*, vol. 69, pp. 184–198, 1994.

[52] H.-G. Schweiger, O. Obeidi, O. Komesker, A. Raschke, M. Schiemann, C. Zehner, M. Gehnen, M. Keller, and P. Birke, “Comparison of several methods for determining the internal resistance of lithium ion cells.,” *Sensors (Basel).*, vol. 10, no. 6, pp. 5604–25, Jan. 2010.

[53] C. Hoch, H. Schier, C. Kallfaß, C. Tötzke, A. Hilger, and I. Manke, “Electrode deterioration processes in lithium ion capacitors monitored by in situ X-ray radiography on micrometre scale,” *Micro Nano Lett.*, vol. 7, no. 3, pp. 262–264, 2012.

[54] B. Markovsky, a Rodkin, Y. . Cohen, O. Palchik, E. Levi, D. Aurbach, H.-J. Kim, and M. Schmidt, “The study of capacity fading processes of Li-ion batteries: major factors that play a role,” *J. Power Sources*, vol. 119–121, pp. 504–510, Jun. 2003.

[55] A. Padhi and K. Nanjundaswamy, “Effect of structure on the Fe3+/Fe2+ redox couple in iron phosphates,” *J. Electrochem. Soc.*, vol. 144, no. 5, pp. 1609–1613, 1997.

[56] H. Lin, Y. Wen, C. Zhang, L. Zhang, Y. Huang, B. Shan, and R. Chen, “A GGA+U study of lithium diffusion in vanadium doped LiFePO4,” *Solid State Commun.*, vol. 152, no. 12, pp. 999–1003, Jun. 2012.

[57] J. Christensen and J. Newman, “Stress generation and fracture in lithium insertion materials,” *J. Solid State Electrochem.*, vol. 10, no. 5, pp. 293–319, Mar. 2006.

[58] J. Barker, “In-situ measurement of the thickness changes associated with cycling of prismatic lithium ion batteries based on LiMn2O4 and LiCoO2,” *Electrochim. Acta*, vol. 45, no. 1–2, pp. 235–242, Sep. 1999.

[59] C. KOWALSKI, “on the of Non-normality On the Effects of the Sample Product-moment Distribution Coefficient Correlation,” *R. Stat. Soc.*, vol. 21, no. 1, pp. 1–12, 1972.

[60] E. Hatzikraniotis, D. Terzidis, C. L. Mitsas, D. I. Siapkas, S. State, and P. Section, “Graphites for Li-Ion Cells: Study of the Irreversible Capacity Using Differential Capacity Analysis,” *Ionics (Kiel).*, vol. 5, pp. 399–404, 1999.

[61] I. Bloom, J. Christophersen, and K. Gering, “Differential voltage analyses of high-power lithium-ion cells,” *J. Power Sources*, vol. 139, no. 1–2, pp. 304–313, Jan. 2005.

[62] K. Xu, “Nonaqueous Liquid Electrolytes for Lithium-Based Rechargeable Batteries,” *Chem. Rev.*, vol. 104, no. 10, pp. 4303–4418, Oct. 2004.

[63] S.-T. Myung, Y. Hitoshi, and Y.-K. Sun, “Electrochemical behavior and passivation of current collectors in lithium-ion batteries,” *J. Mater. Chem.*, vol. 21, no. 27, p. 9891, 2011.

[64] M. Lu, H. Cheng, and Y. Yang, “A comparison of solid electrolyte interphase (SEI) on the artificial graphite anode of the aged and cycled

commercial lithium ion cells," *Electrochim. Acta*, vol. 53, no. 9, pp. 3539–3546, Mar. 2008.

[65] I. Bloom, B. . Cole, J. . Sohn, S. . Jones, E. . Polzin, V. . Battaglia, G. . Henriksen, C. Motloch, R. Richardson, T. Unkelhaeuser, D. Ingersoll, and H. . Case, "An accelerated calendar and cycle life study of Li-ion cells," *J. Power Sources*, vol. 101, no. 2, pp. 238–247, Oct. 2001.

[66] J. Shin, C. Han, U. Jung, and S. Lee, "Effect of Li 2 CO 3 additive on gas generation in lithium-ion batteries," *J. Power Sources*, vol. 109, pp. 47–52, 2002.

[67] K. Zhao, M. Pharr, J. J. Vlassak, and Z. Suo, "Fracture of electrodes in lithium-ion batteries caused by fast charging," *J. Appl. Phys.*, vol. 108, no. 7, p. 073517, 2010.

[68] J. Yan, B.-J. Xia, Y.-C. Su, X.-Z. Zhou, J. Zhang, and X.-G. Zhang, "Phenomenologically modeling the formation and evolution of the solid electrolyte interface on the graphite electrode for lithium-ion batteries," *Electrochim. Acta*, vol. 53, no. 24, pp. 7069–7078, Oct. 2008.

[69] F. Huet, "A review of impedance measurements for determination of the state-of-charge or state-of-health of secondary batteries," *J. Power Sources*, vol. 70, no. 1, pp. 59–69, Jan. 1998.

[70] S. Rodrigues, N. Munichandraiah, and A. K. Shukla, "A review of state-of-charge indication of batteries by means of a.c. impedance measurements," *J. Power Sources*, vol. 87, pp. 12–20, 2000.

Biographical Information

Anthony Matasso holds a Bachelor's degree in Electrical Engineering from the University of Texas at Arlington and a Master's degree in Systems Engineering from Southern Methodist University. After receiving his Bachelor's degree, Anthony went to work as an Engineer for Foresight Automation in Fort Worth, TX. He transitioned to Lockheed Martin where he worked as an engineer on the F-16 program and later within the Skunk Works organization. His research interests include aircraft electrical power systems, vehicle systems modeling and simulation, and technology product development.